Chapter 4
Nanocrystals - Nanowires - Nanolayers

The dimensionality of nanosystems plays an important role in nanoscicnce and nanotechnology. In nanostructures with OD macroscopic extension (OD - nanocrystals), 1D macroscopic extension (I D - nanowires), or 2D macroscopic extensions (2D - nanolayers), novel properties emerge compared to macroscopic bulk systems due to quantum conlincment, charge quantization, magnetic exchange length, etc. In the case of semiconductor systems, the nanostructures of different dimensionality are often called quantum dots, quantum wires, and quantum wells.

Dimensionality effects of nanostructures have been introduced with some exemplary features in Chap. 1 and have been shown to be of relevance in synthesis (Chap. 3). In the present section some generic characteristics of nanocrystals, nanowires, and nanolayers will be discussed. Dimensionality effects will be resumed later in nanoscale carbon systems (Chap. 5) and in the discussion of nanomagnetism (Chap. 8).

4.1 Nanocrystals

Nanodots exhibit in all three spatial directions and dimensions smaller than the dc Broglic wave length of the charge carriers. Semiconductor nanodots are often embedded in another dielectric semiconductor matrix [4.1, 4.2). Single quantum dots may provide innovative components for quantum information processing, quantum cryptography, or hybrid DRAM/Flash data storage. In large numbers (billions) they may form optoelectronic components, lasers or amplifiers, and new systems for communication technology, consumer electronics, or high-precision metrology.

4.1.1 Synthesis of Nanocrystals

Some more specific features of the synthesis of nanocrystals will be discussed in the following in addition to the more general discussion in Chap. 3.

Metal seeds have been used as catalysts for growing semiconductor or oxide nanowires cither in the gas phase, using the vapor-liquid-solid mechanism, or

H.-E. Schacfcr. *Nanoscicnce.* DOI 10.1007/978-3-642-10559-3_4.

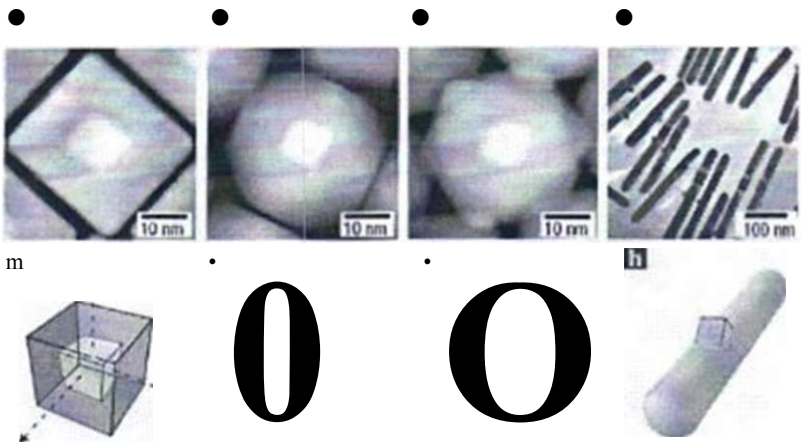

V [1]

r^ **Fig. 4.1** Shapc'controllcd bimctallic Pt-Pd core-shell nanoparticlcs grown by the seeded-growth approach 14.4) using Pi cubes as seeds: high-angle annular dark-field scanning transmission electron micrographs (HAADF-STKM), and models of the core shell nanopaiticles. (a, b) Cubic Pt seed within the Pd shell, (c-**f)** Control over the directed growth of Pd on Pt nanocubcs is achieved by the addition of increasing amounts of NO>. which alters the growth rates along the <100> and **<111>** directions to give Pi/Pd core-shell cuboctahedra (c. **d)** oroctahcdra **(e.** *f).* **(g, h)** For Pt/Au. where the lattice mismatch is large, anisotropic growth of Au rods is observed, with the I*t seed on the perimeter [4.3.4.4). (Reprinted with permission from [4.3]. © 2007 Nature Publishing Group)

in solution via the solution—liquid-solid mechanism (see [4.3]). When using Pi nanocubcs as seeds for growing Pt-Pd bimetallic core-shell nanocubes (see Fig. 4.1a, b), it could be demonstrated that the growth rates along specilic crystal directions can be varied by controlling the concentration of the NO2 atmosphere [4.4]. With increasing concentrations of NO_2. cuboctahcdra or octahedra (Fig. 4.1c-f) can be grown. In addition, lattice mismatch is critically important in this type of epitaxial growth. When Au was rcactcd with the cubic Pt seeds, where the lattice mismatch is *4%* compared with less than \% for Pt-Pd, anisotropic growth of rods was obtained, with a Pt seed partially embedded on the perimeter (Fig. 4.1g, h). The ability to tune the faceting of the Pd shell is of relevance for the application of bimetallic particles in catalysis. Varying the preparation conditions, various facet orientations between all Pd {100} facets (nanocubes) to all Pd {111} facets (octahedra) can be obtained, exhibiting different catalytic properties (see 14.4)).

Infrared quantum dots promise application in fiberoptic and free-space communication photonic components; in in vivo biological tagging in infrared spectral bands in which living tissue is optically penetrable to a depth of 5-10 cm; in solar photovoltaics for energy conversion; and in infrared sensing and imaging based on non-visible signatures (sec [4.5J). The size-dependent properties of quantum-confined states of PbS nanodots (Fig. 4.2a, b) can be tuned for exciton absorption peaks between 800 and 1,800 nm (Fig. 4.2c, d). Room-temperature amplified spontaneous emission has been reported at infrared wavelengths for PbSe and PbS

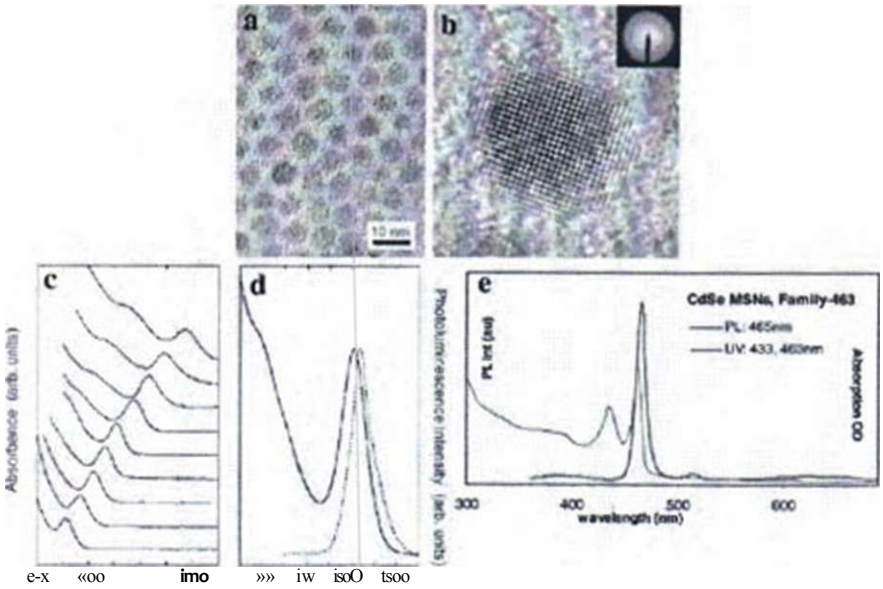

Fig. 4.2 Properties of I*bS quantum dots synthesized by an organometallic route (4.6J. **(a), (b)** High-resolution transmission electron micrographs (HRTKM) of quantum dots with peak luminescence at 1440 nm. (c) Absorption spectra of PbS dots with cxciton peaks size effect tuned from 800-1800 nm. **(d)** Absorption and photoluminccscencc features of 6.5 nm diameter dots (4.6). (c) Single-sized CdSe quantum dot ensembles dispersed in toluene demonstrate a narrow absorption line *(blue line, right* v-axis) and emission line [4.7]. (Reprinted with permission from 14.6] **(a**-d) and [4.7] (c). © 2003 Wiley-VCH **(a-d)** and © 2008 American Chemical Society (e))

nanocrystals (sec [4.5]). Very sharp light absorption near the absorption band edge and very narrow (pure color) photoluminccscencc in the visible range with bandwidths as narrow as 10 nm have been observed for single-sized ensembles of CdSe quantum dots (see Fig. 4.2e).

Dimer clusters of Au nanocrystals and clusters of differently sized Au nanocrystals (Fig. 4.3) can be prepared with high definition and high yield by assembling DNA-cncoded nanoparticlcs [4.8].

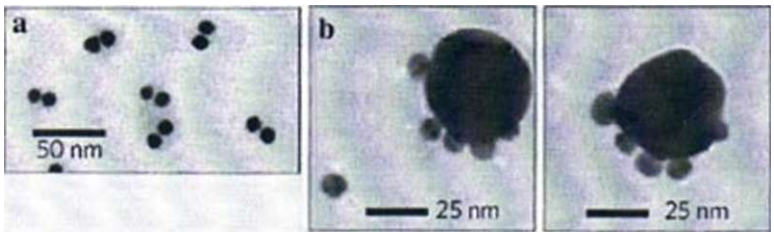

Fig. 4.3 Au dimcrs **(a)** and Au clusters composed of Au particles of different sizes **(b)** assembled by DNA linkers. (Reprinted with permission from [4.8]. © 2009 Nature Publishing Group)

4.1.2 Metal Nanocrystallites - Structure and Properties

The ground-state crystallographic structure of nanocrystals in dependence of size [4.9], the surface atomic structure (4.101, the crystallinity of nanocrystals [4.1 l],and the structural changes of nanocrystals on substrates [4.12] play an important role for the modification of properties and for application. Therefore, structural control of nanocrystals during synthesis [4.131 is of interest.

The ground-stale structures of Fe nanocrystals are icosahedral isomers for a few dozens of atoms (see [4.9]) and for Fe-55 a shell-wise transformed morphology where the innermost shell turns into an almost perfect cuboctahedron, while the outermost shell largely retains its icosahedral shape [4.9]. According to density functional theory [4.9], isomers with the body-centered cubic (bcc) structure of bulk a-Fe are found to be the lowest in energy when the clusters contain more than 100 atoms.

Surface atomic structures of 3-5 nm Au nanocrystals have been probed by electron diffraction [4.10] making use of a 40-nm-diameter electron beam (see Fig. 4.4). Surface reconstruction and bond length contraction are expected to be very important in nanocrystals, where it will affect many phenomena such as interfacial stability and heterogeneous catalysis. The diffraction data of Au nanocrystals together with molecular dynamics studies suggest that the surface atoms do contract, but the amount of contraction depends on the crystallographic orientations of the crystal facet: large out-of-plane bond length contractions for the edge atoms (~ 20 pm); a significant contraction (~ 13 pm) for {100} surface atoms; and a much smaller contraction (~ 5 pm) for atoms in the middle of the densely packed {111}

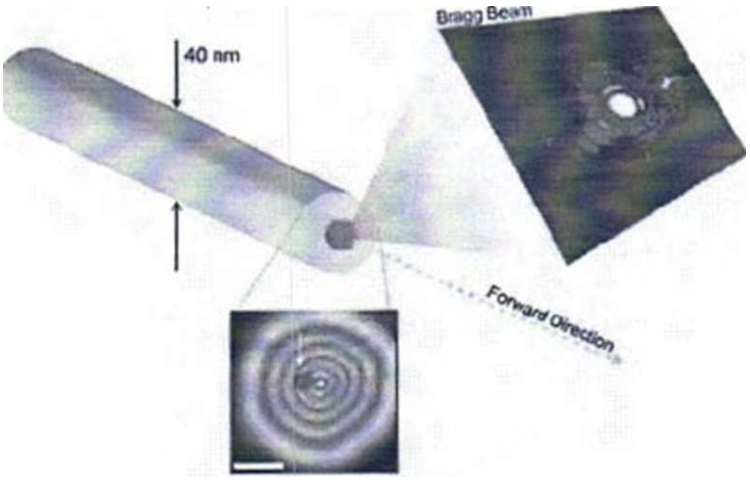

Fig. 4.4 Tlie atomic structure of nanocrystal surfaces can be extracted from diffraction patterns obtained using a coherent electron beam focused to 40 nm. The Au nanocrystal (4 nm) is visible in the *inset (whiteanvw).* The scale bar in the *inset* is 10 nm [4.10.4.14J. (Reprinted with permission from |4.14]. <0 2008 Elsevier)

facets. This indicates a coordination/facct dependence that markedly differentiates the structural dynamics of nanocrystals from bulk crystalline surfaces [4.10].

Raman scattering has been introduced as a new way to measure crystallinity by monitoring changes in the way the crystal vibrates [4.11J. In single-crystalline Au nanocrystals, two separate Raman modes arc found [4.11 j which can be ascribed to two characteristic quadrupolar Raman modes of the elastically anisotropic spherical Au nanocrystals. Polycrystalline nanocrystals produce only one broad Raman peak because they are a blend of different structures. Thus, Raman scattering can offer a simple alternative to, e.g., electron microscopy for characterizing crystallinity [4.111.

Interface structures of Au nanoparticlcs on metal oxide supports may substantially determine the catalytic activity (see Sect. 10.4). By high-angle annular dark-field scanning transmission electron microscopy (HAADF-STEM) with aberration correction (see Sect. 2.6) it was found (Fig. 4.5) that when the gold

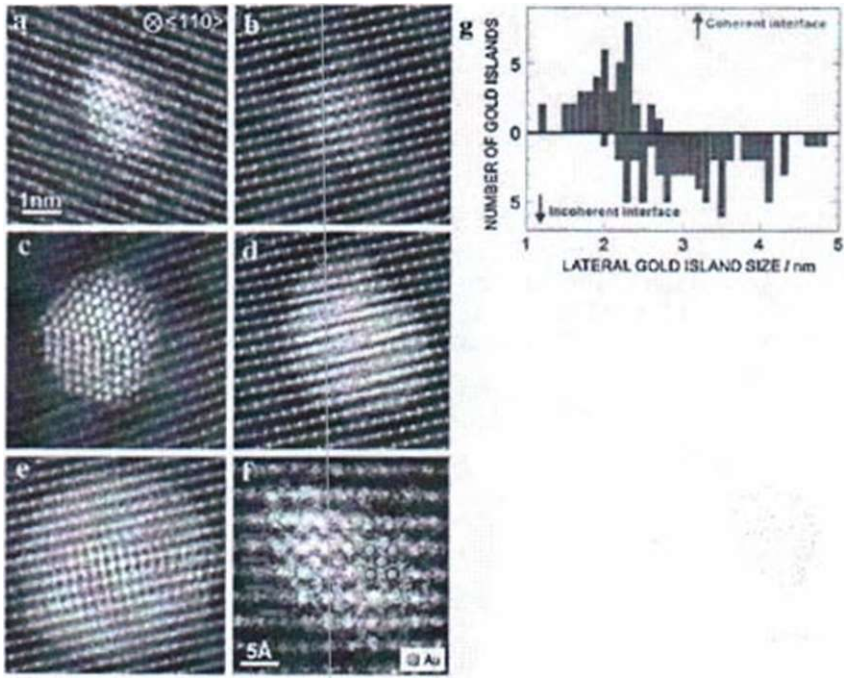

Fly. 4.5 (a-c) High-angle annular dark-lield scanning transmission clcctron micrographs (HAADF-STEMs) of Au nanoparticlcs arranged in the order of the size of the projected particles. The lattice coherency between the Au nanoparticlcs and the TiOj substrate clearly changes according to the Au particle size: **(a)** and (b) are coherent but (c-c) arc incoherent. (0 Magnified image of the epitaxial Au structure shown in **(a).** Not only Au sites on top of the TiO substrate columns but also Au sites on top of the O columns in the troughs of Ti-containing columns (along the arrows) are resolved. (j{) Histogram of the formation of coherent or incoherent interfaces as a function of Au nanoparticlc lateral size estimated from the HAADF-STEM images. (Reprinted with permission from **[4.12). © 2009** American Physical Society)

nanoparticlc size on a Ti20 (110) substrate is smaller than a few nanometers, gold atoms preferentially form an epitaxial and coherent interface. When the Au nanocrystal lite is larger, the gold-Ti20 interface loses lattice coherency in order to accommodate the large lattice mismatch between the dissimilar crystals (4.12).

Crystallinity engineering of Ag nanocrystallites, i.e., selective synthesis of single-crystalline (SC) nanocrystallites or multiply twinned (MT) nanocrystallites, has been achieved [4.13] by chemically modifying the silver phosphine precursor complexes (see Fig. 4.6a). By using NC^-functionalized precursors (1), MT silver nanocrystallites are fabricated (Fig. 4.6d), whereas CI functionalizing (2) results in SC Ag nanocrystallites (Fig. 4.6b). This is ascribed to the preferential etching of the initial metal twinning nuclei by the chloride ions in an oxidative environment, which inhibits the growth of MT clusters [4.13]. The SC and MT nanocrystals exhibit drastically different properties. Upon a chemical reaction with Se, a hollow structure (Fig. 4.6c) is found in the SC nanoparticlc (SC-NP) by a mechanism analogous to the excess-vacancy based Kirkendall effect. In contrast, the MT nanoparticlc (MT-NP) is transformed into a Ag2Se single crystal without hole (Fig. 4.6e), owing to the modification of the atomic diffusion processes by the twin boundaries. For the electron-phonon (e-ph) interaction coupling constants G, values of 15 x 10^{15} JK~'m~^{3}s and 3.7 x lO^JK^m^s are determined for MT- and SC-NPs, respectively [4.13]. This suggests that e-ph scattering is significantly enhanced due to the existence of twinning defects which eventually could lead to sizeable modulation of electronic and heat conductivity and/or superconductivity of metals at the nanoscal^^lastic moduli are derived to be higher in SC-NPs (111 GPa) than in MT-NPs (81 GPa) [4.131 and, from x-ray diffraction studies [4.15], higher in Ag-NPs and Au-NPs than in the bulk materials. The sensitivity of surface plasmons (see Sect. 7.6) in Ag NPs for the refractive index of a solvent or the chain lengths of alkancthiols [4.13] is higher for SC-NPs than for MT-NPs. This is of importance for the optimization of plasmonic mctal-NP-based sensing devices [4.13].

4.1.3 Semiconductor Quantum Dots

In semiconductors excitons, i.e., bound electron-hole pairs can be formed by the association of electron and hole charge carriers or directly by photocxcitation creating an electron in the conduction band and leaving a hole in the valence band. The luminescence resulting from exciton recombination is the basic process of light-emitting diode technology. Conversely, excitons that are formed by photo-excitation can dissociate into free unbound carriers and thus play a central role in detectors or photovoltaic and solar cell devices. Therefore, the properties ofjffcxcitons conlined in quantum dots can change the way that diodes, lasers, or solar cells operate (see (4.2]).

Semiconductor quantum dots are characterized by discrete energy levels where calculations show (see Fig. 4.7) that the centers of gravity of the clectroqh^harge and the hole charge are not directly located on top of each other.

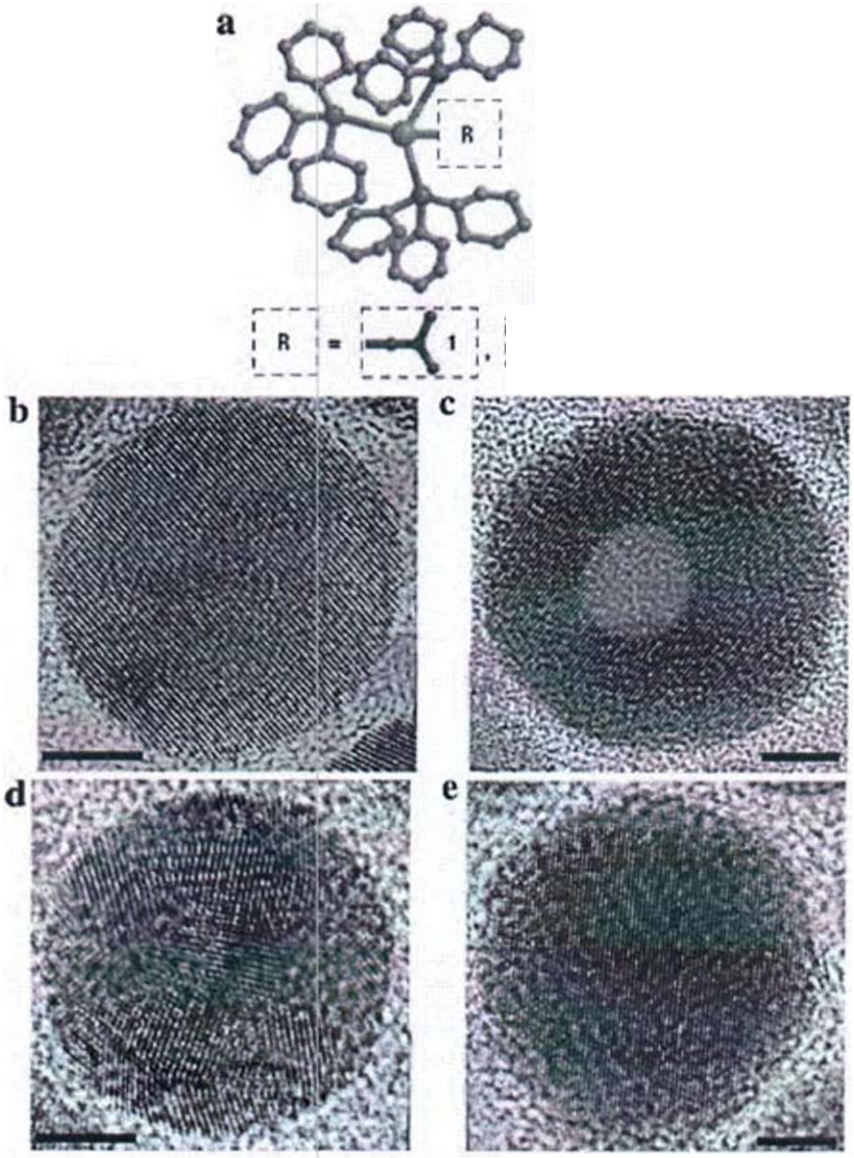

Fig. 4.6 Controlled synthesis of silver nanoparticles (NPs) with selective crystal!inity and chemical transformation to Ag>Se. **(a)** Molecular structure of the phosphine complex precursor (PPh_3)jAg-R with functional groups R = $-NO_3$ (/) or R = -CI(2). **(b)** High-resolution transmission electron micrograph (IIRTI-M) of a single-crystalline (SC) nanoparticle (NP) of silver, (c) HRTEM of SC-Ag'Se NP with a hollow core, **(d)** HRTEM of a multiply twinned nanoparticle (MT-NP) of silver and (c) after reaction with Sc to a SC-AgjSc NP. Scale bars of the HRTEMs: 5 nm. (Reprinted with permission from |4.13|. © 2007 Nature Publishing Group)

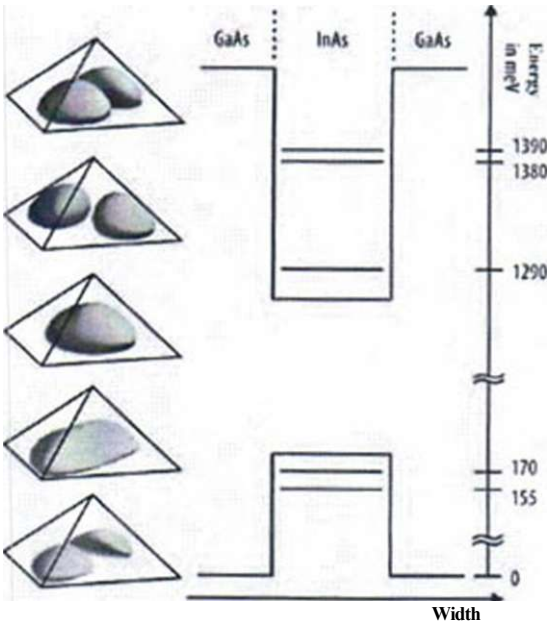

Fig. 4.7 Wave functions and energy levels calculated for the three lowest electron states and the two lowest hole states in a pyramidal InAs quantum dot (baseline 13.3 nm) in a GaAs matrix [4.16], (Reprinted with permission from [4.1]. © 2006 Wiley-VCH)

Due to the discrete energy levels, the luminescence spectra of semiconductor quantum dots are composed of only a few, extremely narrow lines (see Fig. 4.8) originating from different types of exciton complexes. By modifying size, shape, and composition of the quantum dots, the emission wavelength can be tuned over a wide range (Fig. 4.9).

The size tuning of the quantum dot properties is attributed to the confinement of X the exciton in a nanocrystal substantially smaller than the bulk exciton. For example, the exciton Bohr radius of PbS is ~20 nm and its bulk band gap is 0.41 eV. Absorption spectra for PbS quantum dots of radii ranging from 1.3 to 3.5 nm, however, reveal quantum dot exciton energies from 1.5 to 0.7 eV (Fig. 4.10a).

The size-tunable optical excitation energies derive from the semiconductor band gap as well as the exciton binding energy and the quantum mechanical exchange interaction, which are both intimately lied to the size of the exciton [4.21. The exciton binding energy which is about 10 meV in bulk semiconductors increases to 200-50 meV in quantum dots of radii R= 1-2 nm and scales approximately as MR, according to the size dependence of the electron-hole Coulomb interaction. The clectron-holc exchange interaction mixes the single-exciton configurations in a quantum dot, experimentally evident as a splitting between the bright and dark exciton states at the band edge (Fig. 4.10b). This exchange interaction is of the order of milli-elcctron volts in bulk semiconductors but increases 1,000 fold in quantum dots (see [4.2]) and is predicted to scale as $R^{\sim 3}$ as partially confirmed experimentally by the bright-dark splitting of CdSe, CdTe, and GaAs quantum dots (Fig. 4.10b).

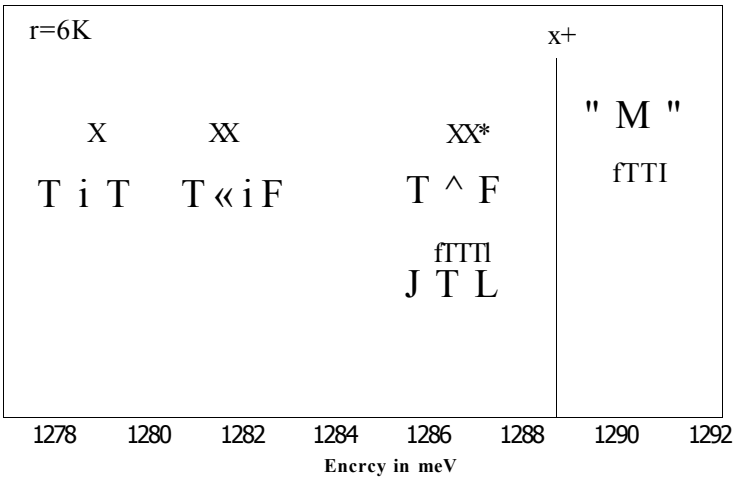

Fig. 4.8 Lumincscencc spectrum of a single InAs quantum dot in a GaAs matrix. The emission lines arc ascribed to various cxcitonic complexes as exciton (X). bicxcilon (XX). positively charged bicxciton (XX+). or positively charged exciton (X+). In all cases an electron rccombincs with a hole where the Coulomb interaction with the additional charge carriers gives rise to an energy shin. (Reprinted with permission from [4.1]. © 2006 Wilcy-VCH)

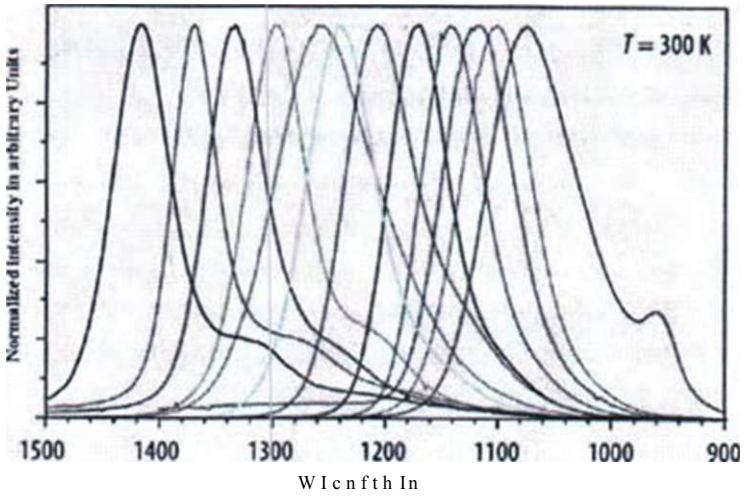

Fig. 4.9 By variation of size, shape, and composition ofquantum dots the wavelength of the emission can be selectively modified over a wide range as shown for In(Ga)As quantum dot ensembles embedded in a GaAs matrix. (Reprinted with permission from [4.1]. © 2006 Wilcy-VCH)

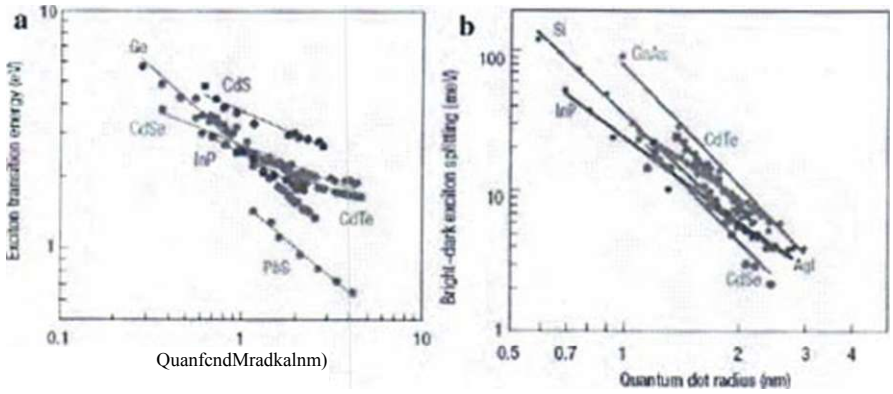

Fig. **4.10** **(a)** Size tuning of excitation energies for various quantum dot materials: Gc calculated by ab initio theory; CdSc. CdS. and CdTc measured at 250 K: PbS measured at 293 K. and InP measured at 10 K. (b) Data of bright-dark exciton splitting representing the exciton exchange interaction in quantum dots of Si (calculations). InP (measured at 10 K), GaAs (calculations). CdTe (measured at 10 K). AgI (2 K), and CdSc (10 K) (for references sec (4.2)). (Reprinted with permission from [4.2]. © 2006 Nature Publishing Group)

For single-photon and entangled photon sources and photon detectors based on quantum dots, the reader is referred to Sect. 7.4. Quantum dot lasers are discussed in Sect. 7.5.

4.1.4 Colorful Nanoparticlcs

Nanoparticlcs or nanoparticle ensembles may give rise to colors, covering the entire visible spectrum (Fig. 4.11). These effects may be used for biomedical detection, sensors, color displays, etc.

Flgi **4.11** Color variation of solutions of nanoparticles in dependence of size, shape, oxidation state, or external magnetic field) (a) Fluorescence of CdSe-ZnS core-shell nanoparticlcs, after cxcitation at a = 470 nm. i&lepcndcncc of particle size, showing the characteristic blue shift with decreasing particle size [4.17]. (b) Size, shape, and composition of metallic nanocrystals can be controlled and manipulated to produce nanoparticlcs with distinct light-scattering profiles [4.18]. (c) Carbon nanoparticles produced in the flame of a candle show luminescencc in the visible range of light depending on the particle size [4.19. 4.20]. (d) Photos of colloidal photonic crystals of superparamagnetic nanoparticles in solution formed in an external magnetic field which increases from the *right* to the *left* [4.21]. (c) Schematic illustration of a polyaciylatc-capped I-^Oj colloidal nanocrystaJUclustcr [4.21]. (0 Hysteresis loop of 180 nm FC3O4 colloidal nanocrystal clusters (CNCs) measured at room temperature, showing superparamagnetic behavior [4.21]. **(g)** TEM image of polyacrylatc-cappcd FcjOj colloidal nanocrystal cluster: scalc bar: 100 nm [4.21]. (Reprinted with permission from [4.17] **(a).** [4.18] **(b).** [4.19] (c). and (4.21) **(d-g).** © 2005 Nature Publishing Group **(a),** © 2005 American Chemical Socicty (b), © 2007 Nature Publishing Group (c). and © 2007 Wiley-VCH **(d-g))**

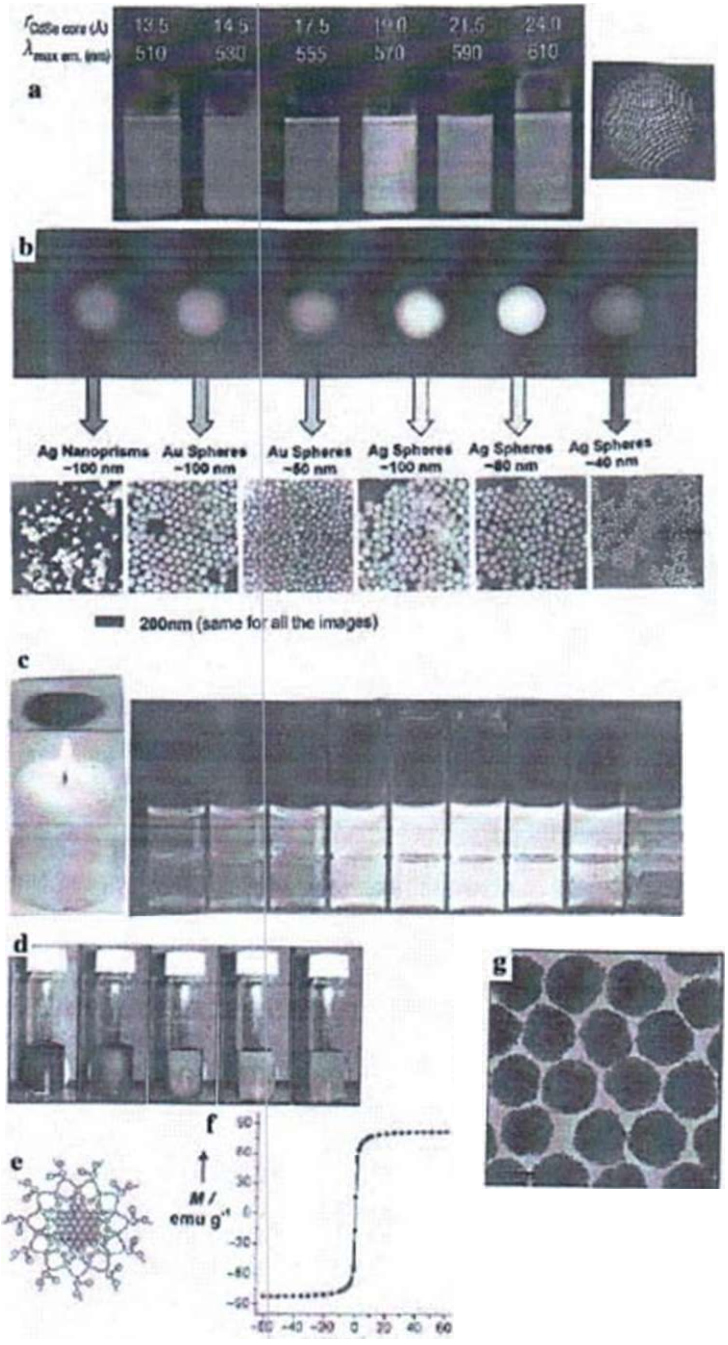
13.5
14.5
17.5
19.0
21.5
24.0
510
530
555
570
590
610
a
b
Ag Nanoprisms ~100 nm
Au Spheres ~100 nm
Au Spheres ~50 nm
Ag Spheres ~100 nm
Ag Spheres ~80 nm
Ag Spheres ~40 nm
200nm (same for all the images)
c
d
e
f
M / emu g-1
g

In *semiconductor nanoparticles* (quantum dots), where the optical response is due to the excitation of single electron-hole pairs, the wavelength of light emission (fluorescence. Pig. 4.11a) can be controlled by the size of the particle when this compares with the electron wavelength, so that the electron motion is "confined" by potential barriers in all three dimensions. This was followed closely by the realization that quantum dots, with the typical size of a protein, could be used for biological labeling [4.22, 4.23] as very stable light emitters with a larger linear absorption cross section for excitations compared with phycoerythrin and orders of magnitude larger cross section for two-photon excitation compared with conventional organic chromophores, where the optical response is due to the excitation of single electron-hole pairs (4.24].

In *metallic nanoparticles* (4.25, 4.26], incident light can couple to the plasmon excitation of the metal (sec Sect. 7.6) which involves the light-induced motion of all the valence electrons (4.27]. Thus, the cross section for clastic light scattering from a 50-nm gold nanocrystal can be a million-fold larger than the cross section of even a quantum dot chromophorc. It has been shown that plasmon resonance is strongly dependent on shape and size of the nanoparticles (Fig. 4.1 lb). Using specific organic molecules or DNA, it appears possible to design discrete aggregates of nanoparticles, in which the spectra will depend sensitively on the particle arrangement, providing a rich system for detection. The electromagnetic field in the near-field region around a metallic nanoparticlc is greatly enhanced, providing new mechanisms for detection (see Sect. 7.6). When gold nanoparticles arc located close to each other, their plasmon resonances can couple, shifting the plasmon resonance to higher energy. This change in optical response can be used to sensitively detect nucleic acids (4.28]. The large lield enhancement in the vicinity of gold nanocrystals is well known to lead to the surface-enhanced Raman scattering (SERS). This makes it possible to detect a wide range of biological macromoleculcs through binding events involving gold nanocrystals that have been coated with specific molecules that offer a distinct Raman signature (see [4.24]).

Carbon nanoparticles from candlelight. From the soot of a candle flame, solutions containing 1-nm carbon nanoparticles can be deduced [4.19, 4.20] which in ultraviolet light luminesce with yellow or blue light (Fig. 4.11c) depending on whether the group used nitric acid (yellow) or aqueous hydrogen peroxide and acetic acid (blue) as an oxidizing agent. The acid oxidation step, therefore, is the key to enriching the soot with luminescent, hydrophilic, and individually dispersed carbon "nanoparticles with carbonyl groups on their surfaces.

*Photonic crystals of superparamagnetic nanopart'i*clcs. Photonic crystals are media with artificially designed regions of varying index of refraction in order }to control the density of photon states (4.29]. Photonic crystals can be fabricated by self-assembly from monodispcrsc nanoparticles. It is desirable from the envisioned applications that a photonic crystal possesses a tunable stop band yielding a variable color scale in the visible range that can be conveniently controlled by external stimuli. Solutions of polyacrylate-capped superparamagnetic imagnetite **(FC3O4)** colloidal nanocrystal clusters (CNCs; Fig. 4.11 g) can form photonic crystals in an external magnetic field (4.21]. Each cluster with a size of 120 nm is composed of many magnetite crystallites of approximately 10 nm.

thus retaining superparamagnetic properties at room temperature. The Fe304 CNCs readily self-assemble in an aqueous solution in the field of an external FeNdB magnet (see Sect. 1.5). The light intensity peak resulting from the diffraction of (111) planes blue shifts from 730 to below 450 nm (Fig. 4.1 Id) as the magnetic field increases from 8.8 to 35.2 mT by moving the magnet to the sample (3.7-2.0 cm) with a decrease of the interplanar spacing from 274 to 169 nm. Larger clusters 170 nm) diffract red light, whereas smaller clusters diffract blue light. The change in diffraction wavelength rcversibly responds to a 2 Hz periodic magnetic field. The 3D order of the photonic crystal in the magnetic field is the balanced result of the interparticlc electrostatic repulsive force due to the polyacrylate capping of the superparamagnetic clusters and the attractive magnetic forces exerted in the external magnetic Held. These forces are estimated to be 10^{-12} N [4.21 J.

4.1.5 Double Quantum Dots for Operating Single-Electron Spins as Qubits for Quantum Computing

The use of quantum mechanical:superposition states and entanglement in a computer can theoretically solve important mathematical and physical problems much faster than classical computers (see |4.30|). Electron spin states (see Sect. 1.4) were identified early as an attractive realization of a quantum bit (qubit) [4.31] in a quantum computer, because they are relatively robust against dccoherence (uncontrolled interaction with the environment). Advances in the field of semiconductor quantum dots have made this system a valuable host for the electron spin. The quantum state of the electron spin can be coherently controlled [4.30] by applying short bursts of an oscillating magnetic field giving rise to oscillations of the spin state (so-called Rabi oscillations), which can be detected by measuring the dot current (Fig. 4.12c).

The spin state of a single electron confined in a double quantum dot can be controlled via electron spin resonance (ESR). In a double dot GaAs/AlCiaAs system (see Fig. 4.12a), spin flips can be detected through the transition of an electron from one dot to the other (see [4.30]) rather than between a dot and a reservoir, as would be the case for a single dot. This has the advantage that there is no need for the electron spin Zeeman splitting to exceed the temperature of the reservoir and that the experiment can thus be performed at a smaller sialic magnetic field and consequently with lower excitation frequencies (sec [4.30]). Furthermore, in a double dot, single-spin operations can in future experiments be combined with two qubit operations to realize universal quantum gates (see |4.30|).

To deteci the ESR-induced spin rotations, electrical transport measurements through the two dots (Fig. 4.12a) in the spin blockade regime are used [4.30] where current flow depends on the relative spin state of the electrons in the two dots. The device is operated so that current is blocked owing to spin blockade (Fig. 4.12b), but this blockade is lifted if the ESR condition $hf_K = gnuBcxi$ is satisfied. Herc,$/_{ac}$ is the frequency of the oscillating magnetic field $/i_{ac}$. Mb the Bohr magneton, and g the electron spin ^-factor. The spin blockade regime is accessed by tuning the gate voltages such that one electron always resides in the right dot and a second electron^

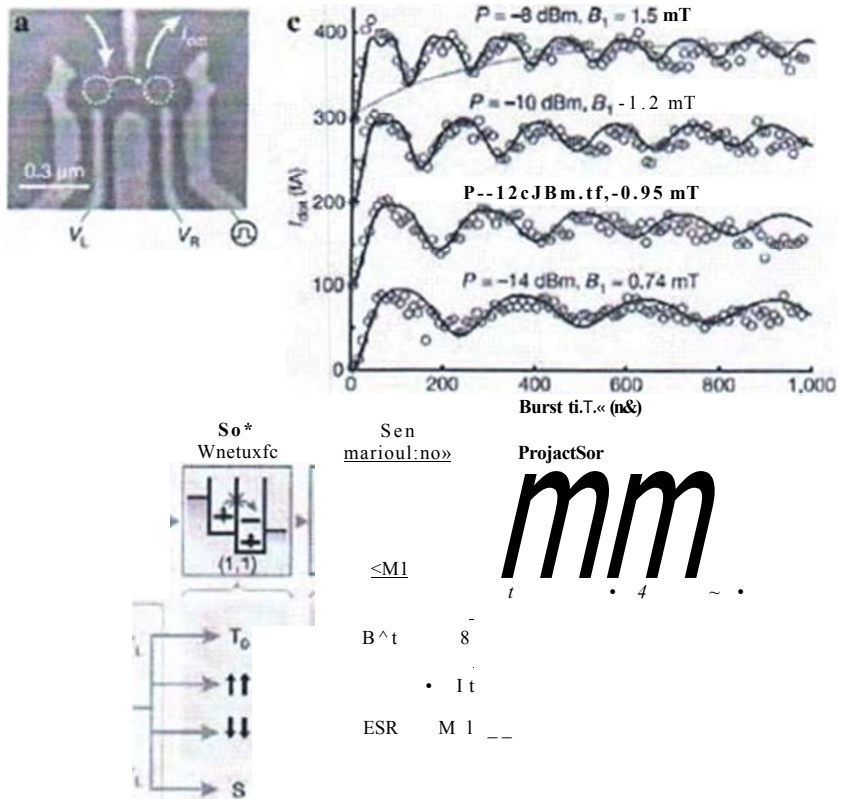

Fig. **4.12** **(a**-b) Dcvice and clcctron spin rcsonancc (ESR) dctcction schcmc for operating single-elcctron spins as qubits for quantum computing, **(a)** Scanning electron micrograph (SEM) of the device with TL/Au gates deposited on lop of a GuAs/AlGaAs hclcrostructure containing a 2D clcc-tron gas. *White arrows* indicate current flow through the two coupled dots (*dotted circles),* (b) Diagrams illustrating thc^ansport cycle in the spin blockade regime, which is described via the occupation numbers (m. n) of the left and right dots as (0. 1) -* (1. 1) (0. 2) -* (0. l)^When an electron enters the left dot (with rate I\) starting from (0. 1), the two-electron system that is formed can be either a singlet S(1. 1) or a triplet T(1, 1). FromS(1, 1). further current (low is pos-sible via a transition to S(0. 2) (with rate F_m). When the system is in T(1. 1). current is blocked, (c) Coherent spin rotations. The dot current - reflecting the spin state at the end of the radiofrequency (RT) burst - oscillates as a function of RF burst length. The period of the oscillation increases and is more strongly damped for increasing RF power P. (Reprinted with permission from {4.30]. <D 2006 Nature Publishing Group)

can tunnel from the left reservoir to the left dot (Fig. 4.12a, b). If this electron forms a double-dot singlet state (f j) with the electron in the right dot, it is possible for the left electron to move to the right dot and then to the right lead, since the right dot singlet state is energetically accessible. If the electrons, however, form a double-dot triplet state (I f or 44), the left electron cannot move to the right dot because the right dot's triplet state is much higher in energy. The electron also cannot move back to the lead and therefore further current flow is blocked as soon as any of the (double-dot) triplet slates is formed [4.30].

The oscillating magnetic liclds for driving the spin transitions arc generated by applying a radiofrequency (RF) signal. As shown in Fig. 4.12c the dot current oscillates periodically with the RF burst length. This oscillation indicates that driven, coherent electron spin rotations, or Rabi oscillations, have been performed [4.30]. This single spin rotation offers new opportunities, such as measuring the violation of Bell's inequalities or the implementation of simple quantum algorithms [4.30].

Fast quantum control of a single quantum dot spin has been achieved by using ultrafast optical pulses, promising nearly 10^s gate operations within the qubit's coherence time of about 3 JAS [4.32].

4.1.6 Quantum Dot Data Storage Devices

Future quantum dot storage devices may combine the properties of dynamic random access memories (DRAM) with rapid data access and the properties of non-volatile Flash memories. Recent studies of quantum dots (see [4.1]) have demonstrated charge storage times of more than 5 ms which may be extended into the 5 s range [4.1]. Addressing of single quantum dots seems to be possible [4.1].

4.2 Nanowires and Metamaterials

Nanowires can be prepared from metals, semiconductors, organic molecules, etc. and offer prospects in mechanical, electronic, optical, or medical applications. Here, we discuss metallic nanowires and their recent introduction into metamaterials for the generation of negative refractive index materials in the optical range, semiconductor quantum wires for transistors, biosensors, light sources, detectors, and molecular nanowires. Finally, the conduction of single rows of atoms is considered.

4.2.1 Metallic Nanowires

Nanowires can be grown from Cu, Ag, and Au (see [4.33]). Copper nanowires (Fig. 4.13a) grown by chemical vapor deposition (CVD) with a fivefold twinned structure are suitable for integration into devices. The confinement for the ID growth arises from a passivation of the {100} side planes of the wires by phosphate ligands derived from the precursor compound, so that the growth only occurs on the capping {111} planes. These Cu nanowires may be useful as a promising electron emitter [4.33]. Bismuth nanowires (Fig. 4.13b) can be grown by the anodic alumina membrane (AAM) template technique [4.34] (see Sect. 3.9). Bismuth is a semimela! with a small effective electron mass, long carrier mean free path, and a small energy overlap between the conduction and the valence band, which can lead to a scmimetal-semiconductor transition in Bi nanowires with decreasing wire diameter (sec [4.34]). The fabrication of Bi nanowires has attracted attention due to potential application in thermoelectric dcvices (see [4.34]). Alloy nanowires

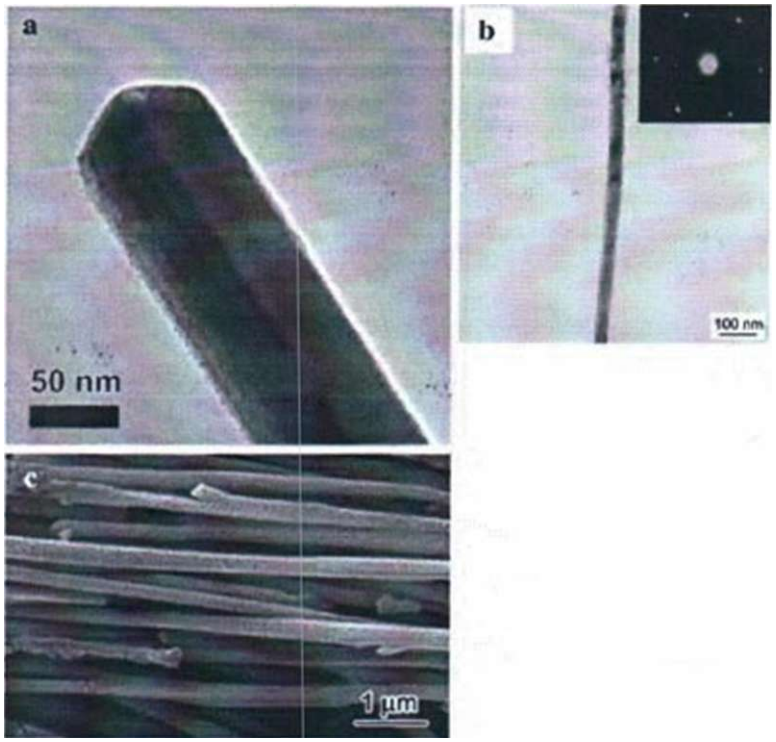

Fig. **4.13** **(a)** Transmission electron micrograph (TEM) of a Cu nanowire [4.33]. (b) TEM of a Hi nanowire [4.34]. (c) Scanning clcctron micrograph of Pd-Ag nanowires [4.35J. (Reprinted with permission from [4.33] (•), [4.34] (b). and [4.35] (c). © 2008 WUcy-VCH **(a).** © 2007 Chinese Society of Metal (b). and © 2008 Chinese Society of Metal (c))

of Pd-Ag (Fig. 4.13c) can be fabricated by the AAM template technique and are expected to be employed for hydrogen sensors [4.35].

Mechanical properties. The mechanical properties of gold nanowires are found to change substantially with the diameter of the wire. Whereas wires with a diameter of 70 nm exhibit a yield stress of 600 MPa, this increases to 1400 MPa for a 30 nm diameter and increases further, down to 5 nm. Transmission electron microscopy shows that deformation is caused by dislocation motion and possibly twinning |4.36]. Nanoporous gold - obtained from leaching Au-Ag alloys - with a relative density of 0.2-0.45 and a ligament size of 5-500 nm shows a high strength of 1-15 GPa |4.36].

4.2.2 Negative-Index Materials (Metarnaterials) with Nanostructures

Metallic nanowires 14.37-4.39] and nanolaycrs of metals and insulators [4.401 or of semiconductors [4.41] are the building blocks for the recently developed

2D or 3D negative-index materials (NIMs) or "melamatcrials." The NIMs have negative electrical permittivity (e), negative magnetic permeability (/z), and negative index of refraction (n) at a common frequency band (for introductory reviews sec [4.42-4.44]. Although it has been well known how to obtain a $e < 0$ material easily, e.g., by using wire arrays (see 14.45]), the realization of a $n < 0$ response (especially at high frequencies) has been a challenge, due to the absence of naturally occurring magnetic materials with negative //. Materials with $/i < 0$ can be realized [4.46] by arrays of metallic rings with gaps, called split-ring resonators (SRR), which exhibit a $// < 0$ regime in the vicinity of a magnetic resonance frequency. Artificial materials with negative e and n have been predicted (see [4.47]) to have the remarkable property of a negative refractive index: a light ray entering such a NIM bends the "wrong" way from the surface normal (see Fig. 4.14). Making use of NIM materials, the realization of invisibility cloaks (see [4.49]) and of "perfect" lenses is envisaged.

The existence of NIMs has been initially demonstrated in the gigahertz frequency range (see [4.45]) and shifted to the optical region [4.37, 4.39] by the use of pairs of finite length nanowircs (cut wires) and the fishnet topology (sec Fig. 4.15a) in 2D arrays. The resonance at 720 nm in Fig. 4.15b is a magnetic resonance, yielding a negative refractive index (see [4.39]). 3D NIM materials [4.38, 4.40] which arc required for practical applications have been developed from 3D fishnet materials

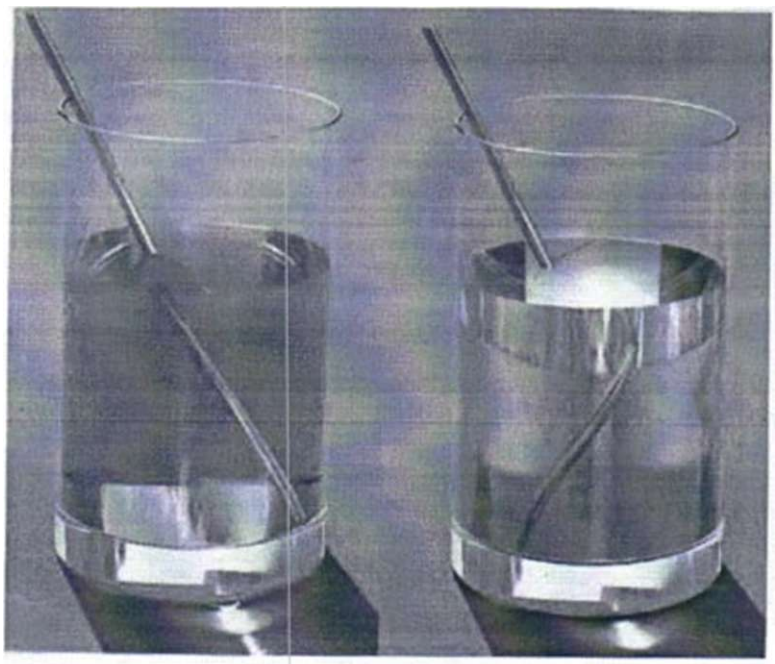

Fig. 4.14 The simulation of a metal rod in a glass filled with water *(left,* index of refraction of water, n = 1.3) would be drastically changcd for a fictitious liquid with a negative index of refraction, $n = -1.3$ *(right).* (Reprinted with permission from [4.48]. © 2006 Wiley-VCII)

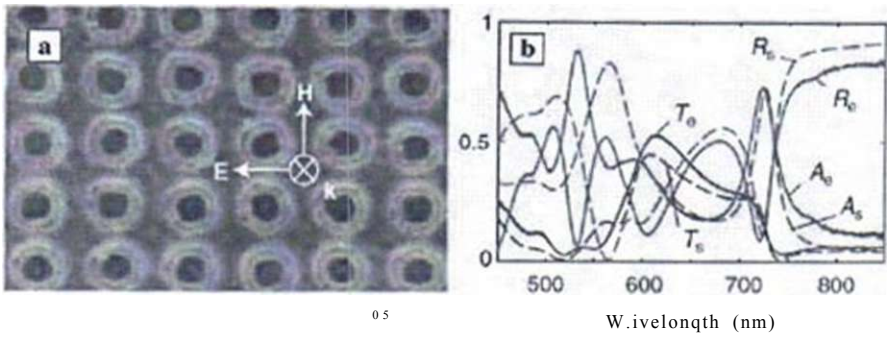

Fig. 4.15 (a) Scanning electron micrograph (SEM) and (b) experimental and simulated spectra of a double-negative negative-index fishnet material (DN-NIM) silver sample. *H. E.* and *k* define the directions of the magnetic field, the electric field, and the wave propagation, respectively. *T* is transmittancc. *R* is reflectance, and is absorbance. with *solid lines* and subscript *e* representing experimental data and *dashed lines* and subscript s representing simulated data. (Reprinted with permission from [4.39]. <0 2008 Materials Research Society)

and gold nanowire 3D-SRR arrays (see Fig. 4.16). where plasmon-like oscillations couple between adjaccnt SRRs. With the 3D fishnet material negative refraction of a laser beam, i.e., "wrong" deflection (Fig. 4.16b), can be demonstrated. 3D meta-materials with a tunable plasma frequency in the visible regime were prepared from InGaAs/GaAs/Ag multilayers with a single-layer thickness of 17 nm [4.50].

4.2.3 Semiconductor Nanowires

Semiconductor nanowires are emerging as a powerful class of materials that, through controlled growth and organization, are opening up novel opportunities for nanoscalc electronic and photonic devices [4.51].

A host of techniques are available for growing semiconductor nanowires (see Sect. 3.3). Homogeneous quantum wires (Fig. 4.17a) can be grown with diameters down to 3 nm with specific dopants to control their electronic properties. Recently controlled growth of axial (Fig. 4.17b) and radial heterostructures (Fig. 4.17c) has been achieved where the composition or doping is modulated on an atomic level along or perpendicular to the axes of quantum wires, respectively. This wide range of controlled structures enables the development of powerful and unique nanoscale electronic and optoelectronic devices for future applications.

Mechanical properties. The mechanical properties of semiconductor nanowires are of interest given the potential applications in electronic and electromechanical devices. Zinc oxide is a semiconductor with a direct wide band gap of 3.37 eV. piezoelectric properties (sec [4.52]), good biocompatibility, and therefore a number of application prospects (see [4.52]). Whereas the Young's modulus of ZnO turns out to be independent of diameter, the ultimate strength increases for small diameter wires and exhibits values up to 40 times that of the bulk [4.52].

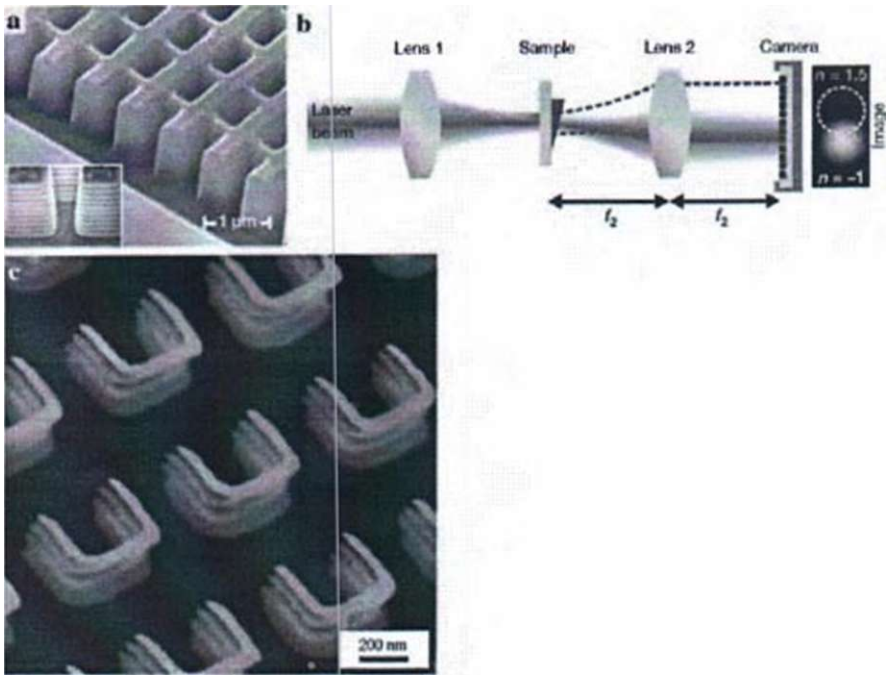

Fig. 4.16 (a) Scanning electron micrograph (SHM) of a 21-layer fishnet structure with the side ctchcd. showing the cross section. T;ie structure consists of alternating layers of 30 nm Ag and 50 nm MgF_2. The *inset* shows a cross section of the pattern, (b) Experimental setup for a laser beam refraction measurement. The focal length of lens 1 is 50 mm and that of lens 2 is/2 = 40 mm. Lens 2 is placed in a 2f configuration, resulting in the image at the camera position. A prism of the mctamalcrial refracts the laser beam with a negative index of refraction n = -1 for wavelengths between 1.500 and 1.800 nm. The *dashed circle* indicates the expected image of the beam for a positive index of refraction n = 1.5 [4.40]. (c) Field-emission scanning electron micrographs *(oblique view)* of a 3D four-layer gold split-ring resonator (SKR) array that mimics magnetism at high frequencies [4.38]. (Reprinted with permission from the [4.40] (a) (b). and [4.38] (c). © 2008 Nature Publishing Group)

Field-effect transistors: It has been shown [4.51] that quantum wire materials including Si, Ge, and GaN can be prepared with complementary n-type and p-typc doping. For example, studies of quantum wires fabricated from boron (phosphorus)-doped silicon have been used in field-effect transistors (FETs) that are switched on with a negative (positive) gate voltage characteristic of p-(n-) channel FETs (Fig. 4.18). In these quantum wires long mean free paths of carriers have been observed and the high quality of these wires has been demonstrated [4.51].

From these quantum wires, logic gates such as inverters or oscillators can be built. By the crossed quantum wire architecture [4.51] the key device properties can be designed making use of a bottom-up assembly of two nanowire components and not of top-down lithography. This concept was first demonstrated using a Si

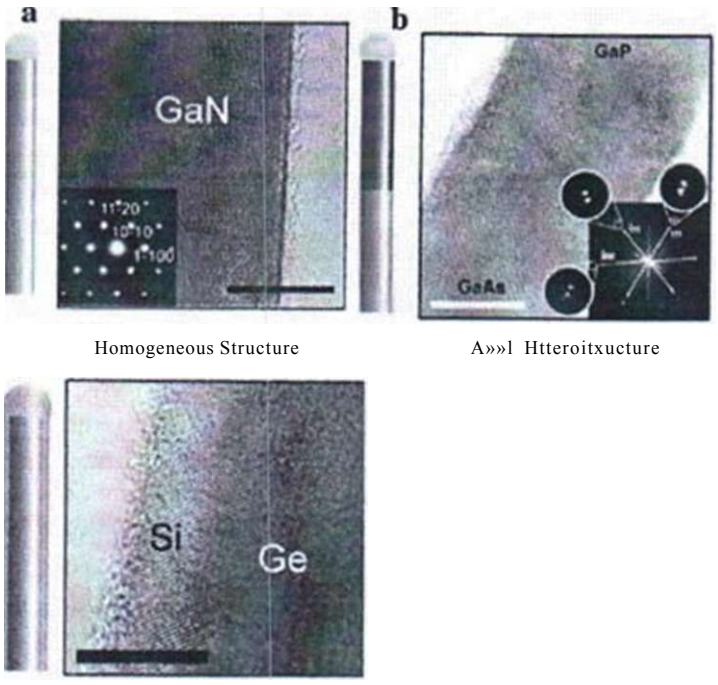

Homogeneous Structure A»»l Htteroitxucture

Radial Heteraitriirnire

Fig. 4.17 Semiconductor nanowires and hetcrostructurcs. schematics, and transmission electron micrographs (TEM). (a) Uniform singlc-crystal GaN quantum wire, (b) axial GaP/GaAs hct-erostructure, and (e) radial (core/shell, core/multishell) heterostnicture. All scale bars 10 nm. (Reprinted with permission from (4.51]. © 2006 Elsevier)

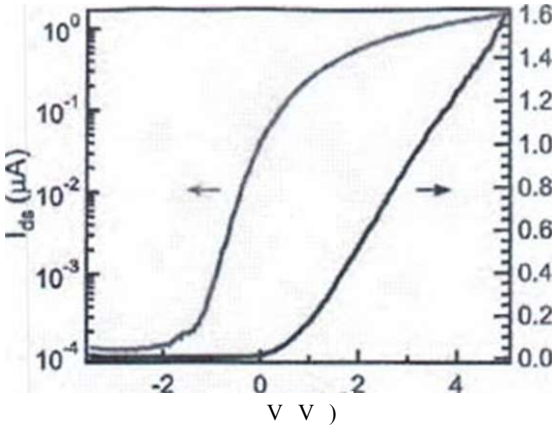

Fig. 4.18 Electrical transport characteristics of a lightly doped (Si/P=4000) 20 nm n-typc Si quantum wire ficld-effect transistor (FET) device with the drain-sourcc currcnt versus the gate voltage Vj, on linear and logarithmic scales. (Reprinted with permission from [4.53]. © 2004 Wilcy-VCH)

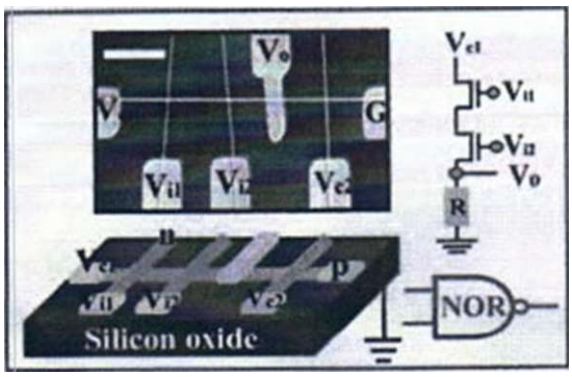

Fig, 4.19 Crossed quantum wire electronic device. I-oft: Schematic of a logic NOR gate constructed from a Si wire crosscd by three GaN wires. *Insets* show a scanning electron micrograph of the device (scale bar: 1 |im) and a symbolic electronic circuit. (Reprinted with permission from [4.51]. © 2006 Elsevier)

quantum wire with a thin SiCb dielectric shell as the channel and GaN quantum wires as gale electrodes to fabricate both NOR logic gate structures (Fig. 4.19) and basic computation devices [4.54].

Biosensors: Quantum wire FETs have emerged as powerful sensors for label-free detection of biological and chemical species [4.51]. Binding of molecules to the surface of the FET is mimicking the application of a gate voltage which leads to the depletion or accumulation of carriers and subsequent specific changes in the quantum wire conductance.

For example, for the specific detection of a particular type of viruses (sec Fig. 4.20a), the small sizes and the high performance of the quantum wire FETs with attached specific antibody receptors yield a high sensitivity, as shown in the FET conductance, upon virus binding and unbinding (Fig. 4.20a). The conductance of a second quantum wire with antibodies not specific to the present virus does not change.

For the diagnosis of prostate cancer, the multiplexed real-time detection of three cancer marker proteins, f-PSA (prostate specific antigen), CEA (carcinocmbryonic antigen), and mucin-1 was demonstrated [4.56] making use of Si quantum wire devices functionalizcd with monoclonal antibodies (mAbs) for f-PSA (quantum wire 1), CEA (quantum wire 2), and mucin-1 (quantum wire 3) (see Fig. 4.20b). These cancer marker proteins can be identified by the subsequent concentration-dependent conductance changes on the differently functionalizcd wires upon sequential delivery of the different protein solutions (see Fig. 4.20c). These results show multiplexed real-time, label-free marker protein detection with sensitivity to the fcmtomolar level and complete selectivity which may offer a significant improvement of future health care.

Light-emitting diodes (LEDs). lasers, and photodetectors: Crosscd nanowires can also be used to fabricate nanoscalc p-n diodes for, e.g., band-edge emission LEDs at the nanoscale cross-points (Fig. 4.21a). The capability to assemble a

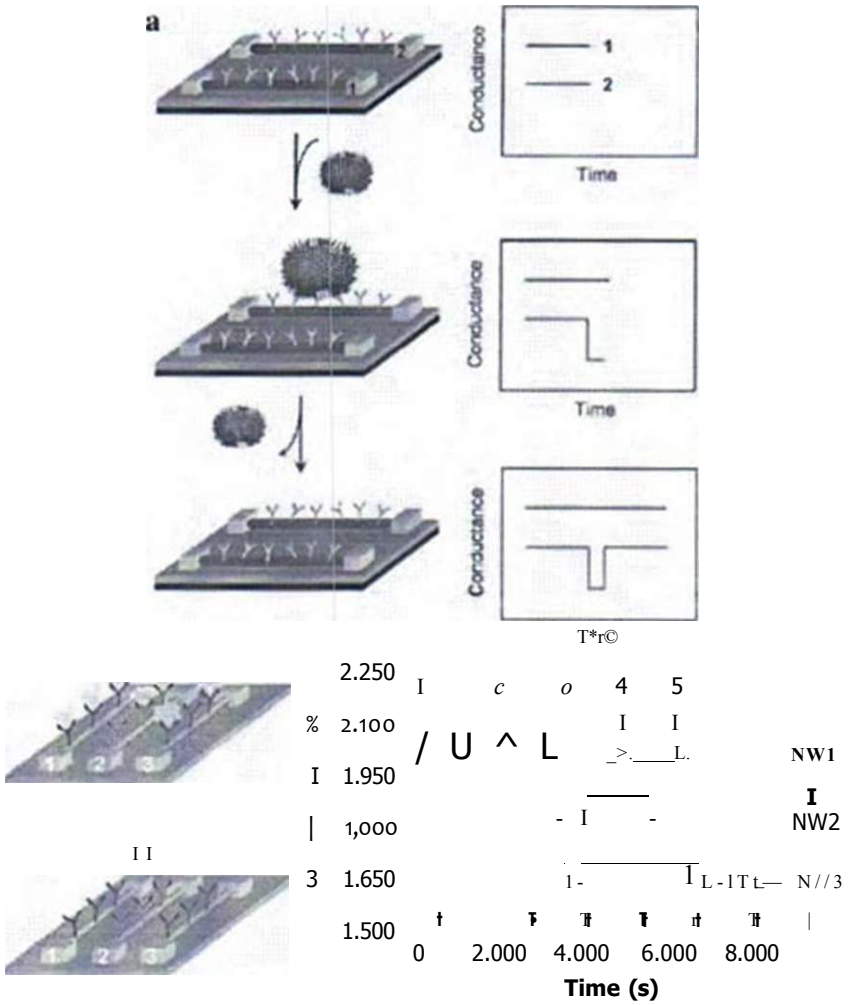

Fig. **4.20** **(a)** Schcmalics of quantum wire-based detection of single viruses making use of two nanowirc devices. 1 and 2. where the nanowircs are modified with different antibody receptors. Spccitic binding of a single virus to the reccptors on quantum wire 2 produces a conductance change characteristic of the surfacc charge of the virus only in quantum wire 2. When the virus unbinds from the surfacc the conductance returns to the initial value **[4.55]. (b)** Schematics illustrating multiplexed protein detection by three Si quantum wire devices in an array. Devices 1. 2. and 3 arc made of similar wires which arc selectively functionalized with distinct monoclonal receptors specific to three different cancer markers, (c) Time-dependent conductance for simultaneous detection of prostate antigen (PSA), carcinoembryonic antigen (CEA), and mucin-1 on a p-Si wire array in which the wires 1. 2. and 3 arc functionalized with monoclonal receptors for PSA. CEA. and mucin-1, respectively. Protein solutions were delivered sequentially on the wire array: (1) 0.9 ng/ml PSA. (2) 1.4 pg/ml PSA. (3) 0.2 ng/ml CEA. (4) 2 pg/ml CEA. (5) 0.5 ng/ml mucin-1. and (6) 5 pg/ml mucin-1. Buffer solutions were injcctcd following each protein solution at points indicated by black arrows [4.51]. (Reprinted with permission from [4.55] (a) **(b)** and [4.51] (c). © 2004 National Academy of Scicnccs. USA **(a) (b)** and © 2006 Elsevier (c))

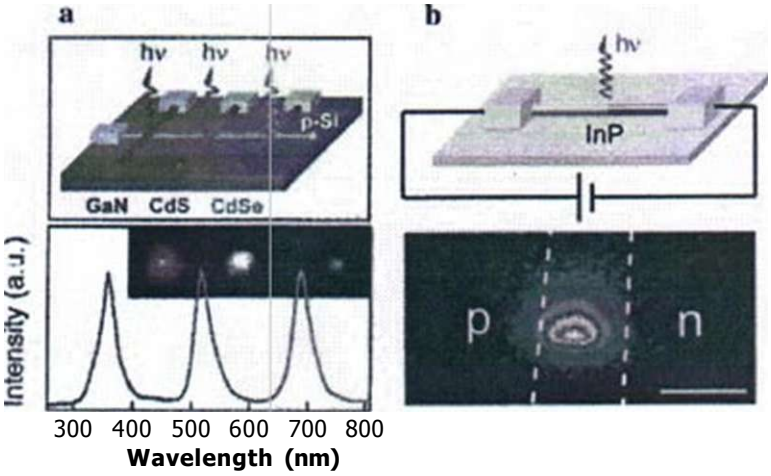

Fig. 4.21 **(a)** Schcmatic of the electroluminescence of a tricolor nano light-emitting diode (LED) array of a p-typc Si quantum wire crossed with n-typc GaN. CdS. and CdSc wires, **(b)** Schcmatic of a modulation-doped InP quantum wire LED and image of the emission from the device. The *dashed while lines* indicate the edges of the electrodes. Scale bar: 3 nm. (Reprinted with permission from[4.51]. © 2006 Elsevier)

wide range of different n-type direct band gap quantum wires of GaN (ultraviolet), CdS (green), and CdSc (near infrared) with p-type Si quantum wires has enabled the simple creation of multicolor light-emitting diodes (LEDs) on a single substrate in a manner not possible formerly. Light emission can also be obtained at p-n interfaces of modulation doped InP quantum wire axial heterostructures (Fig. 4.21b).

A nanoscale electronic injection laser has been constructed from n-type CdS quantum wires assembled unto p-typc Si electrodes (4.57J. This device shows a superlincar increase in the electroluminescence intensity at the end of the quantum wire together with peak narrowing (Fig. 4.22a) when the injection current increases above the threshold.

Photodctcctors for use in integrated photonics can also be fabricated from crossed quantum wire p-n junctions. Avalanche multiplication of the photocurrcnt has been detected in nanoscale p-n diodes of crossed Si/CdS quantum wires (Fig. 4.22d) 14.581. These nanoscale avalanche photodiodes exhibit ultrahigh sensitivity with detection limits of less than 103 photons and sub-wavelength spatial resolution of 250 nm.

Manipulation of quantum wires by means of optical traps. For the manipulation of quantum wires for further integration, an optical trap can be employed (4.59). This makes use of the effect that a light beam can exert a force on a particle and therefore can grip a quantum wire and transport it into a desired location (Fig. 4.23a). By this technique, e.g., a GaN quantum wire could be transported close to a human cervical cancer cell and attached there (Fig. 4.23b).

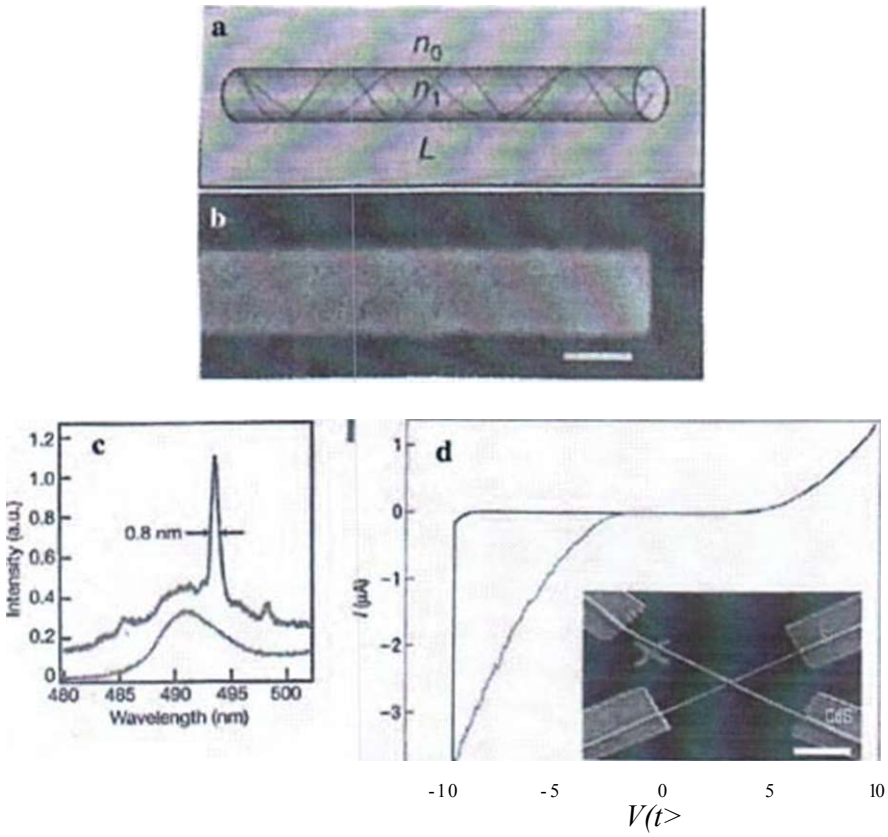

Fig. 4.22 **(a)** Schematics of a Fabry-Pcrot optical cavity of a quantum wire as an optical waveguide and with cleaved ends defining the Fabry-Pcrot cavity, (b) SF.M image of a cleaved CdS quantum wire end. Scale bar: 100 nm [4.57J. (c) Electroluminescence spectra from the end of an n-CdS quantum wire laser deposited on a p-Si substrate with injection currents below (200 n A. *lower curve)* and above (280 jiA, *upper curve)* the lasing threshold. The spectra arc offset by 0.1 intensity for clarity, (d) I-V characteristics of an n-CdS/p-Si crosscd quantum wire avalanche photodiode in dark (step function line) and under illumination (*curved line):* the *inset* represents the optical micrograph of an array of an n-CdS quantum wire crossing a p-Si quantum wire: the larger rectangular features are the metal contacts. Scale bar. 10 jxm [4.58]. (Reprinted with permission from [4.57] **(a) (b)** and [4.58| (c) **(d).** © 2003 Nature Publishing Group **(a) (b)** and © 2006 Nature Publishing Group (c) **(d))**

4.2.4 Molecular Nanowires

For the bottom-up approach of designing electronic components for future information technology or signal conductance in artificial nerves, the exploitation of the features of organic molecules and molecular wires are of interest. Poly(z-vinylpyridine) nanowires were loaded with Au, Ag, or CdS nanoparticles [4.60]. Highly conductive and relatively long (—40 nm) molecular wires can be synthesized by the coordination of teq>yridine-based ligands to metal ions such as Fe or

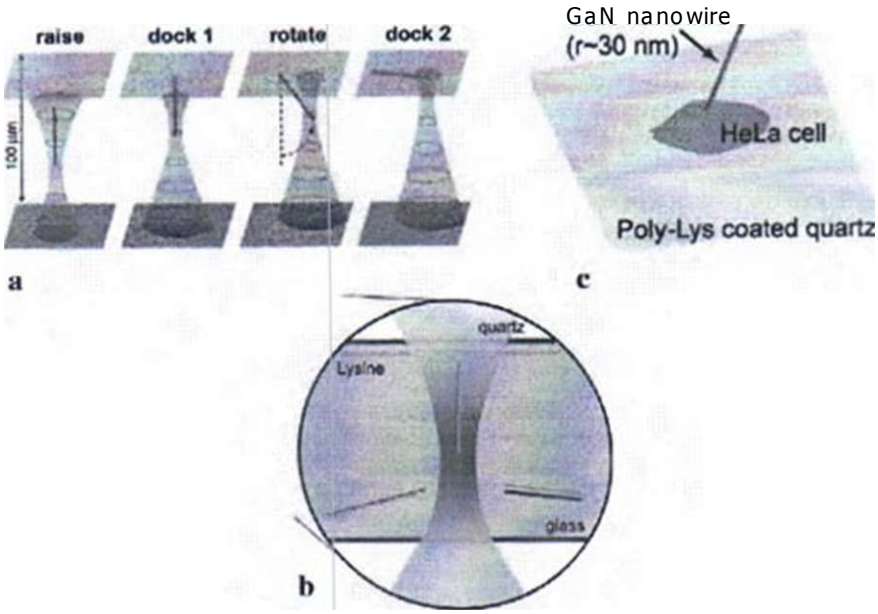

Fig. **4.23** (a) Schcmatic of a four-step nanowire positioning procedure in an optical trap aqueous chamber with a light beam, (b) Schematic of the experimental chambcr cross section. The top surface is a 170 |im quart/ covcrslip *(blue)* coated with lysine *(green)* and the bottom surfacc a glass covcrslip. The quantum wires sink to the bottom and can be picked up there by the light beam, (c) Schcmatic of a GaN quantum wire attached to a human cervical cancer cell by optical trapping. (Reprinted with permission from [4.59]. © 2006 Elsevier)

Co |4.61]. By Tt-stacking of 6,13-bis(methylthio)pcntaccne, molecular nanowircs were self-assembled, achieving four-level switching in a multiwire transistor and demonstrating their suitability for the production of muitilogic devices [4.62].

In spite of all the present progress in quantum wire synthesis, characterization, and their attractive physical features, researchers are aware of further challenges to be overcome before nanowires are implemented in high-end products [4.63].

4.2.5 Conduction Through Individual Rows of Atoms and Single-Atom Contacts

The quantized conductance through individual rows of freely suspended Au atoms [4.64], the manipulation of these single-atom metallic wires [4.65], and the detection of the signature of the chemical valence in the electrical conduction through single-atom contacts [4.66] will be discussed in the following.

By a combination of conductance measurements and high-resolution electron microscopy [4.64], it was shown that the conductance of a single strand of gold atom (Fig. 4.24) is about equal to the conductance quantum $2e^2/h$ $13\,kST^1$)

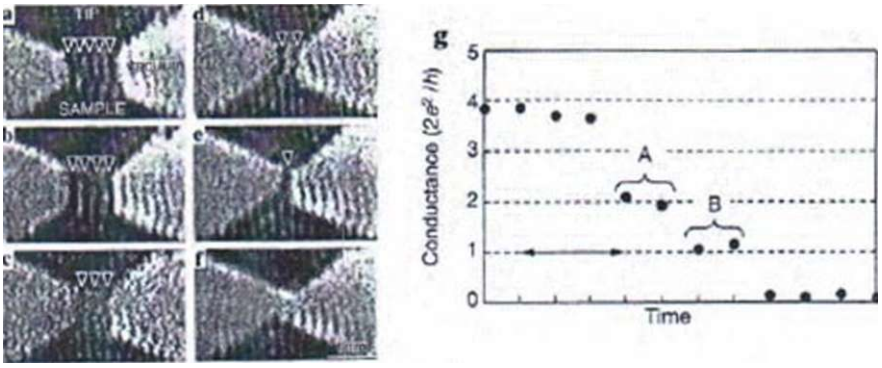

Fig. 4.24 Electron micrographs of an Au contact while withdrawing the Au tip *(top)* from the Au substrate *(bottom).* The gold contact is thinned from (a) to (c) during withdrawing and ruptured at **(f).** *Dark lines* indicated with arrow heads arc single rows of gold atoms, (g) Conductance change of a Au contact in units of $G_0 = 2e^2/h \sim$ (13 left)"' while withdrawing the lip from the substrate. (Reprinted with permission from [4.64]. <D 1998 Nature Publishing Group)

and that the conductance of a double strand is twice as large. By straining the atomic gold bridge (Fig. 4.24) the strands presenting a row of atoms each disappear one by one until the contact breaks. Simultaneously the conductance changes in units of $2e^2/h$ (see Fig. 4.24 g). The Au bridges can sustain high electrical current densities up to 8 x $IO^{14}A/m^2$ [4.65] indicating that the electron transport is ballistic without dissipation.

In chains of two atoms of the noble gas Xe the conductance is two orders of magnitude lower than $2tf^2//j$ due to the non-metallic bonding [4.67].

If the length of an atomic wire shrinks to one atom, we arrive at a single-atom contact or an atomic constriction. Experimental [4.66] and theoretical studies [4.68] show that the electrical conductance in single-atom contacts evidences the signature of the chemical valence of the metals investigated. The extended quantum states of the leads that carry the current from one bank of the constriction to the other necessarily proceed through the valence orbitals of the constriction atom. It has been conjectured that the current-carrying modes (or "channels") of a one-atom contact is determined by the number of available orbitals and so should strongly differ for metallic elements in different series of the periodic table.

The electrical conductance of a quantum coherent structure with N channels is given by the Landauer formula G = Go $T_{,,}$ [4.69] with the conductance quantum Go = $2e^2/h$ and the transmission probability $T_{,,}$ which can be derived from the nonlincarities in the current-voltage characteristics of superconducting constrictions. These nonlincarities are sensitive to the individual transmission values *[T,,]* of the channel ensemble.

It turns out that the maximum number of channels N_{max} for an atomic contact is characteristic for a given metal. For Pb three or four channels contribute to the atomic conductance where in A1 three and in Nb live channels are detected. These results support the hypothesis that N_{max} for one-atom contacts is given by the number of the valence orbitals A'orb of the central atom |4.66, 4.68].

4.3 Nanolayers and Multilayers

In this section 2D nanostructures with a confinement of the charge carriers in one dimension will be discussed. These structures which are also termed quantum wells exhibit novel electronic properties in particular in high magnetic fields, such as the integral quantum Hall cffcct (IQHE) and the fractional quantum Hall effcct (FQHE). In addition. 2D electron gases in oxide interfaces and nanomultilayers for x-ray mirror fabrication will be outlined.

4.3.1 2D Quantum Wells

When an electron is confined in a thin metal or semiconductor film where the film thickness scalcs with the dc Broglic wavelength $k = h/p$ of the charge carriers {]) - carrier momentum; h - Planck's constant), new physical phenomena occur [4.70, 4.71). For an electron the film represents a potential well (quantum well) with the width a (film thickness) and the depth c$> (work function) which may be considered as infinitely deep because <$> = 4 — *5eV* >> *kT.* In this thin quantum well the electron assumes discrete quantized energy levels

$$„ \qquad 7T^2n^2\mathrm{N}^2$$

with $N = 1, 2, \ldots$ and m the effective mass of the carrier (Fig. 4.25a).

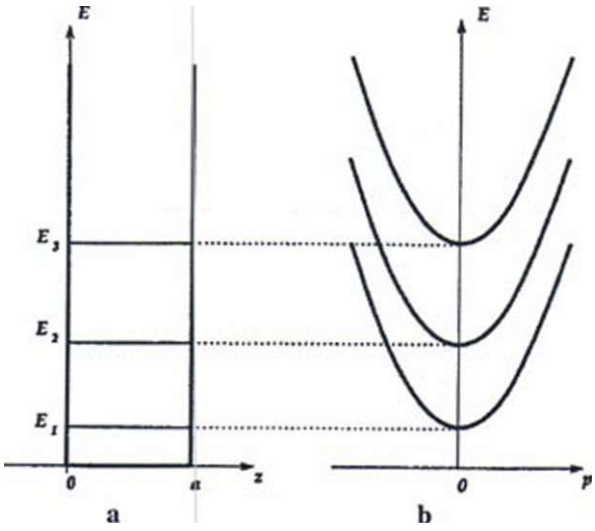

Fig. 4.25 (a) Energy spectrum of a quantum well with quantized levels for the carrier motion in r-dircction perpendicular to the plane of the quantum well and (b) taking into account additionally the in-plane carrier motion with the momentum $p = (p^*$. (Reprinted with permission from [4.701. © 1997 World Scientific)

For the total energy of an electron in a quantum well, the in-plane motion of the carriers has to be taken into account additionally, yielding the energy spectrum

$$E = E_n + \frac{p_x^2 + p_y^2}{2m}$$

with the discrete component E_n for the motion perpendicular to the film (z-direction) and a continuous component with the in-plane carrier momenta p_x and p_y (see Fig. 4.25b). This energy spcctrum gives rise to the step-like density of states in a 2D quantum well (see Sect. 1.3).

4.3.2 2D Quantum Wells in High Magnetic Fields

In the case of a magnetic licld // oriented perpendicularly to the plane of the 2D quantum well, the total energy spcctrum of the carriers including the motion in the direction of the Held // is given by

$$E = E_N + \mathrm{E}l = E_s + ti<o_c\ (M + 1/2).\ M = 0.\ 1,\ 2.\ \ldots$$

The equidistant energy levels $\mathrm{tiio_c}\{M + 1/2)$ are callcd Landau levels with the cyclotron frequency $io_c = eH/mc$ [4.70]. The most remarkable feature of this spectrum is its purely discrete character.

It is convenient to discuss the effects of 2D quantum wells in high magnetic fields employing the dimensionless filling factor

$$v = 2tt\, n_s hc/ell$$

which is the number of Landau levels completely filled by electrons at $T = 0$, where the critical fields $H^{\wedge} = 2xhcn_{\&}/eN$ correspond to integer tilling factors. Since $2nhfe = <\!\!\triangleright o$ represents the magnetic flux quantum, the filling factor $v = /;\$/\ (B/<\!\!\triangleright o)$ can alternatively be interpreted as the number of electrons per flux quantum and much of the physics of 2D electrons in a magnetic field can be cast in terms of this filling factor.

4.3.3 The Integral Quantum Hall Effect (IQHE)

Most of the experiments performed on 2D electron systems in high magnetic fields H are electrical resistance measurements [4.71]. These measurements (see inset of Fig. 4.26) yield the magneto-resistance R_{xx}, which reduces to the regular resistance in zero *11* field, and the Hall resistance R_{xy}, which increases linearly with the field in an ordinary conductor. In 1980 K. v. Klitzing [4.72] discovered novel plateaus in the Hall resistance R_{xy} of a semiconductor quantum well structure (see Fig. 4.26) and was awarded the Nobel prize in 1985. The effect is called the Integer Quantum

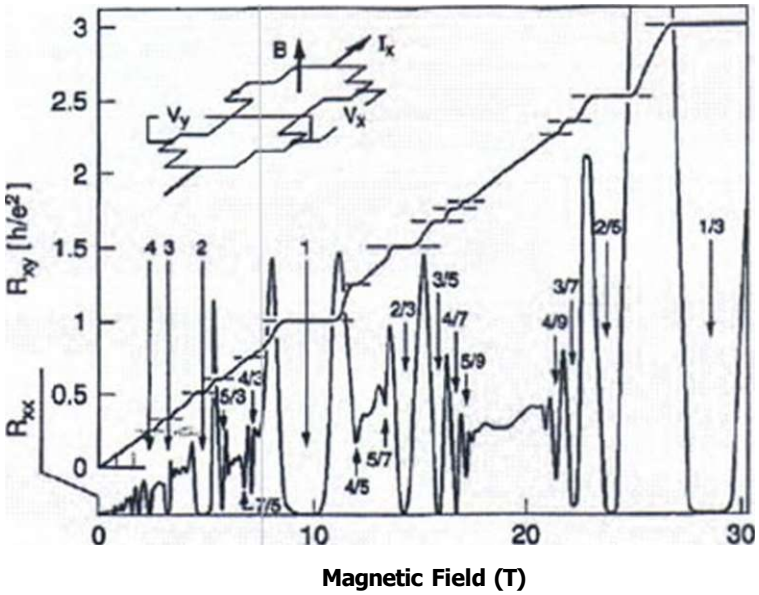

Fig. 4.26 Composite view show ing the Hall resistance $R_{xy} = V_y/I_x$ and the magnctorcsistancc $Rxx = V_x/!_x$ of a 2D electron system of the density $n = 2.33 \times 10^{11}$ cm ^{2} at $T = 85$ mK in dependence of the magnetic field //. The numbers designate the filling factor v. which indicates the degree to which the sequence of I.andau levels is filled with electrons. In contrast to a linear rise with *II.* R_{iy} exhibits plateaus, quantized to $h/(ve^2)$ with simultaneous minima in *Rxx*- The features of the integer quantum Hall effect (IQHE) result from the quantization conditions for individual 2D electrons in a II field, whereas the fractional quantum Hall effect (FQHH) is of many-particle origin. The *inset* shows the measuring geometry. (Reprinted with permission from (4.71]. © 1999 American Physical Society)

Hall Effect (IQHE) because it occurs at integer filling factors v and displays the quantization of the Hall resistance $R_{xy} = Rn = V_y//_X = h/(ve^2)$ (sec Fig. 4.26) as a consequence of the quantization of *non-interacting electrons* in a 2D quantum well in a magnetic field //. It. therefore, is a result of the discretization of the energy spectrum due to the 2D confinement of the chargc carriers *plus* Landau and spin quantization in the magnetic field.

A microscopic picture of the IQHE is at present [4.73] characterized by a striped structure along the edges of the quantum well where the stripes of constant clcctron density $/i_s$ arc incompressible ($3^{\wedge}{}_c i,/3/j_x$ -> oo; $n_C h$ - chemical potential) and the stripes of varying n_s are compressible. By this striped structure, which has been demonstrated experimentally [4.74], the formation of the plateaus of the IQHE can be described microscopically [4.73].

The quantum Hall resistance has applications in metrology [4.73] since the value Nil = 25812.807S2 has been taken as a resistance standard. In comparative measurements of several national institutions, deviations of less than $2 \times 10"^9$ from this value have been reported.

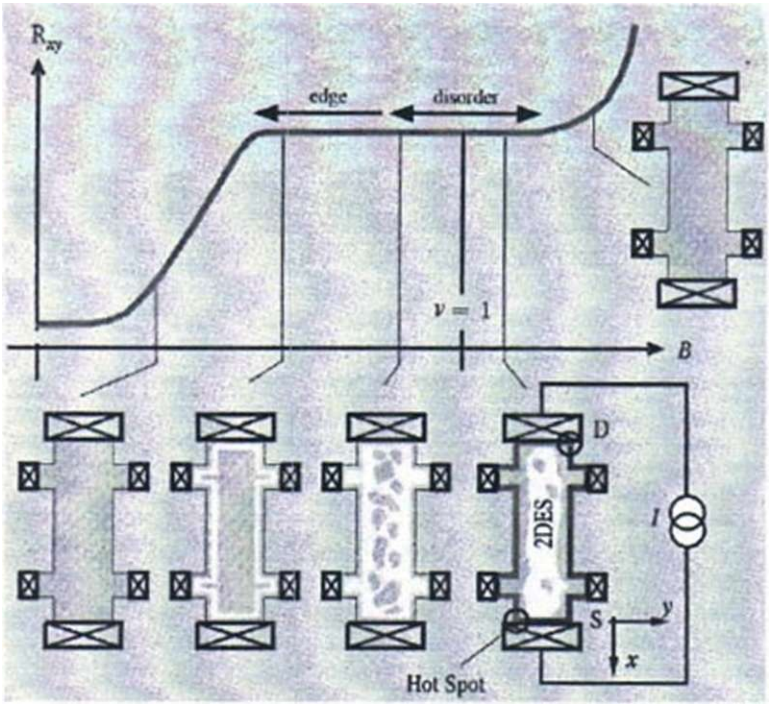

Fig. 4.27 Schematics of the evolution of compressible *(gray)* and incompressible *(while)* stripes or domains in a real inhomogeneous quantum well structure over an integer quantum Ilall cfTcct (IQ11E) plateau in dependence of the magnetic field. (Reprinted with permission from [4.73]. <0 2005 Wiley-VC11)

4.3.4 The Fractional Quantum Hall Effect (FQHE)

In contrast to the IQHE the Fractional Quantum Hall Effect (FQHE). which was discovered by Tsui and Stttrmer (4.75) and theoretically interpreted by Laughlin |4.76] (Nobel prize 1998), occurs at fractional filling factors and its quantum numbers are not integers but rational fractions *p/q.*

The FQHE results from the highly correlated motion of many 2D electrons in a magnetic field. The driving force is the reduction of the Coulomb interaction between the like-charged electrons by a magnetic field. The many-particlc states of this system arc of inherently quantum mechanical nature [4.76]. Fractional quantum numbers and fractionally charged quasi-particles arc the most spectacular of its implications.

At present, the attachment of magnetic vortices to electrons (Fig. 4.28) represents the unifying principle for the description of the multiple many-particle states of the FQHE [4.77] where Laughlin's wave function [4.76] describing the $\nu = 1/3$ states is the prime example for this principle at work. Since electrons are charge accumulations and magnetic flux quanta (vortices) charge deficits they attract each

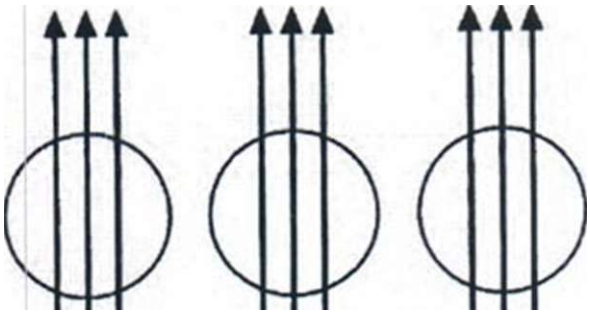

Ffg. 4.28 Skctch of composite particles in Ihc fractional quantum Hall cffcct FQHE for the filling factor w = 1/3. The arrows represent the magnetic flux quanta attached to the electrons *(circles).* (Reprinted with permission from [4.781. O 1999 Karlniher Institut air Technologic)

other. Coulomb energy can be gained by placing vortices onto electrons (composite particle model; sec 14.71) and Fig. 4.28). At v = 1/3 there exist three times as many vortices as there are electrons. The attachment of exactly three vortices to each electron is the origin of the prominent i> = 1/3 FQHE state described by the Laughlin wave function

$$\prod_{i<j} \left(\prod_{k} \right)$$

where the *Zi.j.k* represent the coordinates of *n* electrons in a complex 2D plane. The exponent 3 is a manifestation of the attachment of 3 vortices to the position of each electron and changes to *q* if the electrons are dressed by *q* vortices. Here, only odd *q* values are allowed in order to guarantee the antisymmetry of this electron wave function.

A bound stale of an electron and an even number of flux quanta is itself a fermion and hence called a *composite fermion* (see (4.79)). Numerous properties of these composite fermions and the quantum fluids they form have been established. Their Fermi sea, their Shubnikov-de Haas oscillations, their cyclotron orbits, and their quantized Landau levels have been demonstrated experimentally. The particles' charge, spin, statistics, mass, magnetic moment, and thcrmopower have been measured (sec [4.79]).

4.3.5 2D Electron Gases (2DEG) at Oxide Interfaces

Advances in the heterocpitaxy of complex oxides [4.80] provide the possibility of fabricating interfaces in oxides with atomic precision, including oxides with strongly correlated electrons. 2D electron gases (2DEG) can be formed at these interfaces [4.81]. The electrons interact and order at the interfaces in unique ways (see (4.81-4.83]) so that, for example, novel types of quantum Hall systcms [4.84], unique superconductors [4.85], ferromagnetic ground states [4.86],

and ficld-cffeci transistor behavior [4.87] can be observed. It turns out that everything depends on the precise crystalline structure of the interface (see [4.81]): only when the right atomic layers meet, the internal clcctric fields on each side push electrons toward the junction so that they can form the electron gas with a thickness < 4 nm [4.88]. The quality of oxide films on silicon has been improving steadily [4.89] so that the integration of oxide hcterostructures into silicon wafers could be possible.

Quantum Hall effect. In a (MgZn)()/ZnO hetcrostructure the 2DEG accumulates at the interface through a discontinuity in the electric polarization (sec Fig. 4.29a).

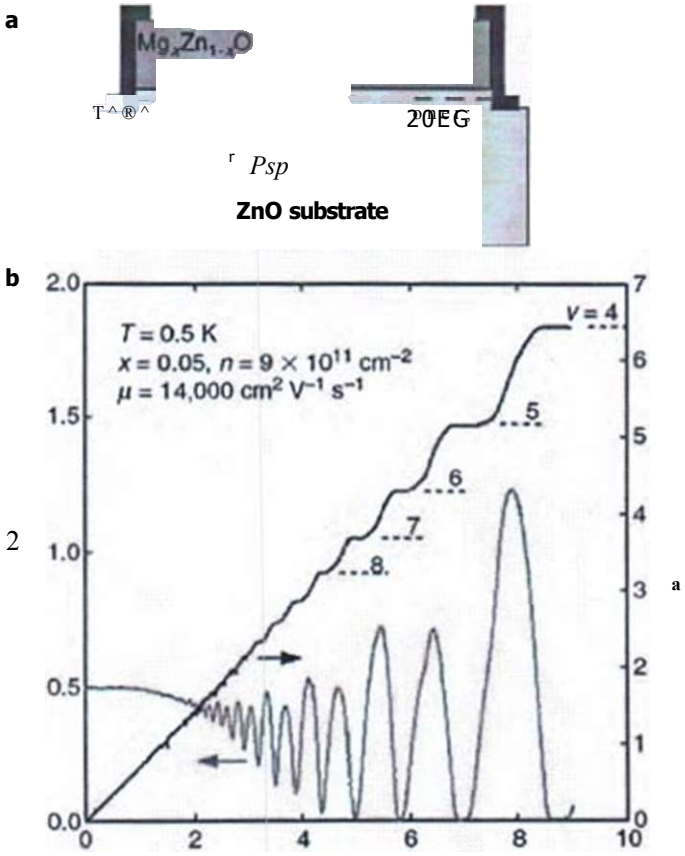

Fig. 4.29 (a) Schematic of (MgZn)OZZnO hcterostructures in which a discontinuity in polarization (P) induces a 2D electron gas (2DKG). P_{SP} is the spontaneous polarization and Ppp. is the piezoelectric polarization, **(b)** Magnetotransport properties of the 2DEG show Shubnikov-dc Haas oscillations *{p_{xx})* and the quantum Hall effect *(p^).* The integers v indicate Landau tilling factors. (Reprinted with permission from [4.82]. © 2008 Materials Research Socicty)

ZnO is a piezoelectric material with a finite spontaneous polarization, *Psp*- When a (MgZn)O layer is grown on the ZnO substrate pseudomorphously. piezoelectric polarization, **Ppf**.. appears as a result of epitaxial strain in addition to *Psp*• At the interface, the sums of P$p and Ppz for the two layers do not necessarily match and a sheet charge is formed in the layer of the narrower band gap material (ZnO) at the interface to relax the electrostatically unfavorable situation. By forming a degenerate 2DEG in the nominally undoped and clean interface channel, a clear oscillation is observed in the magnctorcsistancc and plateaus in the Hall resistance (quantum Hall effect; Fig. 4.29b). These effects result from the quantum interference of free electrons in a strong magnetic field (Lorentz force) and have been observed only in a clean channel with a Hall mobility pu > 10,000 $cm^2/(V\ s)$ (4.82,4.84).

Superconductivity. In LaAIOj/SiTiOa samples, a superconducting condensate has been found to be in the ground state [4.85] with critical temperatures of ~200mK (Fig. 4.30). Critical field measurements with the magnetic field aligned parallel and perpendicular to the interface plane reveal a large anisotropy with the in-plane coherence length estimated to ~ 50-100 nm and the thickness of the superconducting sheet to only ~ 4 nm. From these data, the interface is expected to behave as a 2D superconductor such as described by the Berezinskii-Kosterlitz-Thouless theory 14.90, 4.91]. In field-effect transistor configurations, perpendicular electric fields allow the sheet carrier density of LaAl()3/SrTi03 interfaces to be substantially modulated in both the normal and the superconducting states (see [4.811). At low temperatures an insulator-to-superconductor phase transition can be induced with electric fields [4.92]. This might suggest to write complex patterns into such a 2DEG, potentially allowing the definition of entire electronic circuits (see 14.83]).

4.3.6 Multilayer EUVand X-Ray Mirrors with High Reflectivity

In extreme ultraviolet (EUV) lithography for future chip production (see Sect. 9.2) or in research at high-power soft x-ray sources, such as free electron lasers (FLASH, XFEL), high-reflectivity mirrors are required as optical components for beam formation [4.941. As well known from visible optics, /./4 multilayer structures enhance the reflectivity by constructive interference of the light waves reflected at the layer interfaces (Fig. 4.31). The multilayer stack consists of alternating layers of absorber and spacer materials with different refractive indices. The absorber material is selected according to a high reflectivity at the boundary with the spacer while still having an extinction coeflicient as low as possible, whereas the spacer material should have the lowest extinction coefficient at the desired wavelength.

The multilayers can be fabricated by DC sputtering [4.95]. For the fabrication of multilayers with a period of 1.0-5.0 nm for radiation wavelengths of 2-10 nm, the layer density, smoothness, and the ability to produce continuous thin layers with abrupt and smooth interfaces arc pivotal.

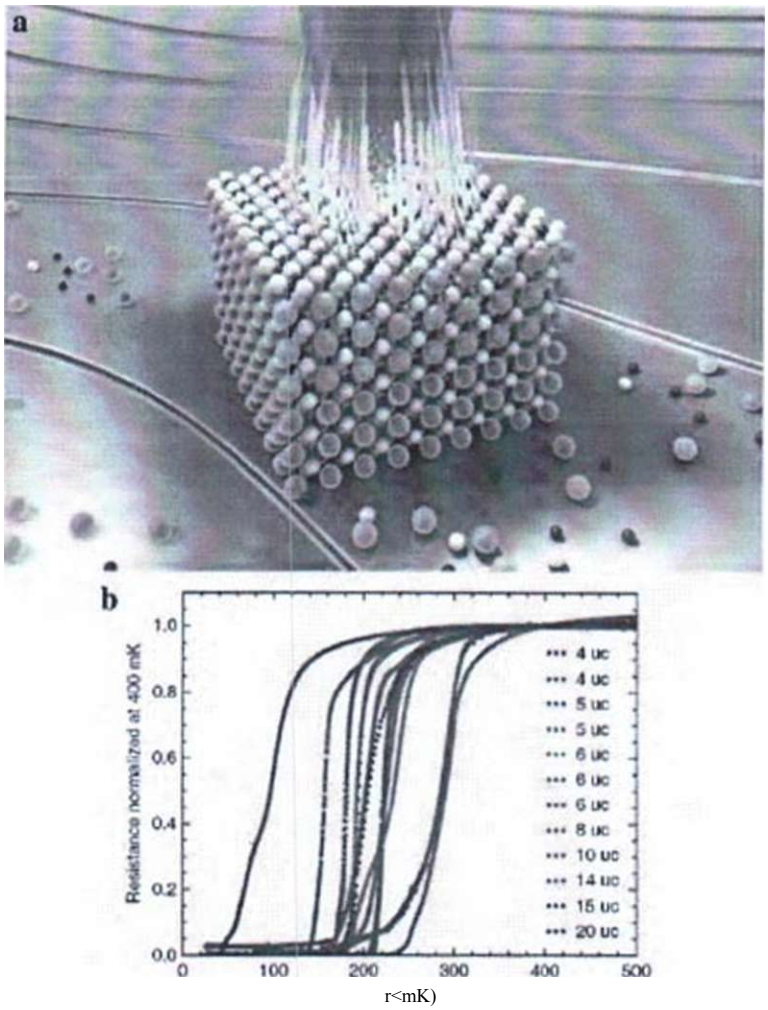

Fig. **4.30** **(a)** The artist's impression shows the interface between lanthanum aluminate (l-aA10$_3$; *top)* and strontium titanatc (SrTiO^; *bottom).* The atoms are shown in different colors: La *{orange).* A1 *(red).* Sr *(pale blue).* Ti (*dark blue).* O *(white)* (4.93]. (b) Resistance measurements of several LaAIOj/SrTiOj oxide hctcrostructurcs with a variety of LaAlO^ thicknesses measured in unit cells (uc). The resistances are normalized to the values measured at 400 mK. The figure shows samples with superconducting transitions at ~ 200 mK (4.81]. (Reprinted with permission from (4.93] **(a)** and (4.81] (b). © 2009 Nature Publishing Group **(a)** and © 2008 Materials Research Socicty (b))

Mirrors with the spectral range from 40 to 120 nm are of particular interest for astrophysical applications making use of A1 layers with protecting MgF2 or LiF layers (see Tabic 4.1). For the wavelength range 35-50 nm Sc/Si multilayers appear to be favorable. For wavelengths from 12.5 nm (above the Si

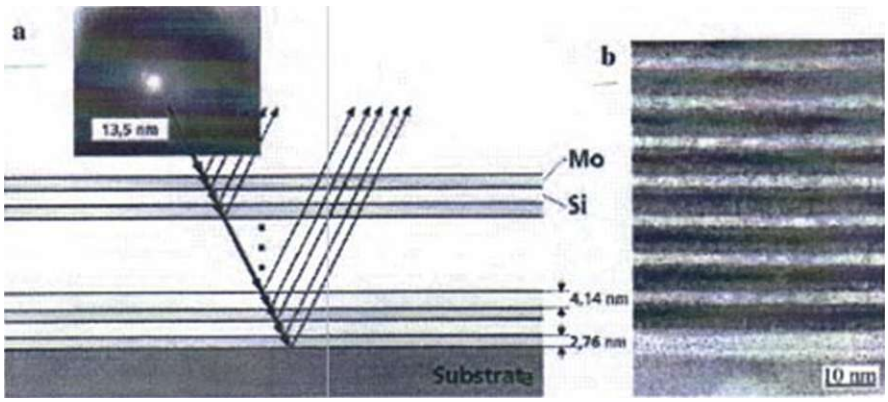

Fig. 4.31 **(a)** Schcmatic representation of high-reflectivity multilayer extreme ultraviolet (CUV) and soft x-ray mirrors due to constructive interference of the radiation reflcctcd at the multilayer interfaces with the **13.5** nm EUV radiation as an example, **(b)** Transmission electron micrograph of a Mo/Si multilayer for EUV mirrors. (Reprinted with permission from [4.94J. <D 2008 Photonik; S. Yulin)

Tabic 4.1 UV. EUV. and x-ray mirrors and multilayer mirrors (4.94]

Multilayer system	A range (nm)	k (nm)	Number of layer periods (AO	Reflectivity (%)	FWIIM
Al	70-150	110	_	60	_
Sc/Si	40-50	46	20	52	4.6
Mo/Si	12.4-40	26	25	25.8	2.6
Mo/Si	13.5 (EUV)	13.5	60	69.5	0.5
M0/B4C	6.4-11.0	6.7	200	26.0	0.04
Cr/Sc	3.1-4.4	4.4	300	7.1	0.021
		3.1	400	17.1	0.008
Cr/V	2.4-2.7	2.5	400	5.2	0.005

L-absorption edge) to 40 nm, Mo/Si multilayer mirrors are used. For the 13.5 nm EUV radiation, maximum reflectivity (see Table 4.1) has been achieved by minimizing intcrdiffusion making use of barrier layers [4.94]. From the wavelength regime from 6 to 12 nm, which is of interest for studies with soft x-rays at free electron lasers, **Mo/B4C** multilayer mirrors arc used, whereas for the so-called water window between the K absorption edges of oxygen (A. = 2.3 nm, 543 eV) and carbon (4.4 nm, 284 eV), which is of particular interest for x-ray microscopy, multilayers of Cr/Sc, Cr/Ti, and Cr/V are employed (Table 4.1, Fig. 4.32).

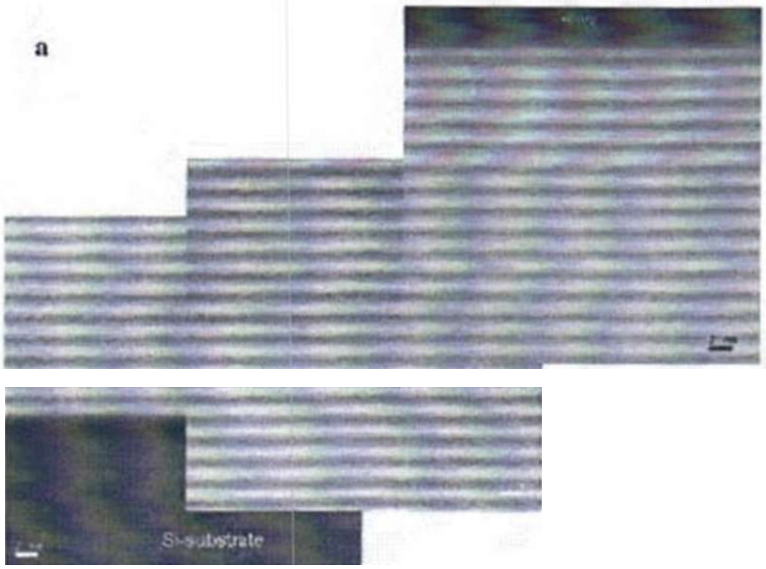

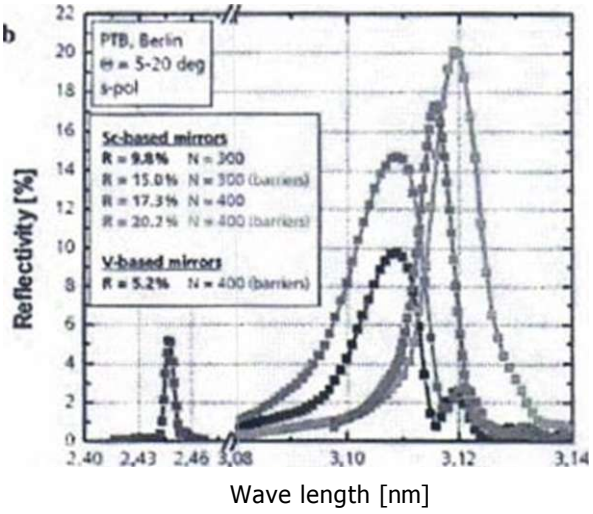

Fig. 4.32 (a) Transmission electron micrograph of the layer structure of a diffusion-barricr-optimized Cr/Sc multilayer (jV = 300) mirror for soft x-ray reflection; near the substrate *(bottom).* in the stack center and near the surface *(top):* scale bar: 2 nm. (b) Enhancement of the reflectivity of Cr/Sc and Cr/V multilayers by optimization of the diffusion banners. (Reprinted with permission from [4.941. © 2008 Photonik: S. Yulin)

4.4 Summary

Nanocrystals or nanocrystal ensembles may give rise to colors due to quantum confinement, plasmonic excitation, or photonic-crystal effects for use in biomedical detection or sensors. Metallic nanowires exhibit enhanced mechanical properties and can he used for the construction of negative-index materials (metamaterials), whereas semiconductor nanowires offer potentials for transistors, logic gates, multicolor light-emitting diodes (LEDs), and photodetectors. In the conductance through individual rows of atoms or single-atom contacts, the valency of the particular metal is manifested. Semiconductor nanolaycrs (quantum wells. 2D electron gases - 2DEG) in a magnetic field show the integral quantum Hall effect of non-interacting electrons with application in metrology or - at higher fields - the fractional quantum Hall effect of electrons interacting via magnetic vortices. 2DEGs can also be generated at oxide interfaces demonstrating quantum Hall cffcct, superconductivity, and ferromagnetic features. Nanostructural multilayers are used as high-reflectivity mirrors for extreme ultraviolet (EUV) and x-ray radiation.

References

4.1 D. Bimberg. Phys. J. 5(8/9). 43 (2006)
4.2 G.D. Scholcs, G. Rumbles. Nature Materials 5.683 (2006)
4.3 U. Banin. Nat. Mater. 6. 625 (2007)
4.4 S.E. Ilabas ct al.. Nat. Mater. 6.692 (2007)
4.5 E.H. Sargent. Adv. Mater. 17.515 (2005)
4.6 M.A. Mines. G.D. Scholcs. Adv. Mater. 15.1844 (2003)
4.7 J.Y. Ouyang et al.. J. Phys. Chcm. C 112.13805 (2008)
4.8 M.M. Mayc ct al.. Nat. Mater. 8. 388 (2009)
4.9 G. Rollmann ct al.. Phys. Rev. Lett. 99,083402 (2007)
4.10 W.J. Huang ct al.. Nat. Mater 7. 308 (2008)
4.11 II. Portales ct al.. Proc. Natl. Acad. Sci. USA 105.14784 (2008)
4.12 N. Shibatact al., Phys. Rev. Lett. 102. 136105 (2009)
4.13 Y. Tang. M. Ouyang. Nat. Mater. 6. 754 (2007)
4.14 J. Wood, Materials today 11. May 2008. p. 8
4.15 Q.F. Gu ct al.. Phys. Rev. Lett. 100. 045502 (2008)
4.16 D. Sticrct al.. Phys. Rev. B59. 5688 (1999)
4.17 I.L. Mcdintz et al., Nat. Materials 4.435 (2005)
4.18 N.R. Rosi. C.A. Mirkin.Chcm. Rev. 105. 1547(2005)
4.19 M. Bottini, T. Mustclin, Nat. Nanotcch. 2. 599 (2007)
4.20 II. Liu ct al.. Angcw. Chcm. Int. Edn. 46. 6473 (2007)
4.21 J.P. Gc et al.. Angcw. Chcm. Int. Edn. 46. 7428 (2007)
4.22 M. Bniche/ ct al.. Science 281. 2013 (1998)
4.23 W.C.W. Chan. S.M. Nie. Science 281.216 (1998)
4.24 P. Alivisatos. Nat. Biotcchnol. 22.47 (2004)
4.25 Y.G. Sun. Y.N. Xia, Science 298. 2176 (2002)
4.26 R.C. Jin ct al.. Nature 425.487 (2003)
4.27 U. Krcibig. M. Vollmcr. *Optical Properties of Metal Clusters* (Springer. Berlin. 1995)
4.28 R. Elghanian ct al. Science 277. 1078 (1997)
4.29 E. Yablonovitch. Sci. Am. 285.47 (2001)
4.30 F.H.L. Koppcns ct al.. Nature 442. 766 (2006)

4.31 D.P. DiVinccnzo. Scicncc 270. 255 (1995)
4.32 D. Press ct aL. Nature 456. 218 (2008)
4.33 C.W. Kim ct al.. Adv. Mater. 20. 1859 (2008)
4.34 L. Li et al. J. Mater. Sci. Tcchnol. 23.166 (2007)
4.35 E.H. Yuc ct al.. J. Mater. Sci. Tcchnol. 24. 850 (2008)
4.36 l3. Derby. 7th Brazilian - MRS Meeting (Sao Paulo. 2008)
4.37 G. Dolling ct al.. Optics Lett. 32.53 (2007)
4.38 N. Liu ct al.. Nat. Mater. 7. 31 (2008)
4.39 U.K. Chcttiar ct al.. MRS Bull. 33. 921 (2008)
4.40 J. Valentine ct al.. Nature 455. 376 (2008)
4.41 AJ. Hoffmann. Nat. Mater. 6.946 (2007)
4.42 W.J. Park. J.S. Kim. MRS Bull. 33. 907 (2008)
4.43 Ch. Caloz, Materials Today. 12. March 2009. p. 12
4.44 G.V. Elcfthcriades. Materials Today 12. March 2009. p. 30
4.45 C.M. Soukoulis ct al.. J. Phys.: Condens. Matt. 20. 304217 (2008)
4.46 J.B. Pcndry ct al.. IEEE Trans. Microw. Theory Tech. 47. 2075 (1999)
4.47 G. Shvets. Nat. Mater. 7.7 (2008)
4.48 S. Linden. M. Wegener. Physik Journal 5 (12). 29 (2006)
4.49 U. Engclhardt. T. 1>c. Scicncc 323. 110 (2009)
4.50 S. Schwaiger et al.. Phys. Rev. Lett. 102. 163903 (2009)
4.51 Y. Li ct al.. Materials today 9. Nr. 10. 18 (2006)
4.52 B.M. Wen ct al.. Phys. Rev. Ixtt. 101. 175502 (2008)
4.53 G.F. Zheng ct al.. Adv. Mater. 16. 1890 (2004)
4.54 Y. Huang ct al.. Scicncc 294. 1313 (2001)
4.55 F. Patolsky ct al.. Proc. Natl. Acad. Sci. (USA. 101. 14017 (2004)
4.56 G. Zheng ct al.. Nat. Biotcchnol. 23.12W (2005)
4.57 X.F. Duan ct al.. Nature 421. 241 (2003)
4.58 O. Ilayden ct al.. Nat. Mater. 5. 352 (2006)
4.59 P.J. Pauzauskic. P.D. Yang. Materials Today 9. Nr. 10.36 (2006)
4.60 A. Walther ct al.. Nanol>ctt. 9. 2026 (2009)
4.61 N. TUccitto ct al.. Nat. Mater. 8. 41 (2009)
4.62 Y. Wakayama ct al.. Nano Lett. 8. 3273 (2008)
4.63 C. Thclandcr ct al.. Materials Today 9. Nr. 10. 28 (2006)
4.64 H. Ohnishi ct al.. Nature 395. 780 (1998)
4.65 A.I. Yanson ct al.. Nature 395. 783 (1998)
4.66 E. Schccr ct al.. Nature 394. 154 (1998)
4.67 A. Yazdani ct al.. Scicncc 272.1927 (1996)
4.68 J.C. Cucvas ct al.. Phys. Rev. Lett. 80. 1066 (1998)
4.69 R. I.andaucr. Phil. Mag. 21. 863 (1970)
4.70 A. Shik. Quantum Wells - *Physics ami Electronics of Two-Dimensional Systems.* (World Scientific. Singapore. 1997)
4.71 H.L. Stormer ct al.. Rev. Mod. Phys. 71(2). S298 (1999)
4.72 K. v. Klitzing et al.. Phys. Rev. Leu. 45.494 (1980)
4.73 K. v. Klitzing et al.. Phys. J. 4(6), 37 (2005)
4.74 Y.Y. Wei ct al.. Phys. Rev. Lett. 81.1674 (1998)
4.75 D.C. Tsui ct al.. Phys. Rev. Lett. 48. 1559 (1982)
4.76 R.B. Laughlin, Phys. Rev. Lett. 50. 1395 (1983)
4.77 S. Das Sarma. A. Pinczuk. Eds., *Perspectives of Quantum Hall Effects.* Wiley. New York (1997)
4.78 A.D. Mirlin. P. Wolflc. Nachrichlen Forschungszcntnim Karlstuh. 31. 94 (1999)
4.79 J.K. Jain. Physics Today. April 2000. p. 39
4.80 A. Ohtomo. II.Y. Hwang. Nature 427.423 (2004)
4.81 J. Mannhart ct al.. MRS Bull. 33.1027 (2008)

Chapter 6
Nanocrystalline Materials

The design of nanocrystalline solids with novel properties different from the chemically identical coarse-grained counterparts was an early and most fruitful contribution to nanoscience [6.1, 6.21. Nanocrystalline materials arc polycrystals with a crystallite size usually in the 10-nm range and atomically disordered crystallite interfaces with a substantial volume fraction. The macroscopic properties arc, therefore. dominated by the small crystallite size, giving rise to confinement effects, and the interfacial structure. Crystallites and interfaces may be of the same or of different chemical composition, composites of different materials may be fabricated, dimensionality may play a role, and a plethora of synthesis routes is available (see Chap. 3). The wide field is covered by early reviews [6.3-6.61, monographs [6.7, 6.8), and an encyclopedia (see [6.9)). In this chapter, recent developments in the lield of nanocrystalline solids will be reviewed, including aspects such as atomic simulation, structure of interfaces, plasticity, strength, superplasticity, fatigue, composites, ceramics, diffusion, and surface-induced manipulation of the properties of nanomaterials.

6.1 Molecular Dynamics Simulation of the Structure of Grain Boundaries and of the Plastic Deformation of Nanocrystalline Materials

Among the various atomic-level simulation approaches, molecular dynamics (MD) has proven particularly useful for studying nanocrystalline solids [6.10-6.13). In deformation studies by MD, rather large plastic strains can be considered, enabling the deformation under very high grain boundary and dislocation densities. However, in addition to being limited to relatively small model systems consisting of typically millions of atoms, the fundamental limitations inherent to the MD approach are well known, pertaining mainly to the reliability of the interatomic potentials used and the relatively short lime period (of typically 10 ns) over which the dynamics of the system can be probed. This leads to extremely high strain rates exceeding $10^7\ s^{-1}$, much higher than in experiments, requiring rather high stresses. While the empirical interatomic forces used in most MD simulations arc computationally highly

H.-E. Schaefer. *Nanoscience,* DOI 10.1007/978-3-642-10559-3_6.

efficient, they are unable to fully capture the many body nature of electronic bonding. Interestingly, however, a comparison between many body and pair potentials used in simulations of grain boundaries (see [6.11)) revealed only few qualitative differences, suggesting that many body effects may not dominate, e.g., the grain boundary (GB) behavior. The dynamic properties of defects (e.g., dislocations, grain boundaries, and precipitates) which dictate the mechanical properties of materials should be computed directly using quantum mechanics-based total-energy methods. However, the number of atoms necessary to do so exceeds available computational resources and will for years to come (sec [6.14]). The challenge, therefore, is to identify the real physical processes (see [6.11]), so that the information extracted from simulations focuses on a careful classification of the atomic processes occurring. e.g., during plastic deformation (see |6.12|), taking into account the interplay between GB structure and deformation mechanisms, as discussed in the following sections.

6.2 Grain Boundary Structure

Coarse-grained polycrystals contain GBs with very much differing structures and with a wide spectrum of energies and properties (see [6.11, 6.15]). *Special high-angle GBs* contain no dislocations and their properties arc perfect-crystal like (Fig. 6.1a) with low energies, low atomic diffusivitics, and low mobilities but with high sliding resistance and cohesion. Grain boundaries of this type, i.e., twin boundaries, play a role in the process of deformation twinning (see [6.11]). In *low-angle or dislocation boundaries* the atomic structure consists of periodic arrays of dislocations and their properties are characterized by isolated lattice dislocations and their interactions. In the *general high-angle GB,* dislocation cores are completely overlapping yielding a GB structural atomic disorder similar to an amorphous material, which is characterized by the local radial distribution function. #(/•) (Fig. 6.1b).

According to MD simulations [6.111, the structure of GBs in nanocrystallinc Pd (Fig. 6.1c) is fully disordered and virtually identical to that of high-angle (110) twist boundaries (Fig. 6.1b), i.e., to the universal structure of the high-energy GBs in coarse-grained Pd. These simulations for nanocrystallinc Si and Pd |6.11] show that the randomly oriented grains are connected by a glassy intergranular "phase". These observations arc consistent with simulations of the phonon density of states and of the related free energy [6.16] which indicate that below a critical grain size (1.5-3 nm) nanocrystallinc microstructurcs are thermodynamically unstable with respect to the amorphous phase.

Temperature-dependent structural and dynamical transitions in thermal equilibrium arc additionally predicted by MD simulations in highly disordered high-energy GBs in Si and Pd bicrystals (see 16.11]) at a critical temperature T_c below the melting temperature T_m (Fig. 6.Id). At $T>T_C$ the splitting of the second *g(r)* peak observed at low temperatures (Fig. 6.1c) has disappeared. This transition has a profound influence on the high-temperature GB properties, such as GB migration.

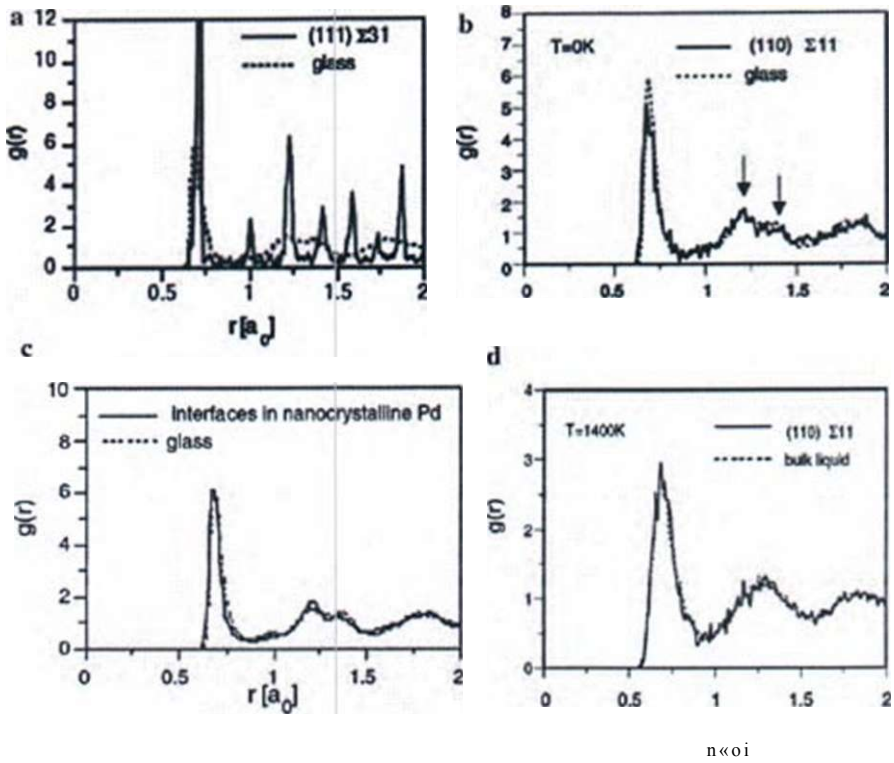

n«oi

Fig- 6.1 I.ocal radial distribution functions. #(/•). determined from MD simulations for high-angle twist GBs on densest lattice planes of fee Pd. described by an embedded atom model (F.AM) potential. The radial distribution function. *g(r),* is normalized such that for large r. £(r) = 1. For comparison, the *dotted lines* show *g(r)* for bulk Pd glass or bulk liquid Pd. (a) Bicrystal (111) E31 twist boundary (E is the inverse density of coincidencc-sitc lattice sites) with an energy of 300 rnJ/m^2; (b) (110) El 1 twist boundary at 7=0 K with an energy of 1025 mJ/m^2. The *arrows* indicate the split second peak present in both the GB and the bulk glass, (c) Local radial distribution function for the GB atoms in a Pd nanocrystalline solid with a grain size of 8 nm. compared to the g(r) of bulk Pd glass, **(d)** High-temperature radial distribution function for the atoms in the two ccntral planes of the (110) E11 twist GB in Pd at 7=1400 K compared to that of the bulk melt supercooled to the same temperature (Reprinted with permission from [6.11). <D 2005 Elsevier)

sliding, and diffusion and hence on the mechanical behavior of nanocrystalline solids. The temperature-dependent changes of the GB mobility and GB diffusivity (Fig. 6.2) are ascribed to a transition from a low-temperature solid-like atom hopping to a high-temperature liquid-like reshuffling of the GB atoms (see [6.11)). This is consistent with an early suggestion by Mott [6.17] that the mechanism for GB migration involves local disordering, or "melting," of small groups of atoms at the boundary, thereby enabling atoms belonging to one grain to reshuffle collectively while aligning themselves to the opposite grain. According to this idea, the activation energy for GB migration at high temperatures can be substantially smaller than the activation energy for atomic diffusivity in GBs (sec [6.11]).

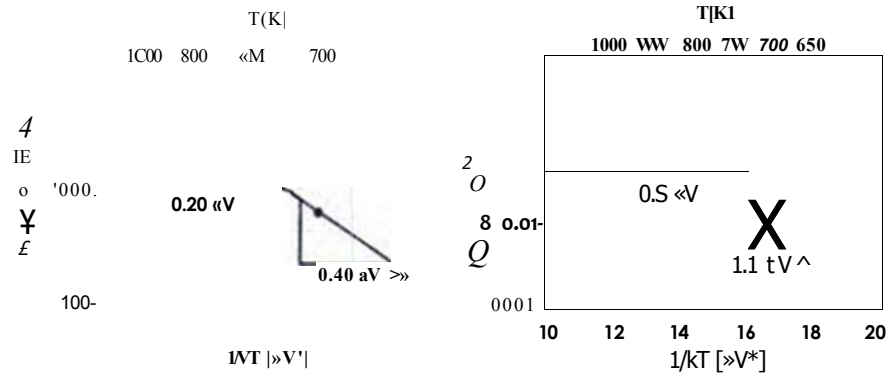

Fig. 6.2 Arrhenius plots derived from MD simulations, making use of a Lennard-Jones potential, for **(a)** the GB mobility, m. and **(b)** the GB diffusivity. W_C\\\. for the (001) E29 twist GB in Cu. (Reprinted with permission from [6.11]. © 2005 Elsevier)

Experimental evidence of the structure of grain boundaries may be derived from x-ray diffraction (XRD). high-resolution transmission electron microscopy (HRTEM), extended x-ray absorption line-structure (EXAFS). positron annihilation (PA), or atomic diffusion (AD). From XRD of n-Pd [6.18], the atomic coordination numbers in the GBs were determined to depend on the time-temperature history of the sample, indicating that the structure of well-relaxed GBs is similar to the structure of microstructurally unconlined bicrystalline GBs. For the direct test whether the atomic structure of GBs changes revcrsibly with temperature, temperature-dependent XRD on line-grained nanostructured specimens arc required. Initial XRD studies on nanocrystalline Fe73SiioB7Nb3Cui (grain size 12 nm) at ambient temperature and at 7=773 K showed a reversible change of the GB radial distribution function at nearest-neighbor sites (Fig. 6.3a).

For the *lateral* resolution of atom columns in general high-angle GBs by HRTEM. 0.1-nm resolution of the microscope is required (see Fig. 6.4). One should, however, have in mind that sample preparation and high-energy electron irradiation in HRTEM may affect the GB structure. For characterization of grain boundaries *along* the columns, the application of electron microscopes with aberration correction may be promising |6.22). From EXAFS studies a reduction of the atomic coordination in the GBs has been reported which appears to depend on the time-temperature history of the specimen [6.18, 6.23,6.24].

By positron-electron annihilation techniques, atomic free volumes in GBs can be studied specifically [6.25]. In defect-free crystals, positrons exhibit diffusion lengths of ~ 100 nm prior to annihilation with electrons. In nanocrystalline solids they arc, however, efficiently trapped by atomic size free volumes, which can be characterized by the annihilation signals. In nanocrystalline Pd, agglomerates of a few vacancies were detected by positron lifetime studies [6.20] with positron trapping rates varying revcrsibly with temperature (Fig. 6.3b). This variation may be ascribed to a temperature-dependent structural change of the agglomerates in the GBs. In C3B

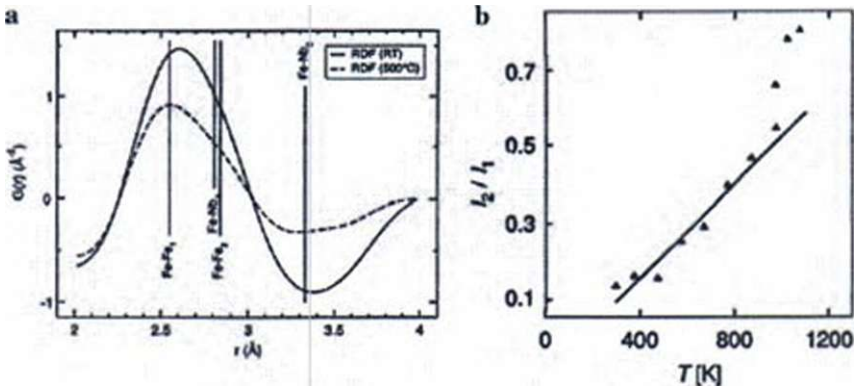

Fig. 6.3 **(a)** Nearest neighbor part of the radial distribution function G(r) of atoms in the GBs of nanocrystallinc I'C73Sii6B7NbjCui measured rcvcrsibly by x-ray diffraction at ambient temperature (RT) and at 737 K [6.19] with the bulk nearest-neighbor distance of iron atoms (Fo-Fc() or iron and niobium atoms (Fc-Nbi) or the next-nearest neighbor distances (Fc-Fc2, Fe-Nb2> indicated, (b) Reversible temperature variation of the positron trapping at vacancy-size free volumes with the concentration Ci and at vacancy agglomerates (C2) in the grain boundaries of nanocrystallinc I'd(«/-ri6 with a grain size of rf<250 nm. The changc of the intensity ratio /2//1 = oiCi/o\C\ of the two positron lifetimes rj = 175 ps and xi = 370 ps. characteristic for the two types of intcrfacial free volumes, indicates a reversible changc of the intcrfacial free volumes with temperature. a 1 and <72 arc the specific positron trapping rates of vacancy-size free volumes and of vacancy agglomerates, respectively (6.20]. (Reprinted with permission from |6.19) **(a)** and [6.20| (b). © 2005 l-andcsstiftung Baden-WUrttcmbcrg **(a)** and © American Physical Socicty (b))

diffusion experiments, a change of the temperature dependence of the atomic diffusivity at high temperatures (6.26) is consistent with the MD simulation study of the diffusion behavior shown in Fig. 6.2b. A reversible transition from an amorphous to a liquid structure of interfaces in n-Si has been deduced from molccular dynamics simulations (6.27).

6.3 Plasticity and Hall-Petch Behavior of Nanocrystalline Materials

Low-temperature plastic deformation of coarse-grained metals involves the nucleation of dislocations from a Frank-Read source and their glide through the crystal on well-defined slip systems. In a polycrystallinc material, the size L of the sources is restricted to the grain size. Since the stress $a=Gb/L$ needed for their operation (G - shear modulus, b - Burgers vector) rapidly increases with decreasing L, this deformation mechanism can operate only down to a grain size of typically 1 |im. For the plastic deformation of nanocrystalline metals with smaller grain sizes (Fig. 6.5), mobile dislocations must be nucleated from other sources, such as grain boundaries or grain junctions. Recent MD simulations (see [6.11, 6.12]) suggest the existence

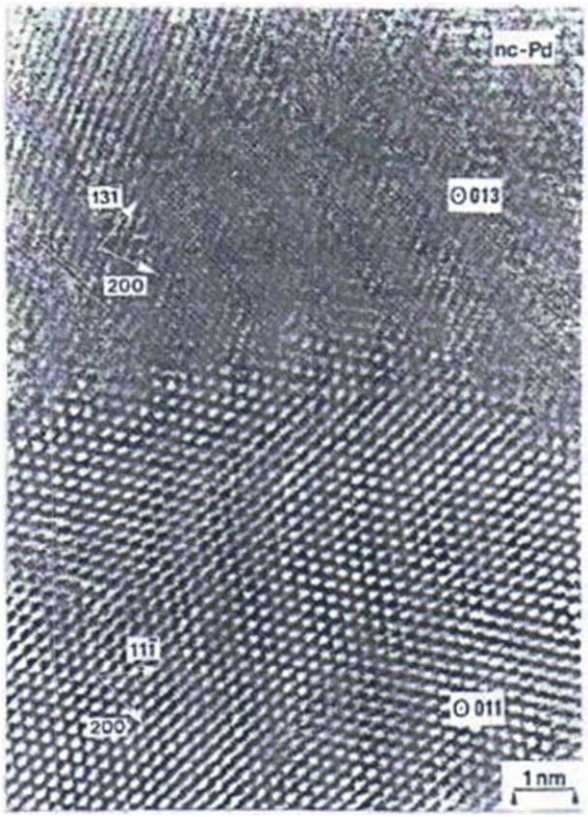

Fig. 6.4 Atomic resolution transmission electron micrograph of nanocrystalline Pd with <013> and <011> zone axes and an orientation correlationship £>39 of the two crystallites, giving rise to a general, high-energy grain boundary in the center of the micrograph. (Reprinted with permission from [6.21]. <D 2000 Elsevier)

of a length-scale competition between the grain size d and the dislocation splitting distance r which renders, with decreasing d, the dislocation process less and less effective until, at a critical grain size d_c, grain boundary-based deformation processes dominate. The simulations also show a propensity for deformation twinning, giving rise to strain hardening.

According to the simulations, in the case of the largest nanosized grains the GBs act as sources for complete extended dislocations that subsequently glide across the grains to be finally re-incorporated into the GBs. Although Frank-Read sources cannot be operated, the material still seems to deform by the conventional dislocation-slip mechanism, including dislocation-dislocation reactions and cross slip.

When the grain size decreases well below 100 nm the deformation behavior seems to change fundamentally because of the appearance of deformation twinning in the simulations in A1 with a high stacking fault energy (Fig. 6.6a). Twin deformation occurs through emission of groups of partial dislocations from grain boundaries into grain interiors (see [6.29, 6.30]). Deformation twinning in nanomaterials has been observed [6.31], [6.32] by high-resolution electron microscopy (Fig. 6.6b). Although it is unknown whether the increase in yield stress follows the $\sigma^* \sim d^{-1/2}$ Hall-Petch relation, two hardening mechanisms are envisaged.

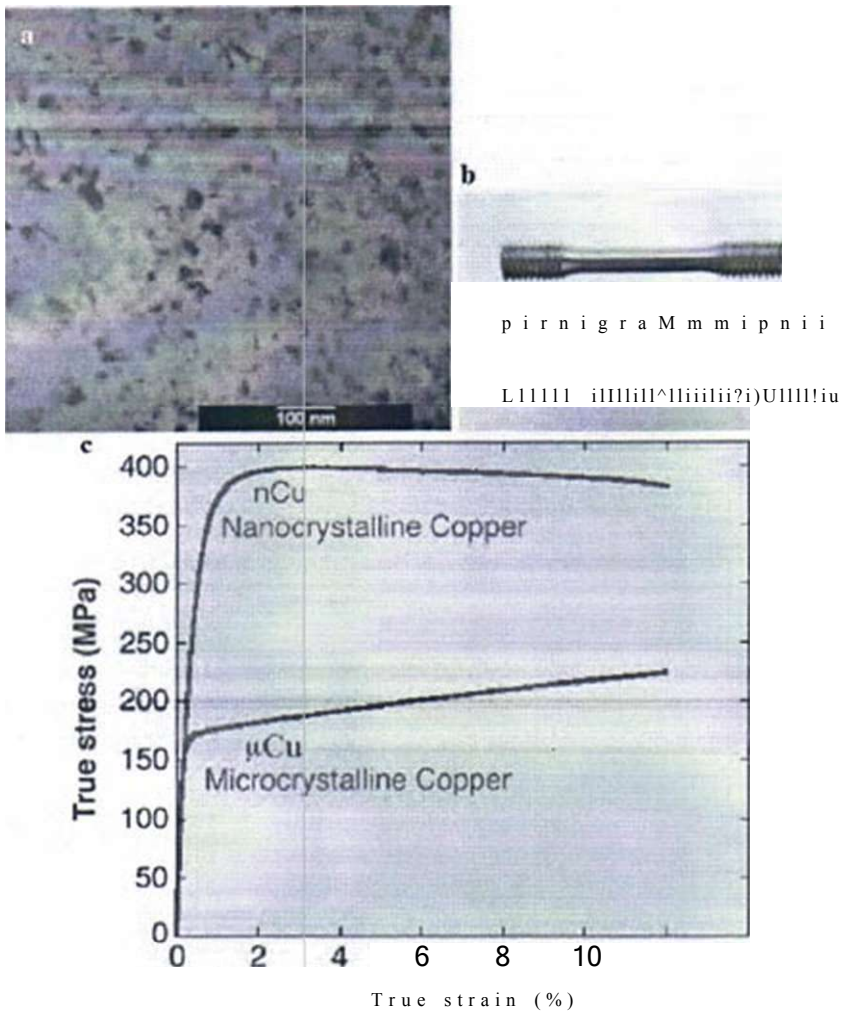

Fig. 6.5 **(a)** Transmission electron micrograph of a nanocrystalline Cu sample (grain size. 20 nm) synthesized by inert gas condensation [6.12]. **(b)** Tensile test specimen cut from nanocrystallinc Cu. prepared by powder metallurgy [6.28]. (c) Comparison of the stress-strain curvcs of nanocrystalline and microcrystall inc Cu. showing a higher yield strength in n-Cu; the tests were performed at a strain rate of $s = 5 \times 10^{-6}s^{-1}$ |6.28J. (Reprinted with permission from [6.121 (a) and [6.26] **(b)** (c). © 2006 Elsevier **(a)** and © 2003 **AAAS (b)** (c))

including dislocation pilc-ups against GBs and pilc-ups against complex networks of deformation twins (see [6.11)).

As the grain size is even smaller and similar to the si/.e of extended dislocations, slip of complete dislocations seems to be gradually replaced by the slip of partial dislocations in the MD simulations, which is also indicated in experiments [6.32].

The transition from complete- to partial-dislocation slip in simulations with decreasing grain size is accompanied by a rapid increase in the stress required to

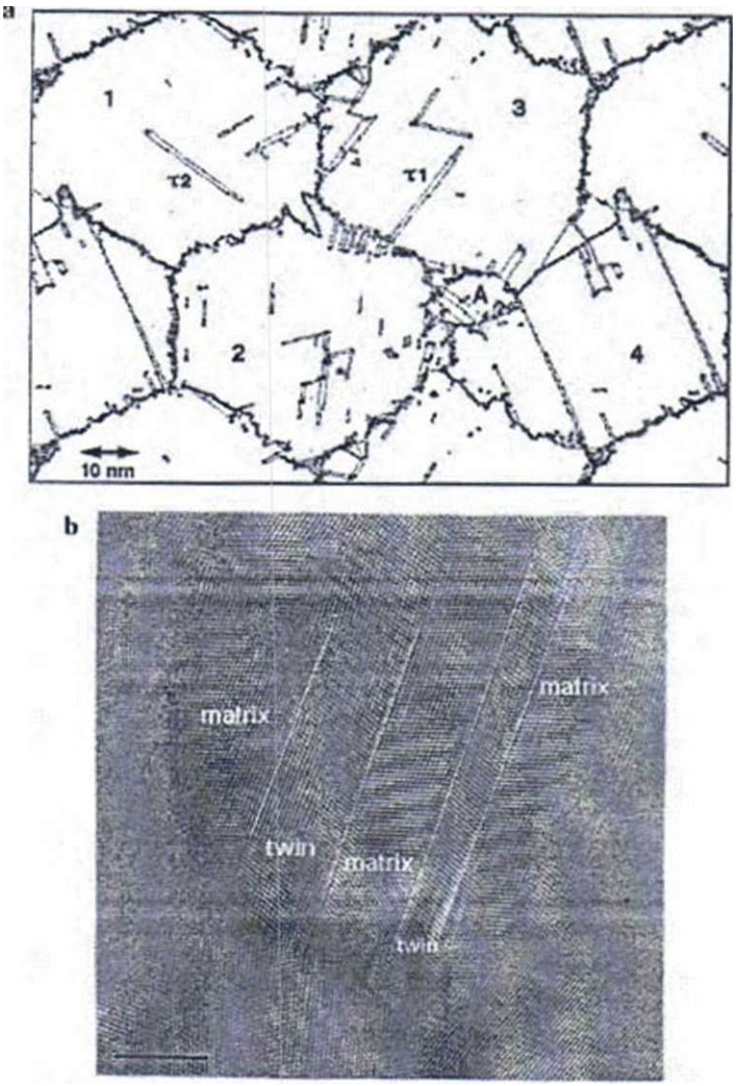

Fig. 6.6 (a) MD simulation of plastic deformation (strain e = 0.119) of nanocrystalline Al. Formations r = 1 and r = 2 in grains 3 and 1 mark two types of deformation twins. The formation of a new grain, labeled A. is also seen (see Video 3 in |6.11|). (b) lligh-resolution transmission electron micrograph of nanocrystalline Pd deformed to e = 0.32 by rolling at a strain rate e = 0.3 s^{-1} [6.31]. (Reprinted with permission from [6.11] (a) and [6.31] (b). © 2005 Elsevier (a) and © 2005 Wilcy-VCH (b))

nucleate dislocations from the GBs. The dislocation activity therefore decreases rapidly until a C3B-based deformation process takes over. The simulations reveal that this crossover in the dominating deformation mechanisms from Hall-Petch hardening to softening gives rise to a minimum in the strain rate and a maximum in the yield stress at the "strongest grain size" d_c where a maximum in hardness (Fig. 6.7a) is observed experimentally. Hardness measurements covering the crossover from normal to inverse Hall-Petch behavior have been critically discussed 16.331. According to the simulations 16.10, 6.11], Coble creep (i.e., GB diffusion-induced grain elongation accommodated by Lifshitz sliding) characterized by a strain rate dependence e^crDcii/Td} (see [6.11]) seems to dominate the deformation mechanism at small grain size $d<d_c$, giving rise to a softening at small grain

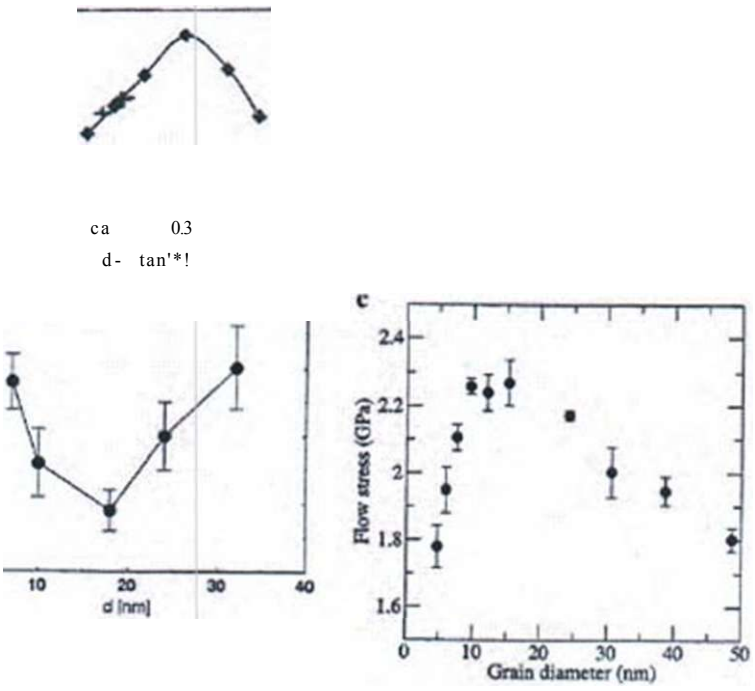

Ki^. 6.7 Experimental data and MD simulation results of the Hall-Petch relation and the crossover to inverse I lall-Pctch behavior in dependence of grain sized in ihc plastic deformation of nanocrystalline materials, (a) Hall-Petch plot (yield strength versus $d^{-1/2}$) for Cu. The yield strengths are obtained from tension, compression, and hardness tests on nanocrystallinc Cu [6.121: (b) MD simulation of the grain-size dependence of the strain rate e of nanocrystallinc Al. The minimum in e at d_c = 18 nm suggests the existence of a "strongest size" at which the grains arc too small to sustain the dislocation-slip proccss. but arc still too large for GB sliding processes to dominate the deformation [6.11 J; (c) flow stress versus d in nanocrystallinc Cu [6.10]. (Reprinted with permission from [6.12] (•). [6.11) (b). and [6.10| (c). © 2006 Elsevier (»). © 2005 Elsevier (b), and © 2003 AAAS (c))

sizes. Here, a is the stress and Don the GB diffusivity. This gives rise to the e minimum or a maximum of the simulation data for the flow stress in Fig. 6.7b and c, respectively. In simulations of Coble creep (see [6.11|) it has been found that the activation energy for crccp is similar to the diffusion activation energy in high-energy bicrystal GBs. In addition, the excess free volume in GBs is expected to play an important role in GB creep [6.12]. Simulations suggest (see [6.11]) that lowering the stacking fault energy (SFE) results in a decrease of d_c which is confinned by the simulations for Al (high SFE, d_c = 18 nm) and Cu (lower SFE. dc = 14 nm) shown in Fig. 6.7b and c, respectively.

6.4 Plasticity Studies by Nanoindentation

The development of indentation and impression tests has a long tradition for measuring the mechanical properties of a material by making a contact of well-known geometry [6.34]. Owing to the development of new sensors and actuators, indentations can now be perfonned on sub-micron scales, a technique termed nanoindentation. Recently, a nanoindenter has been coupled in situ to a transmission electron microscope (TEM) for monitoring the stress-strain curve of the material together with the micrestructure of the material throughout the test [6.34]. The indenter is made from B-dopcd diamond for electrical conductivity to suppress electrical charging from the TEM electron beam so that no electrostatic force is exerted between the indenter probe and the specimen.

In Fig. 6.8 the stress-strain curve and TEM images of nanoindentation studies on Al arc shown with an initially dislocation-free Al crystallite in Fig. 6.8b. Figure 6.8c and e shows the grain's microstructure immediately after each of the lirst two dislocation bursts which, surprisingly, coincide with the barely discernible load transients 1 and 2 in Fig. 6.8a, i.e., they occur before a sustained rise in load. This shows that plasticity in a dislocation free volume of polycrystalline aluminum can begin at very small forces, remarkably, even before the first sustained rise in repulsive force (indicated by a star in Fig. 6.8a). However, the shear stress associated with these very small forces do approach the theoretical shear strength of aluminum (~2.2 GPa). The data in Fig. 6.8 supply evidence that a sub-micrometer grain of aluminum, plastically deformed to a dislocation density of — 10^{14}m^{-2}, is also capable of supporting shear stress close to the theoretical shear strength [6.35] which is contrary to earlier assumptions that a dislocation free volume is necessary to achieve shear stresses near the theoretical shear strength (sec [6.35]). This behavior may be attributable to grain boundaries acting as a barrier to dislocation motion [6.35]. The data are, furthermore, at odds with the prevalent notion that the lirst obvious displacement excursion in a nanoindentation test is indicative of plastic defonnation (see [6.35]).

Atomic simulation of nanoindentation in nanocrystallinc gold with a grain size of 12 nm shows dislocation nucleation within the grains at the onset of plastic deformation with the grain boundaries as an efficient sink for partial and full dislocations. Intergranular sliding and a decrease in Young's modulus are observed as the grain

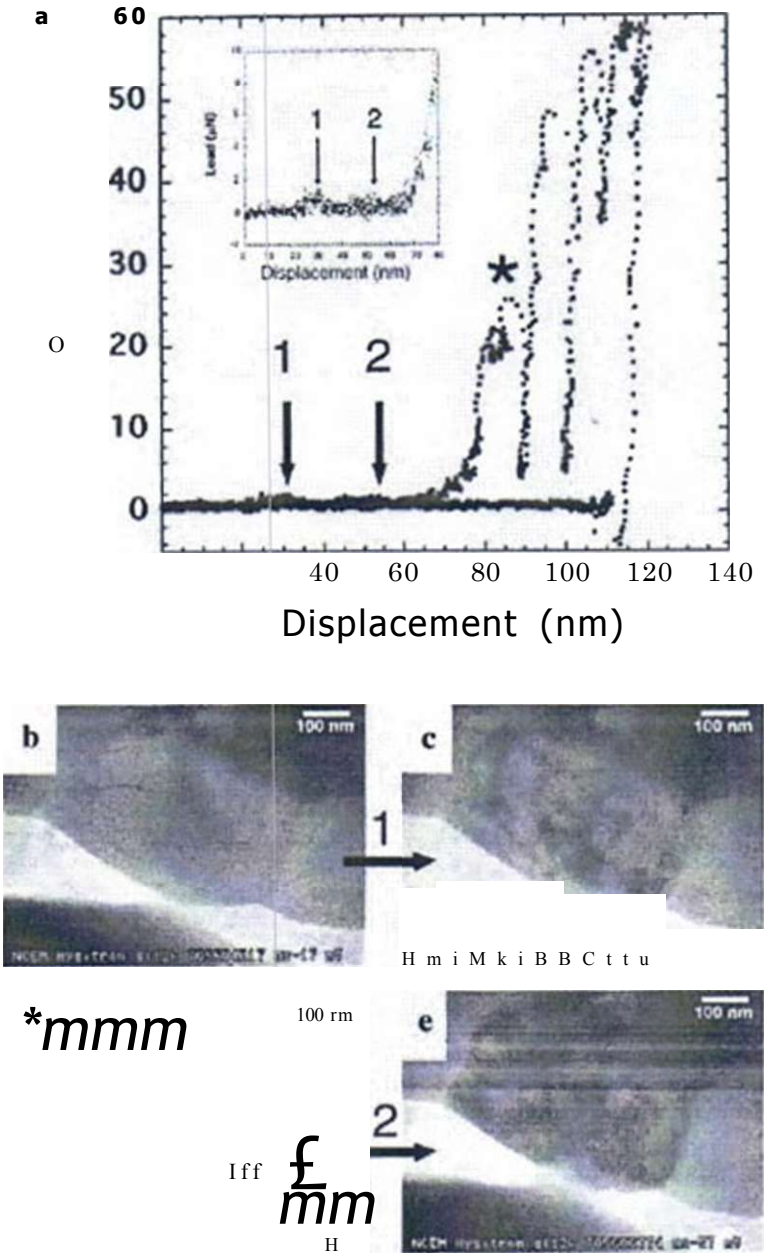

Fig. 6.8 (a) I.oad-displaccment curves, measured in an integrated nanoindcntcr-Tl:M facility. The *curve* exhibits several load-drop events as the indenter *(lower pari* in (b)) moves into the A1 grain *(upper pari* in (b)). Inset: Initial portion of the loading segment: *Arrows* point to tiny load peaks, corresponding to the first two dislocation bursts within the grain. The *star* indicates the first major load-drop event, (b), (c) and (d). (e) Sequential TEM images from the first and second dislocation bursts [6.34. 6.351- (Reprinted with permission from [6.34). © 2007 Elsevier)

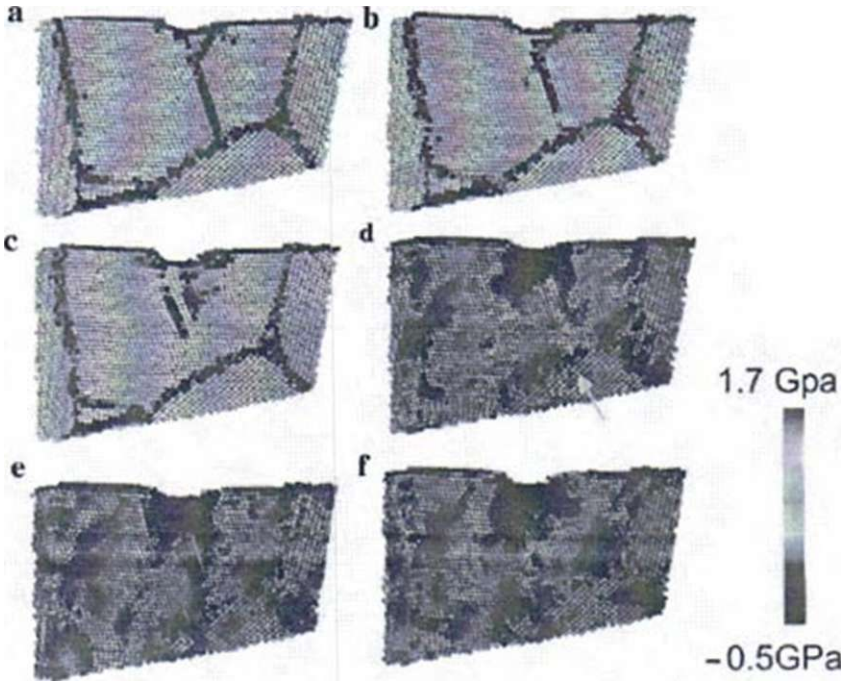

Fig. 6.9 Molecular dynamics indentation simulation of nanocrystallinc Au showing the interactions between dislocations and grain boundaries (GB). **(a-c)** Atomic configuration during loading and (d-**f)** corresponding stress distribution. Upon indentation, dislocations arc emitted from under the indenter and propagate through a grain until absorption by GBs. A dislocation is represented by two *red lines* (parallel planes) that mark a stacking fault left behind a propagating partial dislocation. The *yellow arrow* in **(d)** marks the region where the leading partial dislocation arrives. (Reprinted with permission from |6.37J. © 2004 Elsevier)

size is refined to 5 nm (6.361. When the indenter size is smaller than the grain size, the grain boundaries not only act as sinks but also reflect or emit dislocations (Fig. 6.9).

Molecular dynamics simulation of nanoindentation has been furthermore performed on nanocrystalline SiC ceramics [6.38, 6.39] with an 8-nm grain size and 19 million atoms in total. As the indenter depth h increases, a crossover is observed from a cooperative deformation mechanism involving multiple grains to a decoupled response of individual grains, e.g., grain rotation, sliding, and intragranular dislocation activity. The crossover is also reflected in a switch from deformation dominated by crystallization of the grain boundary material to deformation dominated by disordering (see Fig. 6.10). In the early stages of plastic deformation, the soft (amorphous) GB phase "screens" the crystalline grains from deformation, thus making nanocrystallinc SiC more ductile than its coarse-grained counterpart. Fracture toughness (a measure of how much energy it takes to propagate a crack) measured experimentally in nanocomposites (see [6.39]) exceeds that of a polycrystalline

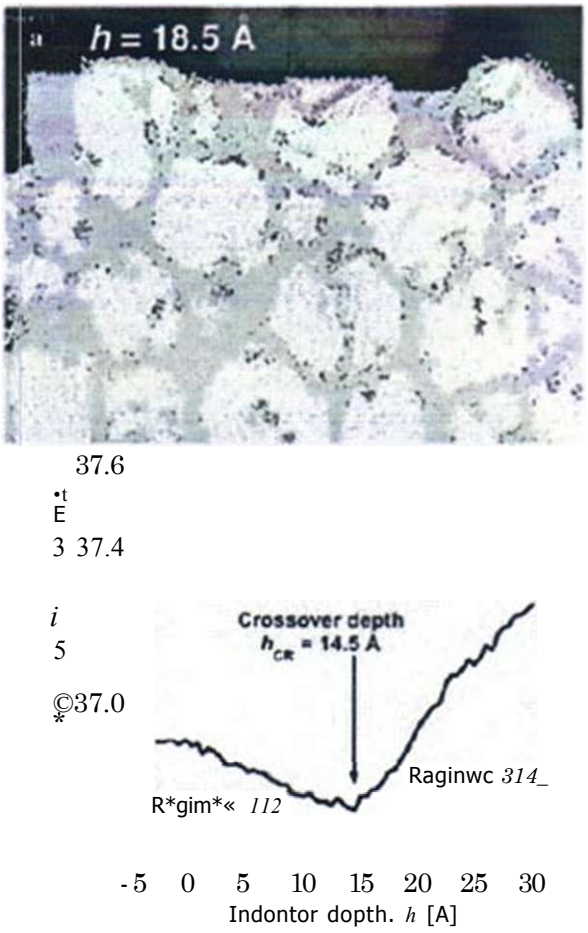

Fig. 6.10 (a) Atomic configuration of nanocrystallinc SiC with *white* grains and *yellow* GBs. At lower indentation depths *h,* the deformation of the material is dominated by rccrystallizalion *(blue* atoms). At depths $h > /r_{cr}$, deformation is dominated by disordering *(red* atoms), (b) Percentage of disordered atoms in the material as a function of *h* rcllccts the crossover in the deformation mcchanism. (Reprinted with permission from [6.38]. © 2005 AAAS)

matrix by about 50%. Increased fracture toughness docs not necessarily lead to a lower value of hardness. Nanoindentation experiments of nanocrystallinc SiC with grain sizes of 5-20 nm show the opposite trend [6.40] and report nanocrystallinc SiC to be superhard with hardness values of 30-50 GPa, higher than that of coarse-grained SiC. and a similar value (39 GPa) has been derived from the molecular dynamics simulations [6.39].

6.5 Ultrastrength Nanomaterials

Ultrastrength nanomatcrials (Table 6.1) have been reviewed before [6.41]. The strength of metals is dictated by dislocation nucleation and motion at low temperatures (see [6.131). In the absence of mobile dislocations in nanocrystallites, plastic

Tabic 6.1 Experimentally measured ultrahigh strengths. CNT, carbon nanotubes; NW. nanowires: NP. nanopillars; NS. nanosphcrcs; ML. monolayer, SW, single wall: MW, multiwall; *E,* Young's modulus, For references sec (6.41)

Material	Number of layers or diameter (nm)	Measured strength (GPa)	Ideal strength ~£/10 (GPa)
CNT	SW	30	100
CNT	MW	30	100
Ag-NW	16.5	7.3	8
Au-NW	40	5.6	8
Au-NP	300	0.8	8
Si-NS	20-50	20-50	17
Graphcnc	ML	130	100

deformation will not proceed until new dislocations are nucleated, which can lead to a high strength, approaching the ideal strength, which is the stress required to deform a pcrfect crystal to its clastic limit while maintaining perfect periodicity.

Ultrastrength can be achieved by dislocation exhaustion [6.41] or starvation [6.42], a concept explaining the high compressive strength of Au nanopillars (sec [6.41]) of about 800 MPa which is about 50 times higher than that of bulk Au and which is not so far from the prediction of the ideal shear strength from ab initio calculations (sec Tabic 6.1). Unlike in bulk samples, dislocations in nanostructures can travel only very small distances before being annihilated at free surfaces, thereby reducing the overall dislocation multiplication rate. Gliding dislocations leave the crystal more rapidly than they multiply, decreasing the overall mobile dislocation density which requires very high stresses to nucleate new mobile dislocations (see [6.41]).

Insight into source-controlled dislocation plasticity in a sub-micrometer Al crystal (300 nm x 400 nm x 400 nm) has been gained by in situ transmission electron microscopy in tensile tests [6.43]. Single-ended sources emit dislocations that escape tile crystal before being able to multiply (Fig. 6.11). As dislocation nucleation and loss rates arc counterbalanced, the dislocation density remains constant throughout the deformation at strain rates of about 10^{-4} s^{-1}. However, an increase in strain rate to 10^{-3} s^{-1} causes a surge in dislocation density as the nucleation rate outweighs the loss rate. This demonstrates that the deformation of nanometer crystals is strain rate sensitive [6.43].

One possible application of the extremely high strength of nanoparticlcs is to exploit their role as reinforcement to improve the mechanical properties of bulk materials. In this case strengthening is induced through the introduction of nanoscale precipitates, hindering the propagation of dislocations in the crystalline matrix [6.14]. The precise mechanism of the strengthening depends on the size of the nanoparticlcs [6.44] and their structure can be altered through their interaction with the dislocations. Small nanoparticlcs of 3-5 nm in diameter can be structurally stable at high temperatures and lead to a six orders-of-magnitude increase in crccp resistance (see [6.13]). The limit of precipitate strengthening is determined by both

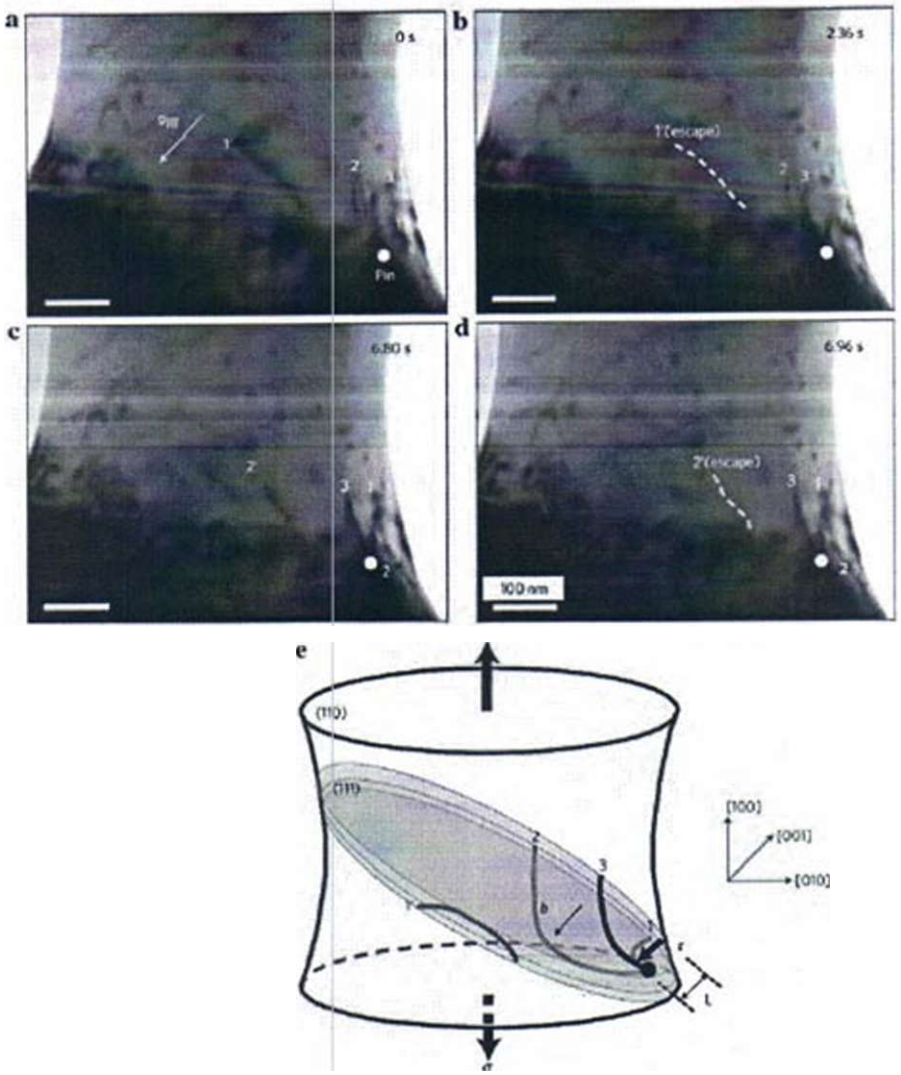

Fiy. 6.11 Dislocation emission in the tensile test of an Al nanocrystal by the operation of a single-ended source, **(a-d)** Scqucncc of transmission electron micrographs (TEM) showing singlc-cndcd dislocation sources lying on a set of parallel slip planes 1. 2. and 3 at *e* * 140%. (e) Schcmatic of the dislocation configuration corresponding to **(a).** The previously generated dislocations from sources 1 and 2 are labeled as 1* and 2', respectively. The source size is 70 ± 20 nm. Upon generation, the dislocations glide and rcach the surfacc in proximity with aligning their lines in parallel to the surfacc in edge character and intersecting the surfacc perpendicularly owing to image forces. (Reprinted with permission from (6.43]. © 2009 Nature Publishing Group)

the strength of the nanoscale precipitates and the elastic properties of the matrix and may approach the ideal strength [6.14J.

6.6 Enhancement of Both Strength and Ductility

When designing materials, there is often a trade-off between strength and ductility - properties that are critically important to the performance of materials. This is also true for bulk nanostructured materials, which usually have a high strength, but disappointingly low ductility (see [6.45, 6.46]). Techniques have been developed to make a nanostructured material both strong and ductile [6.46, 6.47], and by simulation methods [6.45] it has been revealed why some nanodesigncd materials behave with that desirable compromise between strength and ductility by visualizing tlie simulation of materials deformation on a timescalc of minutes.

Nanocrystallinc metals are several times stronger than conventional microcrystallinc metals (Fig. 6.5) but often more brittle (less ductilc). However, in many

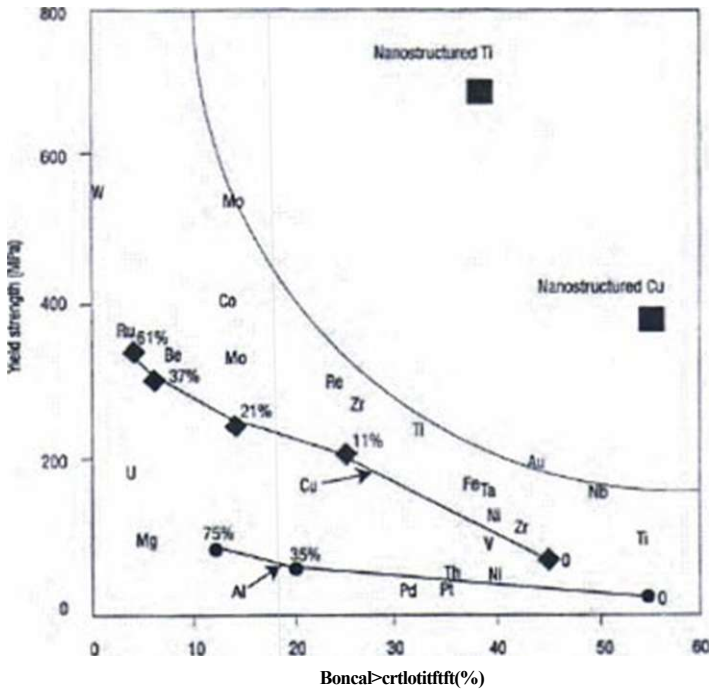

Fig. 6.12 Strength and ductility of severely plastically deformed nanostructured Cu and Ti compared with coarsc-grained metals. Conventional cold rolling of Al and Cu *(full lines* with percentage of rolling indicated) increases the yield strength but decreases the ductility. In contrast, the high strength and ductility of nanostructured Cu and Ti differ very much from the behavior of coarsc-grained metals. (Reprinted with permission from [6.48]. © 2004 Nature Publishing Group)

applications one needs optimum combinations of strength and ductility [6.45] which has been demonstrated in severely plastically deformed nanocrystallinc Cu and Ti (Fig. 6.12) and in nanotwinned copper [6.47], by a bimodal distribution of grain sizes and by low-temperature/high-strain rate deformation (see [6.49]). Copper with tunable combinations of strength and ductility could be produced by controlling the thickness and nanospacing of twin boundaries inside small grains [6.47] (Fig. 6.13a, b). Internal interfaces such as grain boundaries and twin boundaries play a critical role in the strength and ductility of metals. When there arc smaller grains in the metal structure, and hence more grain boundaries, there is more interaction between the boundaries and dislocations (string-like defects in the material) that move inside and between grains during mechanical deformation. The larger portion of these boundaries contributes to the britlleness of the metal. Adding nanoscalc twin boundaries has a similar strengthening effect, but the twin boundaries do not promote the same level of britlleness as grain boundaries do (see [6.45]). Simulations reveal [6.45] that the ductility of nanotwinned copper can be

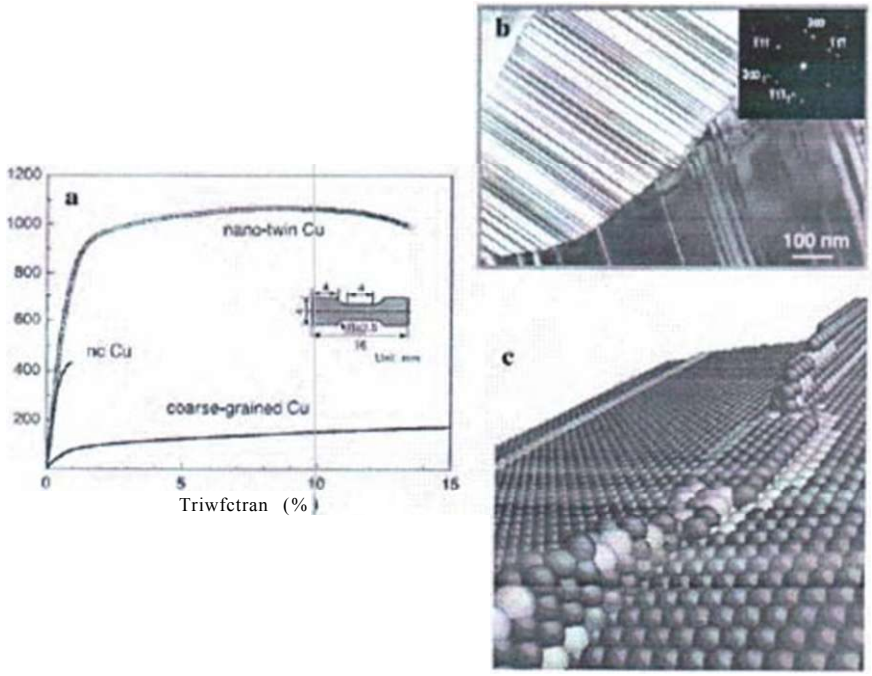

Fl^. 6.13 High mochanical strength and ductility of nanotwinned Cu. (a) Stress-strain curves of clectrodcpositcd nanotwinned Cu. of nanocrystallinc Cu, and of coarse-grained Cu |6.47|. (b) Electron diffraction patterns (*inset*) indicate that the twins in each grain (transmission electron micrograph - TEM) are parallel to each other in [111 } planes [6.47]. (c) Atomic simulation shows the absorption of a line defect by a twin boundary in nanotwinned Cu [6.45. 6.50]. (Reprinted with permission from [6.47J (a) (b) and [6.45] (c). © 2004 AAAS (a) (b) and © 2007 National Academy of Sciences USA (c))

attributed to changes in the atomic structure of the twin boundaries as the material is deformed (Fig. 6.13c). From molecular dynamics (MD) simulations for copper it is concluded (6.51] that, since the dislocation nuclcation is suppressed in the vicinity of the coherent twin boundaries (TBs) and each TB plane hinders dislocations from propagating, the coherent TBs can be regarded as an intrinsic strengthening phase relative to a perfect crystal. Furthermore, a comparison of experimental evidence and calculations (sec [6.52)) demonstrates that dislocation/interface interactions, rather than dislocation/dislocation interactions, arc the rate-controlling mechanisms in the TB-dominatcd materials. It was found in nanotwinned copper [6.53] that the strength increases with decreasing twin thickness, reaching a maximum at 15 nm, followed by a softening at smaller values.

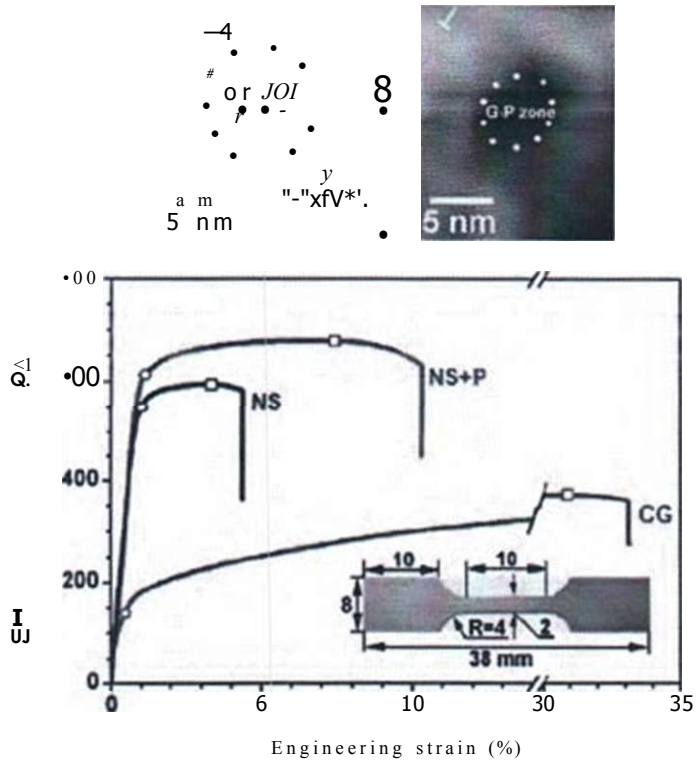

Fig. 6.14 (a) High-resolution transmission electron micrograph (HRTEM) of a [111| matrix plane of a nanostnictured 7075 Al alloy with a Guinier-Prcston zone precipitate (NS+P specimen) before and **(b)** after tensile testing. The *white dots* mark the particle/matrix interface and the *white T symbols* designate edge dislocations, (c) Tensile engineering stress-strain curves of the coarse grained (CG), nanostnictured (NS). and the nanostruclurcd Al alloy specimen with nano-precipilations (NS+P). The *inset* shows the tensile specimen with a thickncss of 1 mm. (Reprinted with permission from [6.46]. © 2006 Wiley-VCII)

Another technique for a simultaneous increase of strength and ductility has been demonstrated by engineering very small sccond-phasc particles into a nanostructurcd alloy matrix (6.461. In a cryogcnically rolled 7075 AI alloy with a 100-nm grain size (NS sample), second-phase nanoparticlcs (such as Guinier-Preston zones; Fig. 6.14a, b) with sizes between 4 and 10 nm were precipitated (NS+P specimen) yielding an increased strength (engineering stress) and ductility (engineering strain) compared to coarse-grained (CG) or nanocrystallinc (NS) specimens (Fig. 6.14c). The high dislocation density and the line grain size of the NS specimen arc responsible for its enhanced strength over the CG sample, while the high density of second-phasc particles in the NS+P specimen is responsible for the increased strength compared with the NS specimen. The enhanced elongation (ductility) of the NS+P specimen (Fig. 6.14c) is ascribed to the increased work hardening rate, *0* (slope of the stress-strain curve), through dislocation accumulation at the precipitates with an increase of the dislocation density from 3.5 x 10^{14} m~^{2} before tensile testing to 5.4 x 10^{14} m^{-2} after testing (Fig. 6.14a, b). The second-phase precipitates significantly reduce dynamic recovery and increase the dislocation storage capability, leading to an enhancement of the hardening rate, 0. and of the ductility.

6.7 Superplasticity

Supcrplasticily is the deformation process that produces essentially neck-frce elongations of many hundreds of pcrccnts without failure in materials deformed in tension (see [6.29, 6.54, 6.55]). A reduction in grain size decreases the temperature and increases the strain rate of superplastic flow. Examples for superplasticity tensile tests on nanocrystallinc materials are shown in Fig. 6.15. Exceptionally high superplastic elongations of 3050% have been achieved at 473 K with a strain rate of 10~^{4} s^{-1} in a commercial Mg - 5.5 wt% Zn - 0.5 wt% Zr alloy with a grain size of 800 nm after processing by equal-channel angular pressing [6.56]. Superplastic behavior is of industrial interest, as it allows for net-shape fabrication of components with complex shape from materials that are hard to machine, such as compositcs or intcrmctallics.

Superplasticity of nanocrystallinc materials is characterized by very high values of the flow stress, the strengthening in the first stage of deformation and a softening in a second deformation stage (Fig. 6.16a). Dangerous stress concentrations leading to cracking and failure must be avoided. It is thought (see [6.29]) that superplastic deformation occurs in nanocrystallinc materials, if grain boundary sliding serves as the dominant deformation mechanism whose operation and effective accommodation are provided by lattice dislocation slip, fast atomic diffusion, diffusion-controlled deformation by grain rotation, and triple-junction migration.

According to a detailed discussion [6.29], grain boundary sliding is supported by the slip of lattice dislocations which are generated under a critical stress $cr_c \sim Gb/ML$ (*G* - shear modulus, *b* - Burgers vector, *M* ^ 0.5 a geometrical factor.

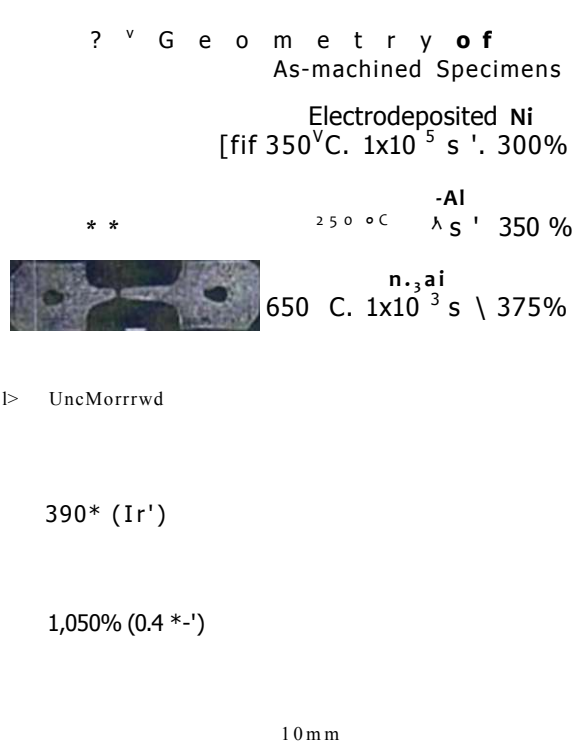

Fig. 6.15 **(a)** Tensile specimens of Ni (grain size 20 nm). AI alloy (100 nm). and Ni3AI (50 nm). shown in the initial geometry and after deformation [6.57). (b) Supcrplasticity of a ceramic specimen composed of Z1O2 (180 nm) witha-AI_2O_3 (250 nm) and $Mg01.3Al_20j$ spinel (180 nm) [6.61]. (Reprinted with permission from [6.57] **(a)** and [6.61] (b). © 1999 Nature Publishing Group (a) and © 2001 Nature Publishing Group (b))

L % 0.3d the length of a Frank-Read dislocation segment in a grain of the size d [6.58]). An estimate for nanocrystalline materials yields $a_c \sim 0/60 - G/30$ which is close to experimental values (see [6.29,6.57]). This shows that the measured flow stress is high enough to activate Frank-Read sources for the generation of lattice dislocations in intermediate grains of nanocrystalline materials. The lattice dislocations then move to grain boundaries to be absorbed there and to be transformed into mobile grain boundary dislocations that carry grain boundary sliding. The storage of GB dislocations (Fig. 6.16b—i) causes the experimentally observed strengthening of nanocrystallinc materials in the first stage of superplastic deformation, in contrast to coarsc-grained materials where strengthening originates from the storage of lattice dislocations in the grains.

The storage of grain boundary dislocations at triple junctions may lead to stress sources, inducing nanocracks and failure. Nanocrack nuclcation under superplastic deformation of nanomaterials can be suppressed by accommodation effects of lattice dislocation slip, diffusion-assisted grain rotation, local diffusion processes, and, in particular, by the emission of lattice dislocations from triple junctions. Grain rotation which occurs through diffusion-assisted climb of GB dislocations serves as the key recovery process for the GB dislocation density and thereby can suppress nanocrack nuclcation.

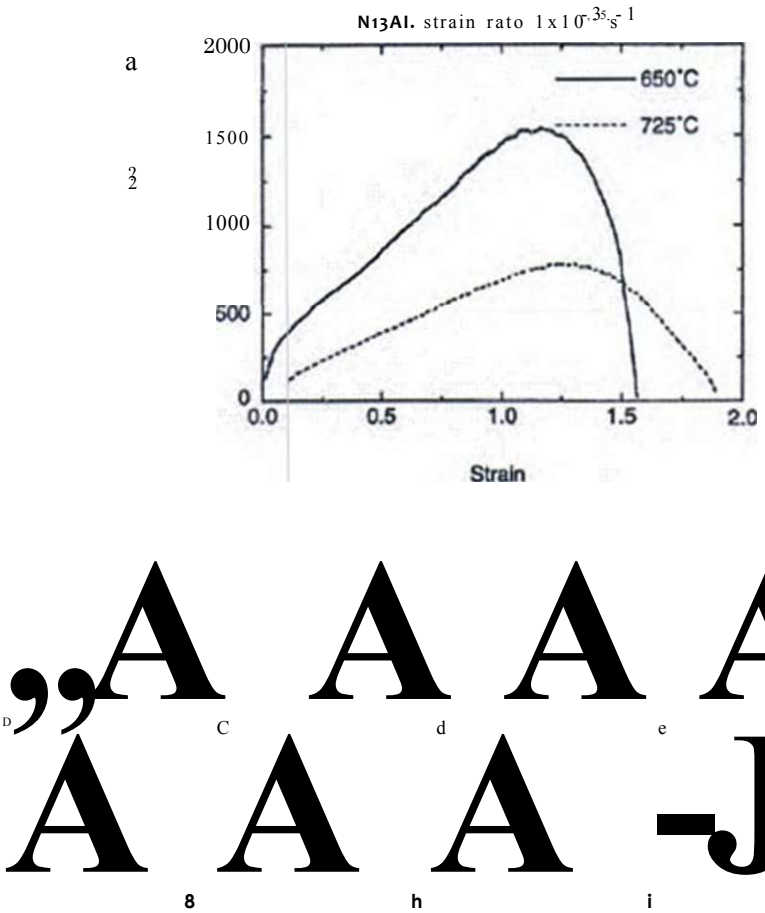

Fig. 6.16 **(a)** Supcrplastic stress-strain curvcs of nanocrystallinc NijAl (grain size 50 nm) prepared by severe plastic deformation |6.57|; (b-1) Grain boundary sliding and transformation of dcfcct structures near a triple junction of grain boundaries; **(i)** the transfer of grain boundary dislocations across the triple junction O results in the increase of the magnitude of the Burgers vector of a sessile dislocation and the formation of a planar array of GBs for easy GB sliding giving rise to softening in the second supcrplastic deformation stage [6.29]. (Reprinted with permission from [6.57] **(a)** and [6.29] **(b-i).** © 1999 Nature Publishing Group **(a)** and © 2005 Advanced Study Center (b-1))

The softening of nanomatcrials under supcrplastic deformation is related to triple junction migration that accommodates GB sliding (Fig. 6.16b-i) [6.29, 6.59]. This results in the experimentally observed [6.60] formation of plane arrays of GBs (Fig. 6.16i). In this geometry, triple junctions stop being obstacles for GB sliding along coplanar grain boundaries. The subsequent cooperative grain boundary sliding gives rise to the softening in the second stage of superplastic deformation.

Notwithstanding the recent progress in the field, the achievement of superplasticity or good ductility of superstrong nanocrystalline materials at commercially desired high strain rates and at room temperature are major unresolved topics in this research area.

6.8 Fatigue

Fatigue of metallic materials is an important issue in the Held of mechanical behavior. Because enhanced fatigue properties arc associated with high tensile strength and good ductility, nanocrystalline materials are particularly susceptible to fatigue failure when strength and/or ductility are poor (see 16.62, 6.631). Although most nanocrystallinc metals (e.g., manufactured by severe plastic deformation 16.63]) exhibit a shorter fatigue life compared to their coarse-grained counterparts because some ductility is lost during manufacturing, an enhancement of the fatigue life has been observed for nanocrystalline Ti and for CuCrZr alloys after severe plastic deformation (SPD; see 16.63]).

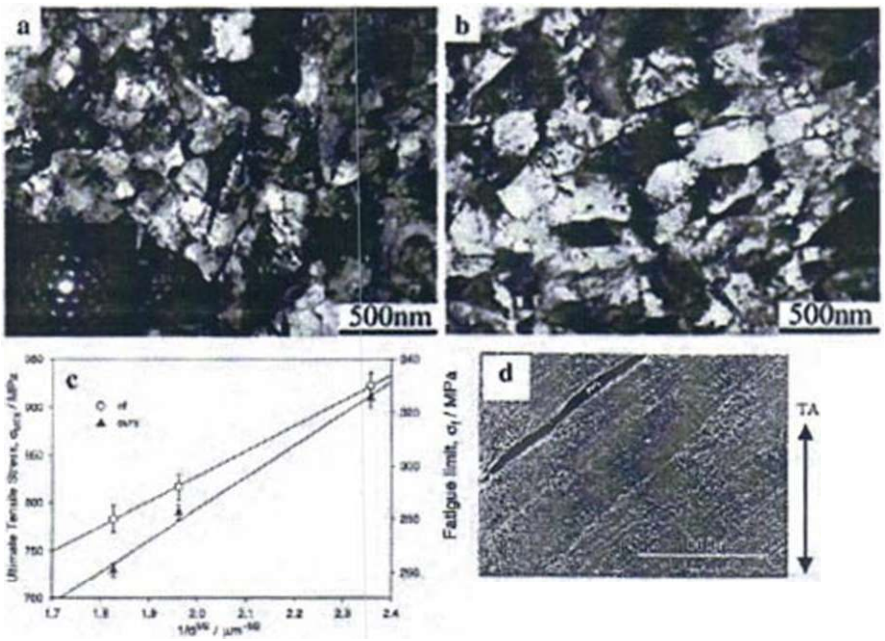

Fig. 6.17 (a) Invar, manufactured by severe plastic deformation (SPD). before and (b) after fatigue at a cumulated fatigue strain of Afpe/2 = 10^{-3}; (c) Hall-Petch behavior of the ultimate tensile strength ^uts fid the fatigue limit of of a SPD manufactured nanocrystallinc Invar alloy, (d) Shear bands on the surface of SPD nanocrystallinc Cu deformed cyclically to Afpc/2 = 10^{-J}. (Reprinted with permission from (6.63]. © 2003 Wiley-VCH)

As an example, the structure of SPD nanocrystallinc Fe-36Ni (Invar) with equiaxed sub-micron-sized grains before fatigue and after fatigue with a cumulated plastic strain A£pc/2 = 10^{3} and significantly elongated grains are shown in Fig. 6.17a, b. For the ultimate tensile strength aurs and the fatigue limit Of a Hall-Petch behavior is found (Fig. 6.17c). Detailed studies on ultrafine-grained pure metals have been performed for Cu (6.64,6.65] and Ni (6.66). In cyclic deformation of SPD nanocrystallinc materials, strain localization in shear bands oriented at 45° to the tensile loading axis are observed (Fig. 6.17d). In the shear bands, where the strain localization occurs primarily along the grain boundaries, cracks are initiated and propagated (sec [6.63]).

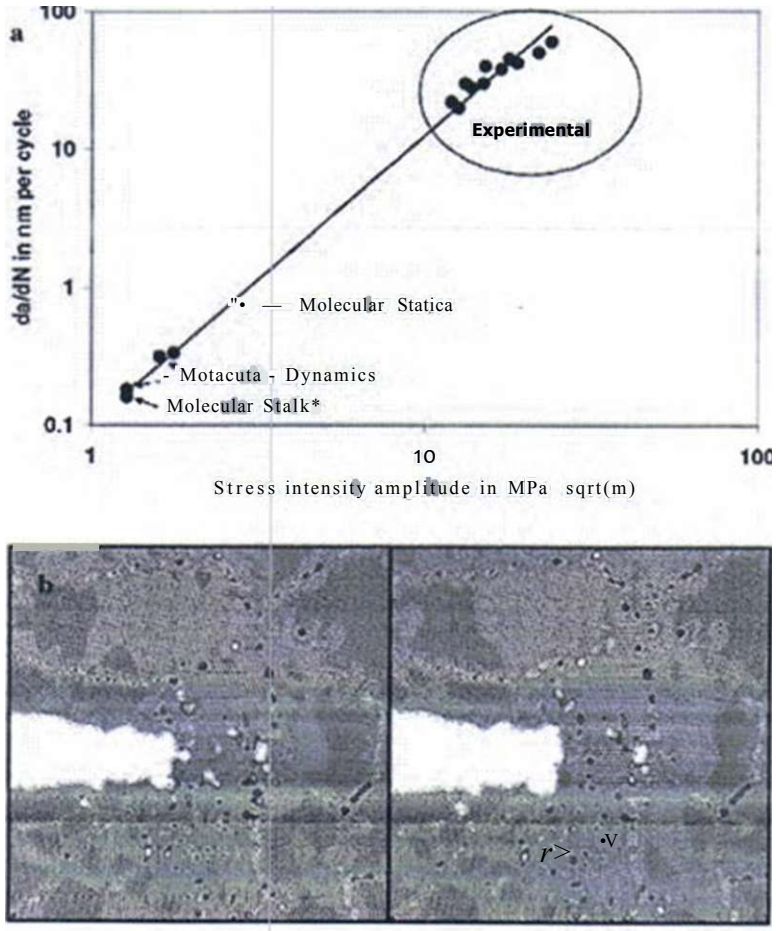

Fig. 6.18 (a) Rate of crack advance for both molecular statics and dynamics simulations (6.621 together with experimental data [6.67J: (b) Crack tip configurations for 26 *(left)* and 31 *(right)* cycles showing nanovoids essentially within the grain where the crack tip is located. (Reprinted with permission from [6.62]. © 2005 American Physical Socicty)

Although the details of die inicrosopic mechanism of fatigue damage of nanocrystallinc materials have still to be uncovered [6.63], atomic simulation studies may shed some light on these processes [6.62]. In these studies, a combination of molecular statics and molecular dynamics making use of an embedded-atom method (EAM) potential for Ni has been utilized. The calculated rates of crack advance are compared to experimental values (Fig. 6.18a). Regarding the mechanism of crack advance, the calculations suggest nanovoids to be created in die grain where the crack tip is located (Fig. 6.18b), with most of the dislocations being unable to continue to glide across the grain boundary. However, the experimental data of fatigue failure of nanograincd Pt films are ascribed to dislocation-slip mediated processes [6.68], known to operate in fee metals during fatigue, and not to plastic blunting and void coalescence mechanisms observed in MD simulations.

6.9 Nanocomposites

A critical challenge in nanocompositc fabrication is the ability to realize materials that allow the transfer of the exceptional mechanical properties (e.g., tensile strength, CTUTS', Young's modulus, *E)* of the nanoscale materials to the macroscalc properties of the bulk material 16.69]. In addition, novel optical features will arise from the interfaces of, e.g., metal oxides/polymer interfaces. This will be discussed in the following, comprising rccent examples of nanocomposites from metals, ceramics, and polymers.

6.9.1 Metallic Nanocomposites

Materials with both high strength and high ductility can be manufactured from Zr based Zr-Nb-Cu-Ni-AI alloys [6.70] by simple casting of appropriate alloy compositions. These composites consist of a ductile dendritic bcc-Zr phase and a strong nanostructured matrix (Fig. 6.19a, c). The dendritic phase exhibits work hardening and enhances the ductility of the compositcs reaching plastic strains of 17.5% whereas the nanostructured matrix enhances the strength to high values of about 1900 MPa (Fig. 6.19d). Catastrophic failure can be avoided for compositcs with larger amounts of dendrites (alloys C3-C5; see Fig. 6.19d). On the other hand, the yield strength decreases with increasing bcc dendrite volume fraction. The glassy sample (alloy G in Fig. 6.19d), the nanocrystallinc sample (NC), and die quasi-crystalline alloy (QC) show practically no ductility. Due to the heterogeneous structure, the deformation mechanisms of the nanocompositc are quite complicated. The shear bands, spreading in the matrix and interacting with the dendrites, exhibit intcr-band spacings of about 150 nm [6.70], yielding essentially homogeneous strain distribution during deformation. After nuclcation, cracks propagate through the shear bands, whereas the dendrites act as crack blunting objects, thus enhancing the toughness of the nanocompositc.

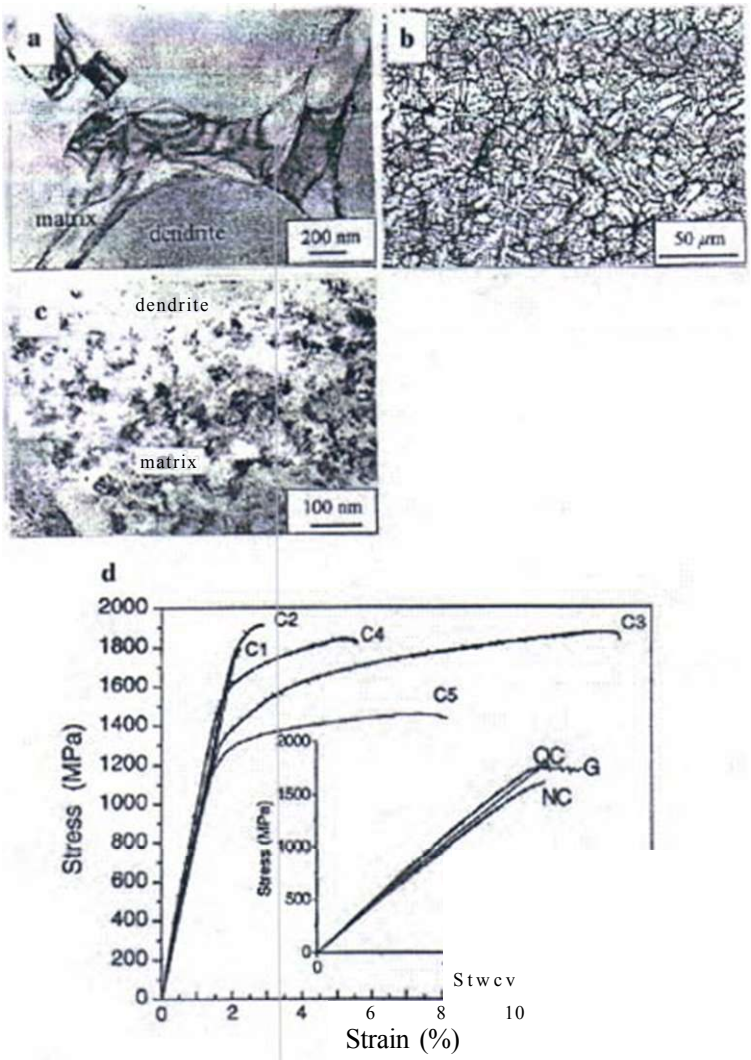

Fly. 6.19 (a) TEM image of Zr^NbisCujNifcgAl^ dendrites in a nanostnictured matrix, (b) SEM image of a Z^.jNbgCi^Nii Al9.5 nanocompositc (alloy C4) with 88 vol% dendrites in a (c) $CuZr_2$-type nanocrystalline matrix (TEM). (d) Stress-strain curves of Zr-Nb-Cu-Ni-AI nanocompositcs with various compositions and dendrite volume fractions (alloys C1-C5) or of Zr-Tt-Nb-Cu-Ni-AI alloys (G - bulk metallic glass. QC - 90 vol% quasi-crystalline + glassy composite. NC - 10 xo\% nanocrystallinc + glassy composite. (Reprinted with pennission from f6.70]. © 2005 Wiley-VCH)

The combination of high ductility, strength, and elasticity of these nanocompositcs is promising for engineering applications for springs, microgcars, medical devices, sporting equipment, etc.

6.9.2 Ceramic/Metal Nanocomposites with Diamond-Like Hardening

The design of materials with a hardness similar to diamond is an ongoing challenge because diamond cannot be used in machining steels due to its reactivity with materials such as Fe, Ti, or Si. The synthesis of alternative supcrhard materials including carbides, nitrides, and borides, however, requires extreme conditions (6.71). Therefore, the supcrhard behavior of alumina (grain size 300 nm) and Ni (< 60 nm) nanocomposites (Fig. 6.20) were studied [6.72] after spark-plasma sintering, making use of the strategies of Hall-Petch strengthening of nanocrystalline solids (see Sect. 6.3) and of percolation theory. When the concentration of Ni increases, the hardness of the composite increases (Fig. 6.20e). It is initially enhanced due to an increase of the number of Ni particles. However, when the metal concentration is further increased, it reaches a critical value with maximum hardness until single Ni particles start to coalesce, leading to increased particle sizes and a decrease in hardness. In fact, the hardness of the present alumina-n-Ni (2.5 vol%) nanocomposite corresponds to an alumina-diamond (6 vol%) composite with a substantially higher diamond contents, if the rule of mixing is applied. In addition, the alumina-n-Ni (2.5 vol%) nanocomposite was found to exhibit an excellent wear

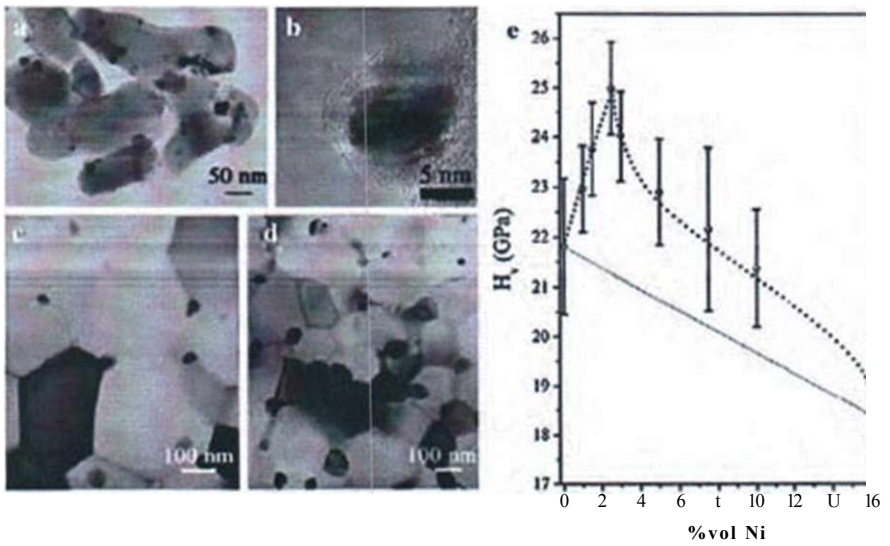

Fig. 6.20 Transmission electron micrographs of (n) alumina/n-Ni powder containing 1 vol% Ni. (b) high-resolution electron micrograph of the alumina-n-Ni interface of the powder containing 1 vol% n-Ni particles, (c) spark-plasma sintered alumina-n-Ni composite (1.5 vol% Ni). (d) sintered alumina-n-Ni composite (5 vol% Ni), and (e) hardness as a function of Ni contents. Measured and theoretically predicted *(dashed line)* hardness values plotted as a function of the Ni contents. The *solid line* represents the rule of mixing. (Reprinted with permission from (6.721. *O* 2007 Wiley-VCH)

behavior with a wear rate by a factor of 30 smaller than that of pure alumina and about 15 times lower than that of B4C.

6.9.3 *Oxide/Dye/Polymer Nanocomposites - Optical Properties*

Nanocomposites of oxides and polymers (e.g., PMMA) can fluoresce emitting photons of a particular wave length (fluorescence) when excited by irradiation with shorter wave lengths. The fluorcscence is excited by photon absorption in the ccramic core (~5 nm) of the composite and the energy is transferred to the (C=0)-0 bond in the ccramic/PMMA interface (Fig. 6.21a) for fluorescence between 400 and 475 nm. In Zr()2/m-PMMA nanocompositcs with a particle diameter changing from 4.5 to 2.0 nm the emission spectra (Fig. 6.21c) blue shift from 434 to 418 nm and the emission intensity increases upon decreasing the particle

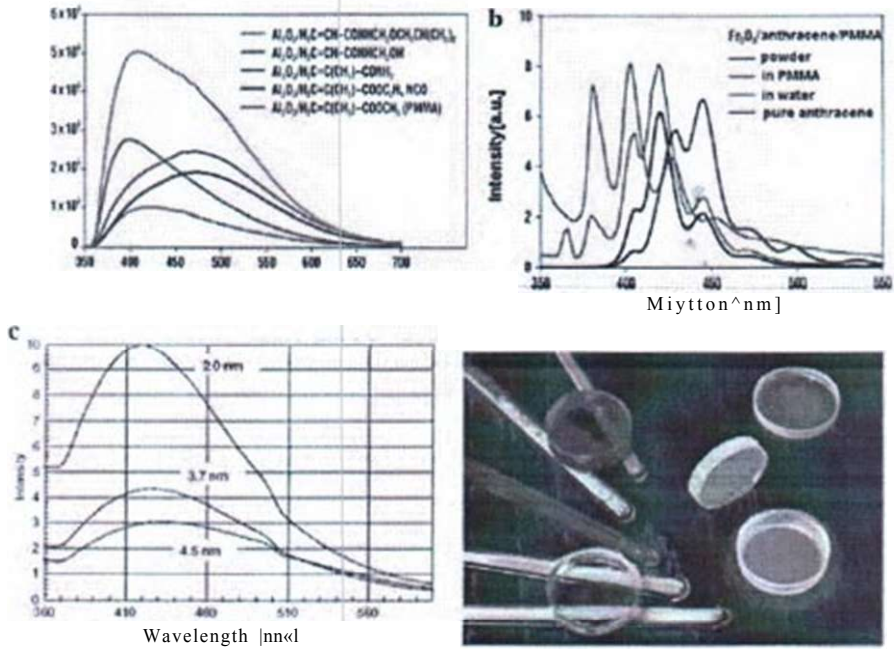

Fig. 6.21 (a) Fluorcscence spectra of AliCVpoIymcr nanocompositcs. Polymers including amide or isocyanatc groups enhance the fluorcscence intensity, (b) Huorcscence spectra of y-1ᶜc>O3/anthraccnc/PMMA nanocompositcs with emission wave lengths depending on the surrounding chcmistry [6.73|. (c) Influence of the particlc diameter (4.5-2.0 nm) of ZrO;/m-PMMA nanocompositcs on the emission spectra. The emission wave length blue shift (from 434 to 418 nm) and the emission intensity increases with decreasing particlc size [6.74]. (d) Metal oxide/dyc/polymer nanocomposite powders in glass tubes and dispersed in a PMMA matrix [6.73]. (Reprinted with permission from [6.73] **(a)** (b) (d) and [6.74] (c). <0 2005 Karlsmhcr Institut fUr Technologic (a) (b) (d) and <0 2004 Springer Verlag (c))

size. The range of fluorescence wave lengths can be widely expanded by making use of an intermediate monolayer of organic dyes, such as the model dye anthracene. In Fig. 6.21b the fluorescence spectra of paramagnetic FejOj/anthracene/ PMMA nanocomposites arc shown which could be of interest in biological analysis and medical diagnosis. By introducing such a nanocomposite into a PMMA matrix, transparently colored materials can be manufactured (Fig. 6.2Id).

6.9.4 *Polymer Nanocomposites*

This term has evolved to refer to a mult(component system in which the major constituent is a polymer and the minor constituent has at least one dimension below 100 nm (6.75-78]. Hybrid organic-inorganic nanocomposites of polymer and clay nanoplatelets (see also Sect. 11.6) have received special attention because of the very low cost of the inorganic component and the relatively simple preparation [6.69] with growing commercial importance (6.79]. Polymer nanocomposites are preferred over metals for moderate temperature applications (C 300°C) based on their weight savings, fatigue resistance, and corrosion suppression [6.80]. The advantages of polymer nanocomposites result primarily from the filler size reduction with the concomitant increase in the volume fraction of the relatively thick organic-inorganic interface structure [6.78] which extends into the polymer matrix on the order of R_z 6 nm [6.781. the radius of gyration [6.81], or approximately the expanse of the polymer molecule. The interfacial volume fraction additionally depends on the aspect ratio of the nanoparticlcs (6.78]. The patent and literature activity in this field has been rapidly increasing during the last decade (6.78]. Some recent studies will be briefly discussed in the following.

Polymer nanocompositcs have been produced (6.69] with properties that approach the theoretical maxima using spatial and orientational control of clay platelets in a polymer matrix at the nanoscale and retaining this order at the macroscale. Montmorillonite (MTM) clay (aluminosilicatc, ~1-nm thick by 100-1000 nm sheet diameter. Fig. 6.22a) with a theoretical in-plane elastic modulus of ~270 GPa [6.821 should yield polymer composites with theoretical stiffness values of —100 GPa, but values achieved to date were at least one order of magnitude lower bccause of clay aggregation and phase separation. Layer-by-layer (LBL) assembly was utilized [6.69] to sequentially coat a surfacc (Fig. 6.22a) with nanometer-thick layers of polyvinyl alcohol) PVA and MTM, yielding, e.g., 300-bilayer films with a thickness of 1.5 p.m (Fig. 6.22c, d) and an average thickness of ~5 nm per bilayer. The PVA/MTM pair has two unique properties. First, the hydrogen bonding is highly efficient because the distance between the O atoms of clay with 0.275 nm and of the H atoms of PVA with 0.265 nm makes hydrogen bonding epitaxial. Second, a substantial part of the efficient bonding and load transfer between the PVA and the inorganic MTM is attributed to the cyclic cross-linking to easily accessible A1 atoms on the surface and along the edges of MTM platelets. One A1 atom, two O atoms, and three C atoms from PVA participating in this bond form a

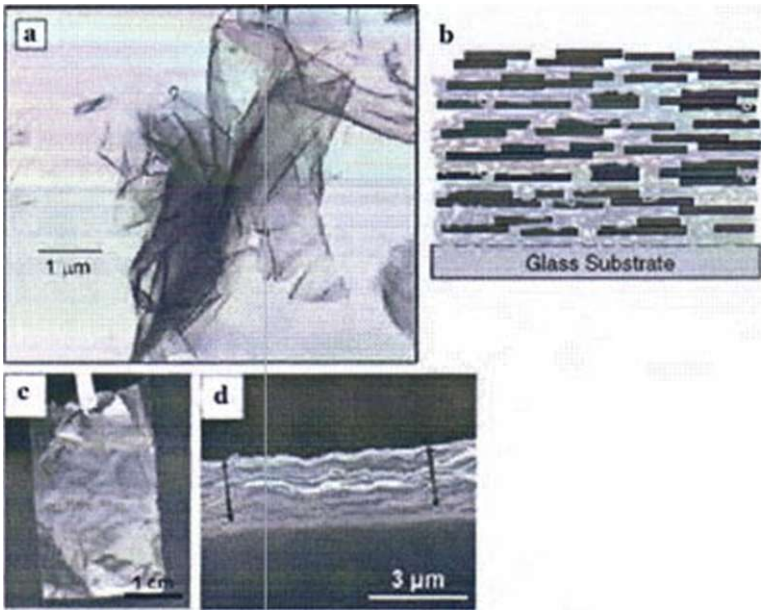

Fig. 6.22 (a) Transmission electron micrograph of refined montmorillonitc (6.79). **(b)** Schcmatic representation of the nanoarchilecture of a PVA/MTM (poly(vinylalcohol)/montmorillonitc) nanocompositc with eight bilayers and a ~5 nm bilayer thickness, (c) Free standing, 300-bilaycr PV/V MTM composite film showing high flexibility and transparency, **(d)** Scanning electron micrograph of the cross scction of the multilayer film with the *arrows* indicating the span of the cross section |6.69]. (Reprinted with permission from (6.79) **(a)** and [6.69] **(b-d).** © 2007 Materials Research Socicty **(a)** and © 2007 AAAS **(b-d))**

six-membered ring structure, which is known to be particularly stable (Fig. 6.23a, b). Experimental data from Fourier transform infrared (FTIR) spectroscopy, nuclear magnetic resonance (NMR), and x-ray photoelcctron spectroscopy (XPS) evidence the formation of AI-PVA covalent linkages. In addition, the PVA/ MTM films were treated with glutaraldchydc (GA) to further the bonding and load transfer between the -OH groups and the clay surface, as again demonstrated by NMR and FTIR studies. GA is a highly efficient cross-linking agent for PVA that forms covalent acetal bridges between -OH groups of the polymer chains as well as the hydroxyl groups present on the MTM sheets. The cross-linkcd free-standing PVA/ 50 vol% MTM films show a high strength (Fig. 6.23c), flexibility, and an 80-90% transparency [6.69]. This can be explained by the nanoscalc dimensions of the inorganic phase and the nearly pcrfcct orientation and dispersion of the MTM platelets. The ultimate tensile strength is increased by nearly a factor 3 over that of PVA/MTM without cross-linking and 10 tunes that of pure PVA, to values as high as 480 MPA. The modulus of cross-linked PVA/MTM cxcecds that of PVA/MTM without cross-linking by a factor of 10 and that of pure PVA by a factor of 100, with the high values of 125 GPa, similar to that of Kevlar (80-200 GPa). In addition, the cross-linked

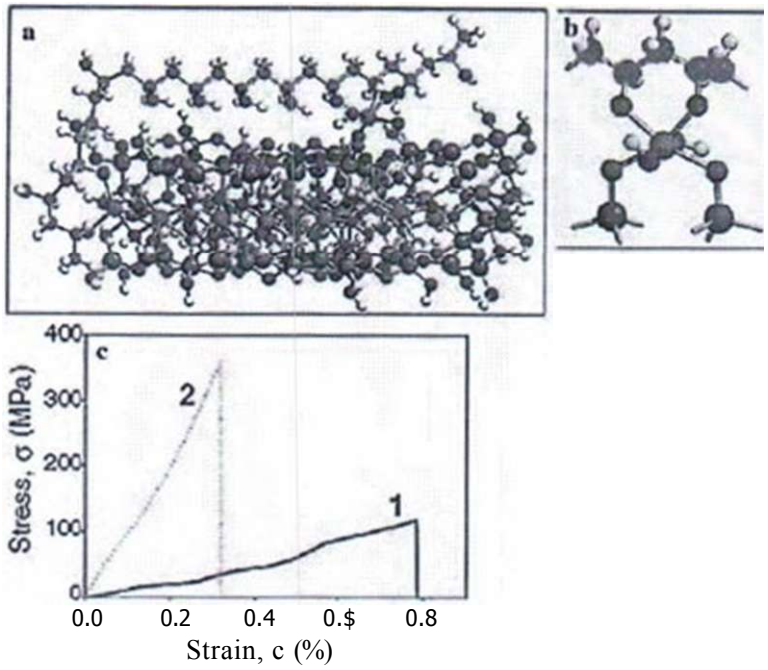

Fig. 6.23 (a) Characterization of the molecular interaction between polyv inyl alcohol) (PVA) and montmorillonite (MTM) clay. Energy optimized geometry of bonding between PVA and MTM obtained by calculations with a semi-empirical algorithm, (b) Enlarged portion of the six-mcmbcrcd cycle formed between PVA and MTM. *Al, purple:* O. *red:* H. *light gray:* Si. *dark gray:* C. *green,* (c) Stress-strain curves for 300-bilaycr PVA/ MTM composites (/) without and (2) with glutaraldehyde (GA) cross-linking. (Reprinted with permission from [6.69]. <D 2007 AAAS)

PVA/MTM composites show exceptional stability to humidity due to the covalent character of the bonding. It is believed [6.69] that the understanding of these results lies in the effective stiffening of the PVA matrix (due to a constrained motion of the polymer chains) becausc of its close proximity to and many interactions with the MTM platelets. The strengthening and modulus enhancement in the PVA/MTM nanocomposites with GA is considered to be a result of the likelihood that a polymer chain interacts strongly with two or more clay platelets, thereby improving the particle-to-matrix-to-particle load-transfer process over that in PVA/MTM.

The secret of nacre (see Fig. 6.24a and Sect. 11.6), which combines both high strength and toughness with lightweight, is the embedding of ceramic platelets in a polymer matrix (see [6.83]). This has been used as a stimulation for a composite film of 200-nm-thick alumina platelets and a chitosan polymer (Fig. 6.24b) that is both strong (tensile strength ~300 GPa) and ductile (fracturc at a strain of ~20%; see Fig. 6.24c) [6.84]. This artificial material is stronger and absorbs about one order of magnitude more energy during fracture than nacre [6.84].

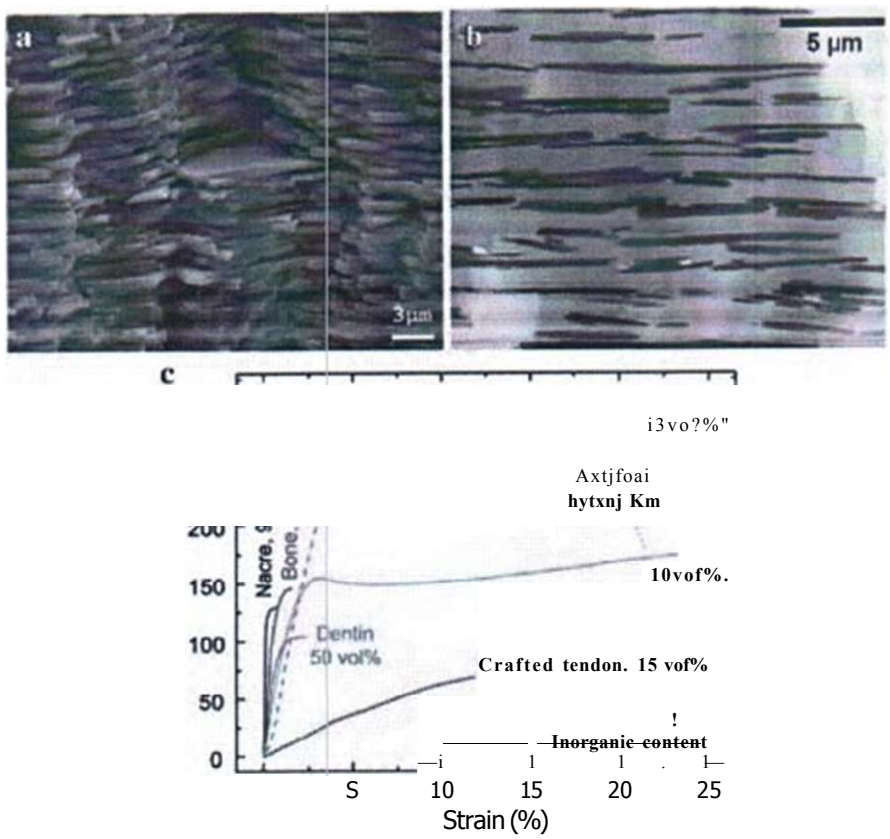

Fig. 6.24 **(a)** Scanning clcctron micrograph of the cross scclion of natural nacre, (b) Transmission electron micrograph of the cross section of the layered AhOj/chitosan composite [6.83]. (c) Stress-strain curves for nacre (red abalonc, *Haliotis rufescens),* bone, dentin, and calcified tendon: for references see [6.84). (Reprinted with permission from [6.83] **(a), (b)** and [6.84] (c). © 2008 Elsevier **(a), (b)** and © 2008 AAAS (c))

In nanocompositcs of carbon nanotubes and polymers [6.85] one could take advantage of the very high Young's modulus and the extraordinary strength of the nanotubes if one can copc with the matrix-to-nanotube stress transfer, i.e.. enhance the strength of the interface [6.86]. Here, key questions emerge concerning wetting, mechanisms of nanotubc-polymer adhesion, or measuring techniques for interfacial strength at the nanoscale. From molecular dynamics simulations, interfacial shear strengths between single-walled carbon nanotubes (SWNTs) and polymers in the 100-160 MPA range have been deduced (sec [6.86]). Experimental studies have been performed by pulling a single multiwalled carbon nanotube (MWNT) from a polymer surfacc. The MWNT is attached to an AFM lip (Fig. 6.25) and pushed into

Fig. 6.25 Pull out of a carbon nanotube (MWNT) from a polymer surface. AFM pullout testing of a single MWNT from a solid polymer droplet. (Reprinted with permission from [6.86]. © 2004 Elsevier)

m i O f i m

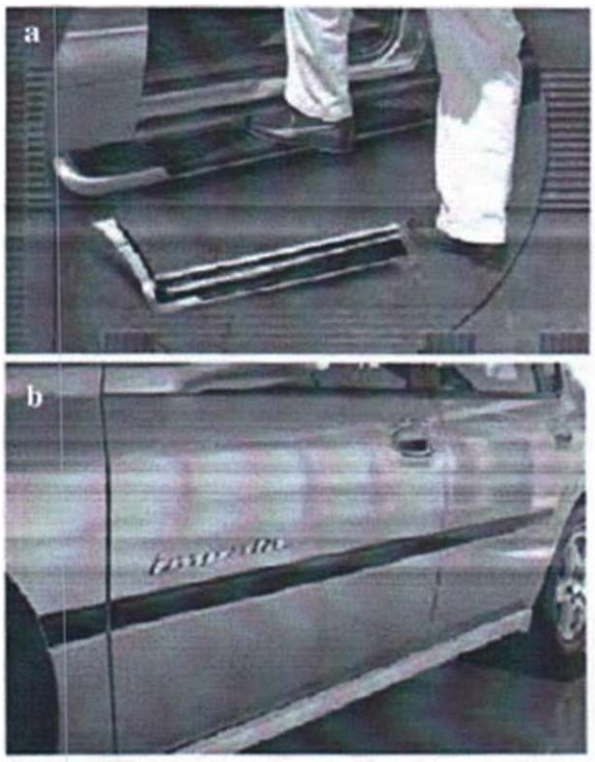

Fig. 6.26 Thermoplastic olefin nanocomposiles: applications for automotive parts: (a) M-Van step assist: first commercial launch and (b) Impala: second nanocomposite application. (Reprinted with permission from [6.91]. © 2006 SAGE Pub)

a melt of polycthylenc-butene. After cooling, the MWNT can be pulled out and an interfacial strength of 50 MPa is measured, which is by a factor of 10 higher than the adhesion level of this polymer and carbon libers and far in excess of the polymer matrix tensile strength, but substantially lower than the above simulation values. The high interfacial strength has been ascribed to the formation of a crystalline layer of material around the nanotubc surfacc (see [6.86]).

Graphene sheet (0.05 wt%, see Sect. 5.2) nanocompositcs with poly(methyl mcthacrylate) can rival values of modulus, ultimate strength and thermal stability of single-walled carbon nanotube-poly(methyl mcthacrylate) compositcs [6.87]. Cellulose nanolibrils in polymer matrices produce reinforced compositcs. The stiffness (145 GPu) and tensile strength (7.5 GPa) of these glucose based, most abundant polymer nanotibrils with diameters of 5-20 nm and hundreds of nanometers in length approach those of carbon nanotubes and should be much cheaper [6.88].

Major applications for polymer nanocomposites arc forecast for large commercial opportunities such as automobile parts, aerospace wings and fuselages, flame retardants and packing, with global consumption of polymer nanocompositcs of tens of thousands of tons [6.78] (~US $250 million) with an envisaged increase to 50,000 tons annually in 2011 (-US $500-800 million) [6.781. The most common use of polymer-clay nanocompositcs is for mechanical reinforcement of *thermoplastics,* e.g., by Ube/Toyota, to replace a metal component near the engine block for weight savings [6.89]. A clay/polyolclin nanocomposite was developed by Basell Polyolefins, General Motors (GM) R&D and Southern Clay products for a GM M-Van step assist (2001), and for side trim moldings of the Impala line (2004) (Fig. 6.26). Here, the interest is based on factors such as mass savings, large processing windows, improved scratch/mar resistance, improved recyclability [6.79|. Mass saving is also an outstanding issue in *aerospace* applications where the costs for launching into the lower Earth orbit arc approximately US $15,000 and for a geosynchronous orbit $36,000 per kg [6.801. The *toughness* of thermoplastic olefin materials can be dramatically increased by adding nanoclay particles, as they interfere with the proccss of droplet coalcsccncc, a key parameter in controlling toughness [6.79]. The use of polymer-clay nanocompositcs for *flame retardant* application [6.90] has led to two commercial products: a Wire and Cable jacket material (organoclay + aluminum hydroxide) produced by Kabelwcrk Eupcn AG, and a scries of polypropylene + organoclay + flame retardant systems (Maxxam™ FR) produced by PolyOnc® [6.89], A number of applications appeared for clay nanocompositcs as *gas-harrier* materials. Exxon Mobile has announced improvements of about 35% in air impermeability of a tire inner liner by using less than 10 wt% organoclay in brominated isobulylcnc-p-mcthylsiyrcnc copolymers (see [6.79]). The gas leakage of a nanocompositc-ovcrwrapped cryogenic hydrogen tank can be reduced by a factor of five and the structural weight by 50%, when layered silicates within the resin are used (Fig. 6.27). Clay nanocomposites can decrease the diffusivity of oxygen and water so that they are successfully used in food/liquid packaging to keep foods fresher longer [6.75], [6.891.

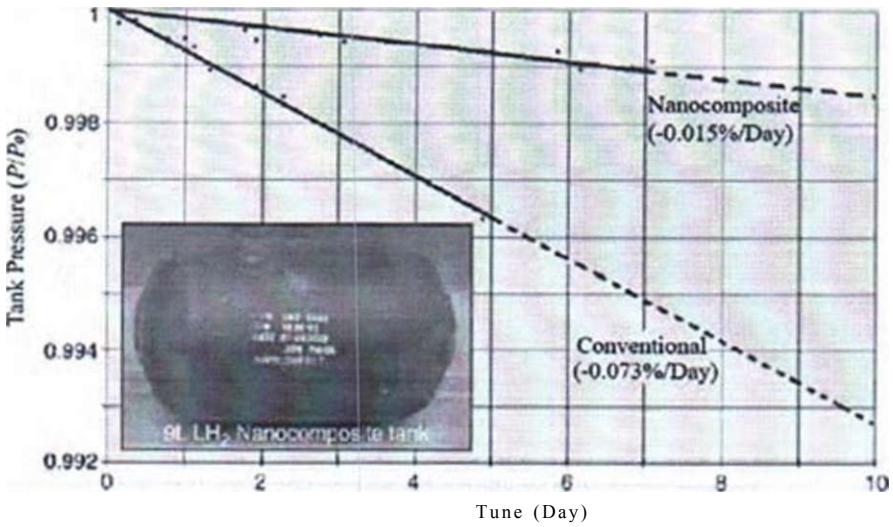

Fig. 6.27 Comparison of leak rates for a nanocomposilc-overwruppcd liquid-hydrogen tank using layered silicatcs within the rcsin. Nanoclays show reduced permeability for tank applications (helium is used for leak detection). *I'o* is the initial helium pressure in the lank. The *inset* shows a photograph of a liquid-hydrogen tank. (Reprinted with permission from [6.80J. © 2007 Materials Research Society)

6.10 Nanocrystalline Ceramics

The properties of ceramics for application as structural materials, solid-state electrolytes [6.921, sensors [6.931, catalysts [6.94], for nanoelectronics, photovoltaics, membrane technologies [6.93], or medical techniques can often be substantially enhanced by nanostructuring. Nanosized ceramics can be synthesized [6.95] by gas-phase condensation and oxidation [6.92,6.96], chemical vapor synthesis [6.93], sol-gel techniques 16.97], etc. Sintering of these ceramics can be achieved at significantly rcduccd temperatures (Fig. 6.28a) because of the small atomic diffusion distances required for densilication which also facilitate superplasticity at moderate temperatures (Fig. 6.15b). Grain growth during sintering may be suppressed by doping, as demonstrated in nanocrystalline (n-)Zr(>2-Y203 by **Al2O3** doping |6.93, 6.98]. Tlie main features of nanoceramics arc characterized on the one hand by the small crystallite size which may give rise to a blue shift of fluorescence emission (sec Sect. 4.1) or to optical transparency (Fig. 6.28c) because of suppression of the light scattering probability when the crystallite size is substantially smaller than the wave length of light [6.93]. On the other hand, the high volume fraction of interfaces in n-ceramics causes an enhanced atomic diffusivity of, e.g., oxygen [6.92] because of excess intcrfacial free volume [6.22] or to a reduction of the ion conductivity due to charge barriers at the interfaces [6.100]. It should be mentioned here that

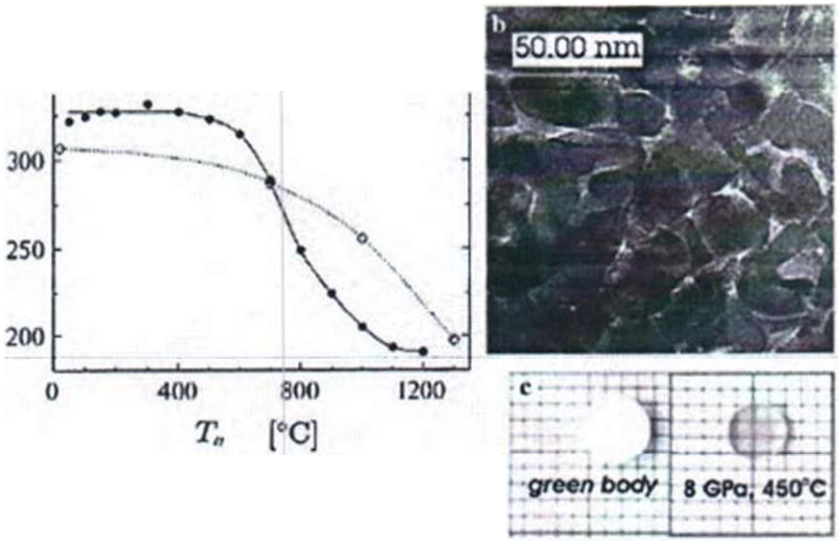

Fig. **6.28** **(a)** Mean positron lifetime as a function of the isochronal annealing temperature, monitoring the sintering process of compacted $Zt0_2$ powders, which occurs in gas-phase condensed nanocrystallinc $Zr0_2$ powders (crystallite size **4** nm. •••) at substantially lower temperatures than in commercial $Zr0_2$ powders (7 nm, 0 0 0). The higher positron lifetimes at low annealing temperatures are due to the presence of nanovoids which disappear upon sintering [6.96]. (b) Transmission electron microscopy of nanocrystalline Nd^{s+}-dopcd Y3AI5O12 (YAG) with residual porosity *(white areas)* after high pressure sintering at 8 GPa. 450^{J} C for 1 min. (c) Optical transparency of the Nd-YAG pellets before (*green* body) and after sintering (8 GPa. 450° C) [6.99J. (Reprinted with permission from [6.96] **(a)** and [6.99J (b) (c). © 1992 Materials Research Society (a) and © 2007 Elsevier (b). (c))

for solid-state electrolyte applications fully dense, crack-free nanoccramics [6.101 j arc a prerequisite whereas for filter membranes or sensors controlled porosity is desirable [6.93]. Schematic designs of nanoccramics for solid-state electrolytes for high-temperature fuel cells, for an oxygen sensor, and for a filtration membrane arc presented in Fig. 6.29.

6.10.1 Low Thermal Expansion Nanocrystallite-Glass Ceramics

In lithium-aluminum-silicatc glasses, nanocrystallites (see Fig. 6.30a) with a diameter of ~50 nm and a volume fraction of 70% can be grown by long-term thermal treatment (Fig. 6.30b). The positive thermal expansion of the glassy matrix is nearly compensated by the negative thermal expansion of the nanocrystallites, resulting in an integral linear thermal expansion coefficient of 5 — 1.4 x $10"^{S}K^{-I}$, by a factor of ~ 1000 smaller than that of Al [6.102].

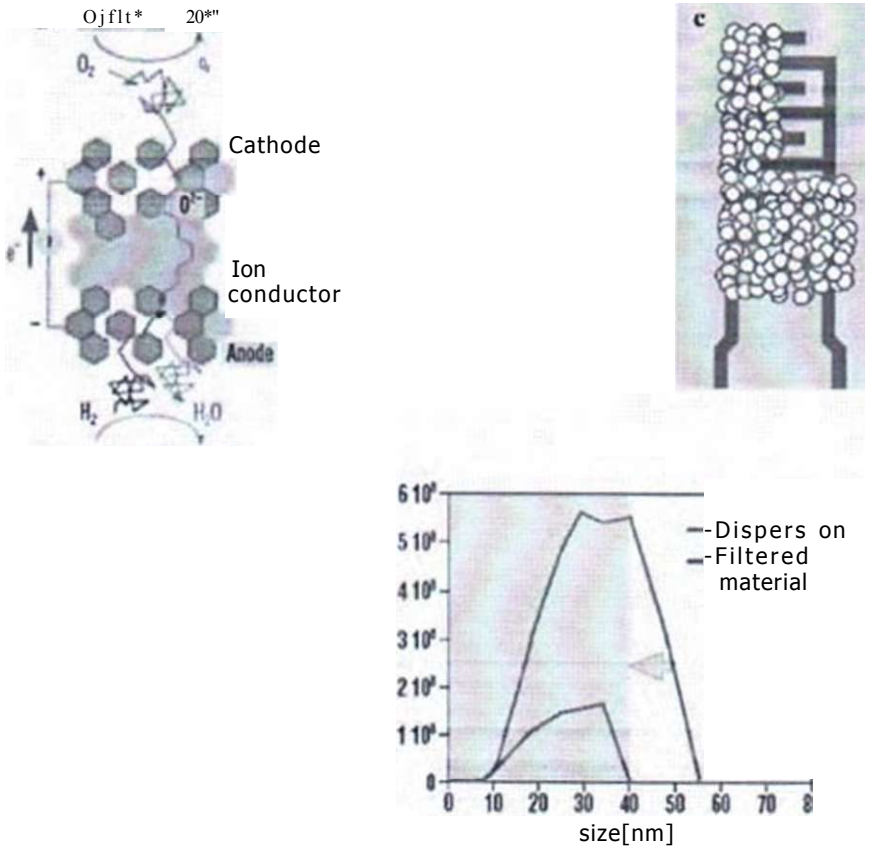

Fig. 6.29 Schematic designs of nanoceramic device applications, (a) Structure of a fuel cell with n-ZrOj • Y2O3 solid electrolyte (ion conductor), cathode, anode, and operation principle, (b) Scanning electron micrograph of a nanocrystalline TiOj oxygen sensor with platinum electrodes, (c) Schematic of the n-TiC>2 oxygen sensor ("ceramic nose"), (d) Schematic of a nanocrystalline filtration membrane ("artificial kidney") on a macro-porous substrate, (e) Separation behavior of the filtration membrane measured by means of a suspension of latex spheres [6.93] before and after filtering. (Reprinted with permission from [6.93]. © 2005 Karisnihcr Institut fitr Technologie)

Due to its extremely low thermal expansion, this nanoceramic is used for observatory mirror carriers for, e.g., the Very Large Telescope (VLT) at Cerro Paranal, Chile, with a mirror diameter of 8.2 m, for high-precision gyroscopes, as carrier for multilayer mirrors in extreme ultraviolet (EUV) lithography and large TV screens. Glass ceramic mirror carriers are also an option for the future European Extremely Large Tclcscopc (E-ELT), which is scheduled to use in 2017 a 42-m-diameter mirror with more than 900 hexagonal segments [6.102].

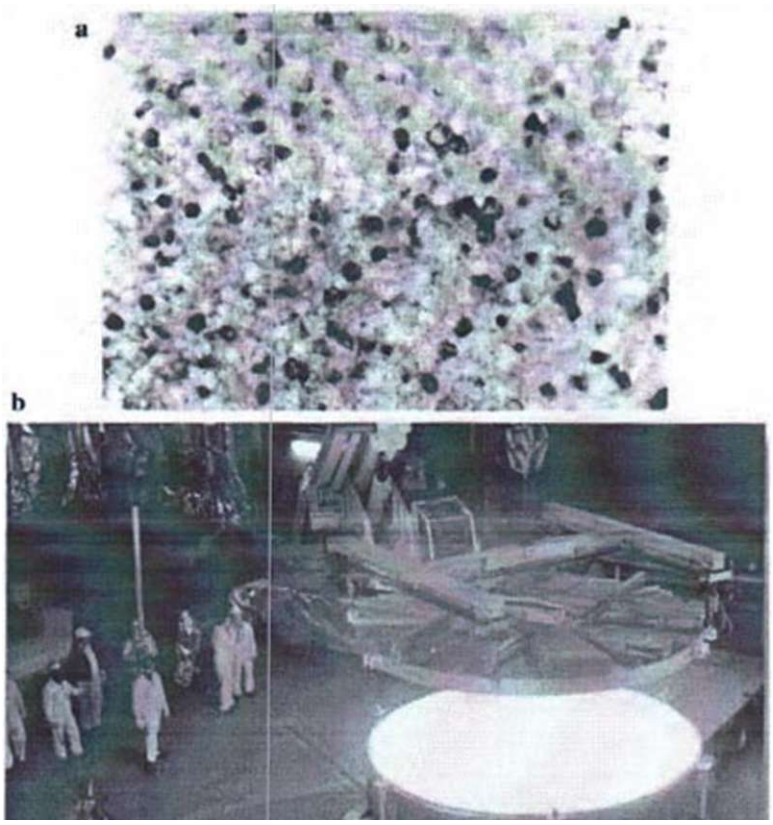

Fiy. 6.30 (a) Nanostructured glass ceramics with the nanocrystallites *(black)* and the remnant glass phase *(while),* (b) Casting of a 4-m-diamctcr telescope mirror carrier of glass ceramics at more than 1500°C. In a cooling procedure over 11 months the nanocrystallites grow to their final size of ~50 nm. (Reprinted with permission from (6.1021- © 2008 Photonik Th. Doring)

6.11 Atomic Diffusion in Nanocrystalline Materials

Atomic diffusion processes in nanocrystalline materials differ fundamentally from the processes in their coarse-grained or single-crystalline counterparts (sec [6.103]). An illustrative example can he given for copper. Whereas the atomic diffusion length $Ly = >/D_v t$ in a copper crystal at ambient temperature is completely negligible, a copper atom in a grain boundary of nanocrystalline copper will travel across Lqb = *-/DgrI* = 10 nm, i.e., the length of the size of a crystallite, within 2 h (sec [6.104]), where D_y is the diffusivity in a bulk crystal and Dqb in a grain

boundary. Therefore, diffusion may control a number of application-oriented properties of nanocrystalline materials, such as enhanced ductility, diffusion-induced magnetic anisotropy, enhanced ionic mass transport, or improved catalytic activity (see |6.103)). In this section a short survey of recent diffusion studies in nanocrystallinc alloys and ceramics will be given and the reader is referred to earlier reviews [6.103-6.109).

For experimental diffusion studies, the radio tracer technique with sputter or mechanical sectioning, electron-beam microanalysis. Auger electron spectroscopy (AGS) or secondary ion-mass spectrometry (SIMS) with depth profiling, Rutherford backscattering, or nuclear magnetic resonance were employed. In the simplest ease of nanocrystal diffusion, the two processes of rapid diffusion (D**qb**) in the interfaces or grain boundaries and the slower diffusion from the interfaces into the crystallites (Dy) have to be considered for the analysis of the experimental diffusion profiles. According to Harrison's scheme, the three types - A, B, and C - of diffusion profiles can be differentiated [6.1101. From the type A (*L\ > d,* diffusion length > crystallite size) or type C (Lv < 5, interface thickness) diffusion profiles, an average of *D* and *Dq***b** or *Dqw* can be derived, respectively. From the tail in the type B profiles *(d* > Z.v > *S)* the product *sSDqqD*^0 5 (segregation factor *s)* may be deduced. Transitions between the regimes A, B, and C can be treated numerically and GB migration due to grain growth or the appearance of several types of interfaces can be taken into account (see 16.103J). It has been shown in nanocrystalline iron that the intcrfacial difl'usivity decreases after specimen preparation in dependence of time at slightly elevated temperatures due to structural relaxation of the grain boundaries [6.111) and in fully relaxed grain boundaries the values of diffusivities appear to be rather similar to the values of grain boundary diffusivities in bicrystals (see 16.1031). Atomic simulations show (see [6.1031) that in low-energy coincidence grain boundaries atomic diffusivity is mediated at moderate temperatures by point defects with reduced activation energies of formation and migration [6.112, 6.113], whereas high-energy grain boundaries may undergo a transition from a solid to a liquid state, accompanied by a decrease in the activation energy of diffusion [6.114].

An exemplary compilation of grain boundary self-diffusivities in metals and alloys is given in Fig. 6.31 for the case of iron and iron-based alloys. The ^{50}Fe diffusivity in relaxed nanocrystalline iron [6.111] is many orders of magnitude higher than the volume diffusivity and similar to the diffusivity in grain boundaries of coarse-grained iron (g-Fe). In nanocrystalline Fc-Ni, two ^{59}Fc diffusivity processes are reported (Fig. 6.31a) where the higher values are ascribed to interfaces between agglomerates of nanocrystallites and the lower values to interfaces between the nanocrystallites within agglomerates. Diffusion processes may play a role in the desirable build-up of magnetic anisotropy in modern soft-magnetic or hard-magnctic nanocrystalline alloys, by annealing, e.g., in an external magnetic field at elevated temperatures. The ^{50}Fe diffusivity measured in nanocrystallinc Fe73.5Si,3.5B9Nb$_3$Cu, 16.115] (Fig. 6.31a) with superior soft-magnetic properties (see Chap. 8.3) is lower than in grain boundaries of pure iron, presumably due to intergranular amorphous phases. However, magnetic anisotropy formation in this material has been found (sec [6.103]) to be due to the much slower Si diffusion

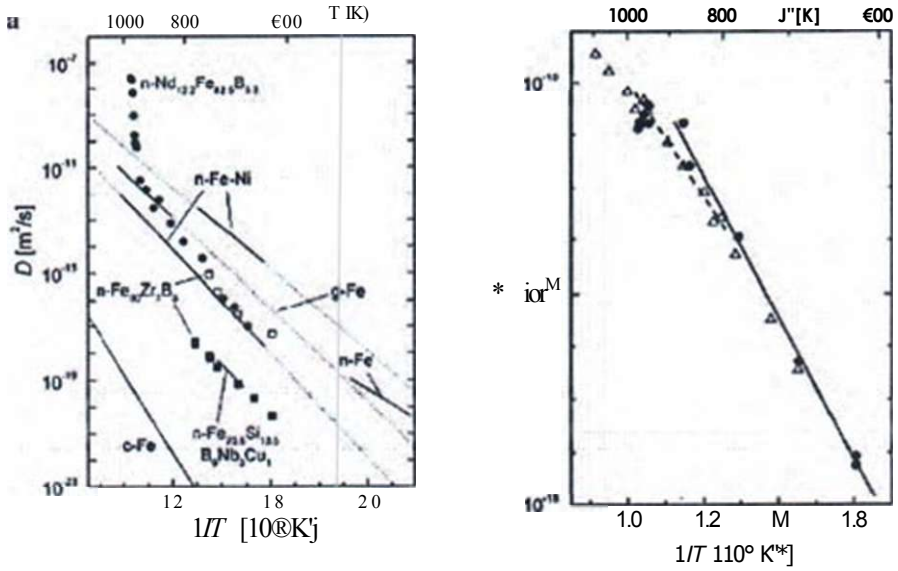

Fig. 6.31 **(a)** Arrhenius plots of ^{59}Fe-tracer diffusivities in the interfaces of nanocrystallinc Fe (n-Fe) and the Fe-rich nanocrystallinc alloys Fe73.5Si13.5B9Nb3Cu1. Fe90Zr7B3. and Nd12.2Fe78.8B9 (interface thickness δ = 1 nm). For Fe90Zr7B3 the diffusivities in two types of interfaces (• and •) are shown. The data of n-Fe refer to relaxed grain boundaries. Diffusion data for crystalline a-Fe (c-Fe), for Fe grain boundaries (g-Fe). and for nanocrystallinc y-Fe-Ni are shown for comparison. See for references text and [6.103]. (b) Comparison of grain boundary diffusivities of ^{147}Nd (•) and of ^{59}Fe (A) in nanocrystallinc Nd2Fe14B. obtained from a type B analysis assuming a volume diffusivity of ^{147}Nd equal to that of Fe in a-Fe (see [6.103]) and δ = 0.5 nm (6.116). (Reprinted with permission from [6.103] **(a)** and [6.116] (b). © 2003 Wiley-VCH **(a)** and © 2005 American Institute of Physics (b))

within the crystallites which finally enables the ordering of the Fe-Si pairs. In the hard-magnetic nanocrystallinc Nd2Fe14B-based system the ^{59}Fe diffusivity is similar to the grain-boundary diffusivity in pure iron (Fig. 6.31a) with a similar diffusion behavior of ^{59}Fe and ^{147}Nd (6.116] (Fig. 6.31b). The steep high temperature increase of the ^{59}Fe diffusivity in n-Nd2Fe14B indicates interfacial melting (Fig. 6.31a).

Self-diffusivities in nanocrystallinc metal oxides have been studied comprehensively in nanocrystallinc ZrO2 and in the oxygen ion conductor ZrO2 Y2O3 (Fig. 6.32). The ^{18}O diffusivity in the grain boundaries of fully dense nanocrystallinc ZrO2-6.9 mol% Y2O3 is found to exceed the high oxygen diffusivity in ZrO2-Y2O3 single crystals by about three orders of magnitude which may be of particular interest for application in gas sensors and electrolytes in solid oxide fuel cells (SOFCs). Open questions concerning the relationship between oxygen diffusion and ion conductivity [6.92] may be elucidated by a careful characterization of the specimen material. A similar enhancement of the oxygen diffusivity in interfaces over that in the crystalline volume, but on a much lower diffusivity level, has been observed in nanocrystallinc monoclinic ZrO2 [6.118] (see Fig. 6.32). The cation diffusivity

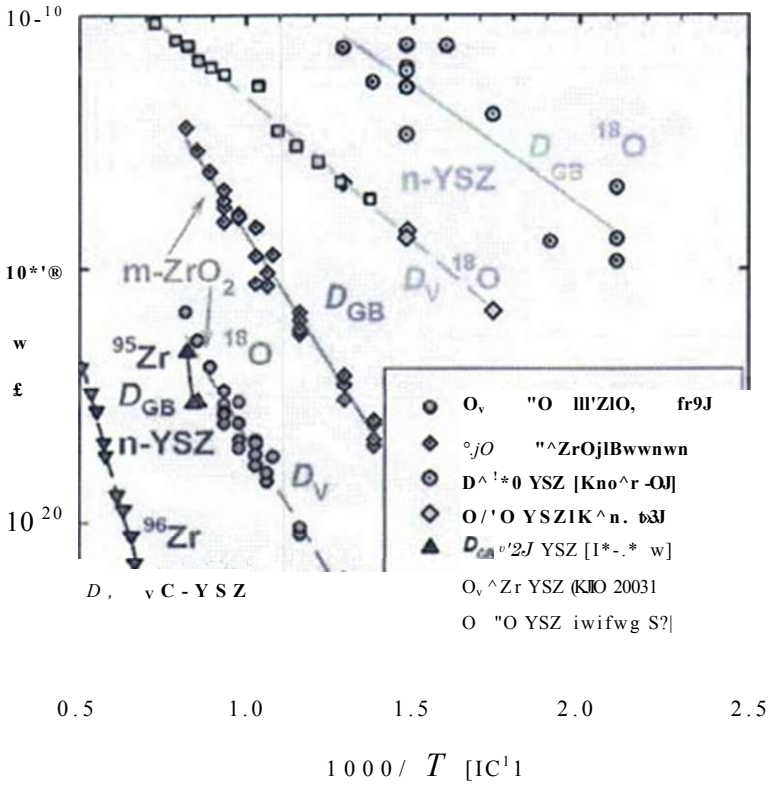

Fig. 6.32 Temperature dependence of the ^{18}O and ^{95}Zr or ^{96}Zr sclf-diffusivities in single crystals and in grain boundaries of nanocrystallinc ZrOi-YjOj and in undoped nanocrystallinc monoclinic m-ZrOi. The volume diffusivities arc designated by D\< whereas **Dgr** is the grain boundary diffusivity |6.117]. For references sec text

in nanocrystalline ceramics may be of relevance for crystallite growth and degradation of solid oxide fuel cell electrolytes. Studies in fully dense nanocrystalline Zr02-9.5 mol% Y2O3 with a grain size of 50 nm showed a ^{95}Zr diffusivity by about seven orders of magnitude higher than in single crystals [6.119] (Fig. 6.32). It may be pointed out here, as demonstrated by the data in Fig. 6.32, that the atomic diffusivities in metal oxides can cover a wide range of ~20 orders of magnitude upon doping and nanostructuring.

6.12 Surface-Controlled Actuation and Manipulation of the Properties of Nanostructures

Actuator materials and mechanisms that convert electrical, chemical, thermal, or photonic energy to mechanical energy have been sought for a long time (see [6.120]). Moreover, the manipulation of magnetic properties of materials by bias

voltages could he of rclevance for convenient design of magnetic data storage devices. Here, some recent progress in charge-induced strain in nanocrystalline metals and carbon nanotubc composites, modification of magnetic properties by electric fields, and chemistry-driven actuation will be discussed.

6.12.1 Charge-Induced Reversible Strain in Nanocrystalline Metals

Length changes in the order of 0.1% or more in response to an applied voltage have been reported for many materials, including ceramics, polymers, and carbon nanostructurcs, which in these cases arise from atomic rearrangements or charge transfer throughout the entire solid. In metals, voltage-induced length changes have been observed making use of nanometer-sized porous metal nanostructurcs [6.121]. In this case, the length change is due to a controlling of the surface charge density a in, e.g., a nanoporous Pt sample (grain size 6 nm; sec Fig. 6.33a, b) through an applied

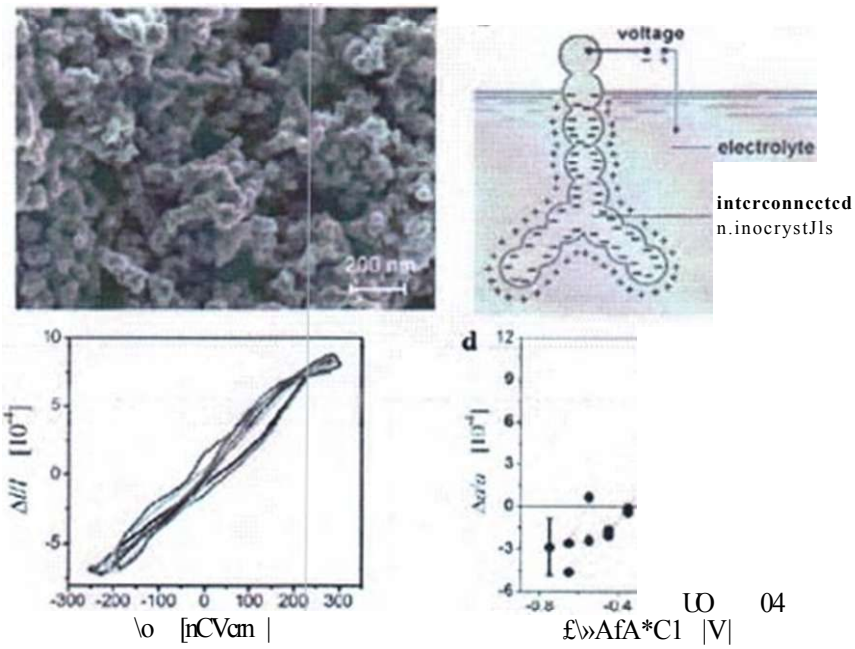

fig. 6.33 (a) Scanning electron micrograph of the fracture surface of a nanoporous Pt sample, (b) Schcmatic representation of an array of chargcd nanoparticles immersed in an electrolyte, (c) Relative length change A///, as measured by dilatomctry. versus the surface charge density **ACT.** (d) Lattice parameter *a* determined by x-ray diffraction *(right ordinate*) and latticc strain Aa/a_0 *(left ordinate*) versus *E*. The *horizontal line* indicates the lattice parameter of the dry powder. The *error bar* refers to the reproducibility of A*a/aQ*\ the uncertainty in the absolute value of *a* is estimated to be ± 0.3 pm. (Reprinted with permission from [6.121]. O 2003 AAAS)

potential E relative to an electrolyte impregnating the pores. The nanocrystallinc Pi sample shows a reversible macroscopic length changc A/// = 0.0015 in a potential E which induces a variation Aa % *500\iC/cm*^{2} of the surface charge density (Fig. 6.33c). This coincides with the voltage-induced variation of the lattice parameter Aa/flo ss 0.0014 as measured by x-ray diffraction (Fig. 6.33d). A microscopic discussion of the charge-induced strain in nanocrystallinc Pt starts from the effects of the electronic band structure on the interatomic spacing in late transition metals, where the antibonding interaction due to the upper d-band states is balanced by the bonding effect of the sp-hybridized states. Injecting electrons into the band structure changes the population of both bands, and the lattice contraction found experimentally upon injecting electrons at the surface would be compatible with the notion of a dominant effect on the bonding sp orbitals [6.121]. Even larger strain amplitudes than at present can be envisioned in porous metals with higher surface-to-volumc ratios.

6.12.2 Artificial Muscles Made of Carbon Nanotubes

An aerogel - a lightweight (1.5 mg/cm^3), sponge-like material consisting of bundles of multiwallcd carbon nanotubes (12 nm in diameter) - is light as air, yet stronger than steel and bendier than rubber. These characteristics are combined in a material that twitches like a bionic man's biceps when a voltage is applied [6.120]. Applying a voltage across the width of a ribbon of the material electrically charges the nanotubes that thread through the material (see [6.122]). This makes them repel one another and the ribbon can expand sideways by up to three times its original width with an actuation rate of 3.7 x 10^4%s~much faster than the 50% s"^{1} maximum rate of natural muscle (see l6.120]).The maximum achieved work per actuation cycle is ~30 J/kg, compared with the maximum capability of ~40 J/kg for natural musclc. Applying a voltage along the length of the ribbon has a very different effect. It triggers the nanotube structure to contract, making the material more dense and very stiff. The material can withstand extreme temperatures between 80 and 1900 K and, therefore, could be easily used in harsh environment.

6.12.3 Electric Field-Controlled Magnetism in Nanostructured Metals

The *magnetic anisotropy* of a bcc Fe (001)/Mg() 001 junction (sec Fig. 6.34a) can be modified by an electric field. Magnetic hysteresis loops, in a 0.48-nm-thick Fe layer under the application of a bias voltage, obtained from Kerr ellipticity, measurements are shown in Fig. 6.34b. From these data, a change of the magnetic anisotropy by 39% is derived when the electric field is switched from 200 to -200 V. The effect is largest for an Fe film thickness of 0.48 nm and is tentatively attributed to a suppression of the number of electrons in the = 0) electron states of Fe atoms adjacent to the MgO barrier (Fig. 6.34c) under a negative voltage due to

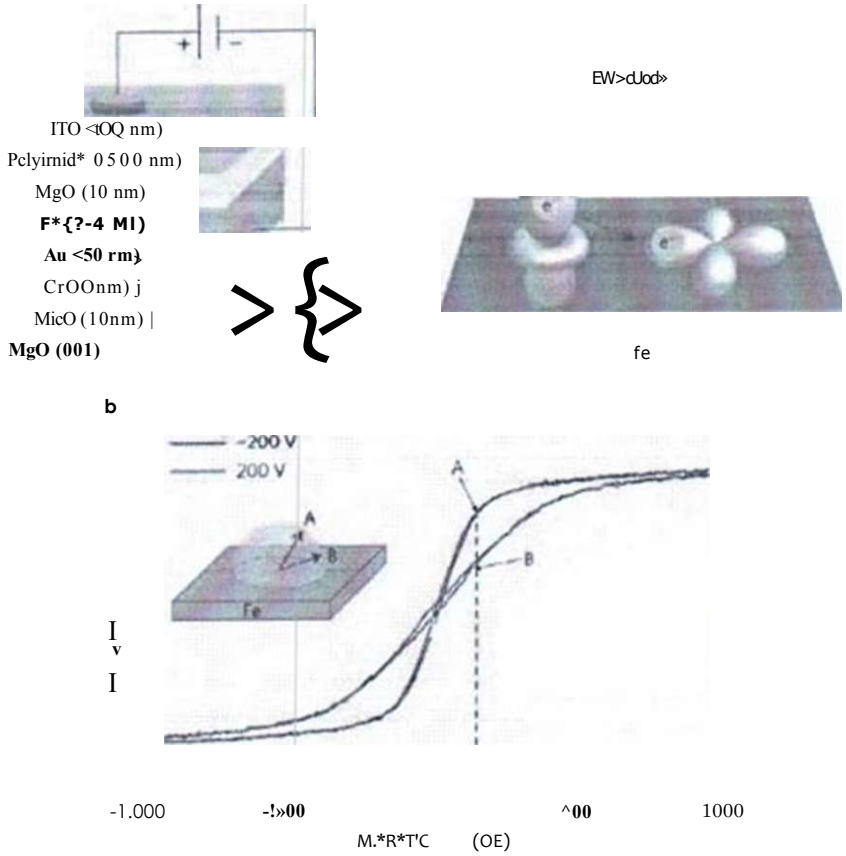

Fig. 6.34 (a) Schematic of the sample used for a voltage-induced magnetic anisotropy change. The magnetic field was applied perpendicular to film plane for magncto-optical Kerr effect (MOKE) cllipticily measurements, 7**k**- (b) Measurements of»;**k** for different applied voltages on a Fc/MgO junction (Fc thickness 0.48 nm) as a function of the applied magnetic field. The change in the hysteresis curve upon the changc of the bias voltage indicates a large change in the perpendicular magnetic anisotropy of the Fc film, (c) Schcmatic of the effect of the electric field on electron filling of the 3d orbitals in the ultrathin Fc layer. (Reprinted with permission from [6.123]. © 2009 Nature Publishing Group)

an increase in energy of these electron states. Therefore, the electron occupancy in the d_{xy} and $d_{x}z\_yi$ states could be changed relative to one another, leading to a modulation of the magnetic anisotropy [6.123). This approach may provide a technique for high-speed voltage-controlled magnetization switching.

The *orientation of the magnetization* in ferromagnetic Co, which is exchange-bias coupled to multifcrroic (sec Scct. 8.9) antiferromagnctic BiFc(>3, can be controlled and switched through the application of an electric field to the BiFe03 structure [6.124], [6.125J.

The *magnetization* at the surface of a ferromagnetic electrode in an electrochemical cell has been demonstrated to be electric Held tunable [6.126].

6.12.4 Surface Chemistry-Driven Actuation in Nanoporous Gold

The powering of actuation by chemical energy which is used in biological systems has been demonstrated for man-made actuator technologies in high-surface area nanoporous gold [6.127]. Reversible strain amplitudes of the order of a few tenths of a percent were achieved by alternating exposure of nanoporous Au to ozone and carbon monoxide. The effect can be explained by adsorbate-inducecd changes of the surface stress and can be used to convert chemical energy directly into mechanical response [6.127].

6.13 Summary

Nanocrystallinc bulk materials are polycrystals with nanometer-sized crystallite dimensions. Due to the high volume fraction of interfaces with a disordered atomic structure they are expected to show novel mechanical, thermal, electrical, and diffusive properties. Molecular dynamics studies have contributed to the understanding of the interface structure and the plastic behavior of bulk nanomaterials showing a yield strength increasing with decreasing crystallite size (Hall-Petch behavior) and turning to an inverse Hall-Petch behavior at small (~15 nm) crystallite sizes. Both ductility and strength can be enhanced in metals with nanotwin structures and superplasticity is observed. Nanocomposites of inorganic and organic materials and nanoccramics play an interesting industrial role. Due to the rapid atomic diffusion in interfaces, the diffusion processes in nanocrystalline solids are strongly enhanced. The properties of nanocrystallinc materials can be surfacc controlled by charges and electrical fields.

References

6.1 H. Glcitcr. in *Deformation of Polycrystals: Mechanisms and Microstructures,* eds. by N. Hansen et al. (RisO Nat. I-ab.. Roskilde. 1081) p. 15

6.2 R. Birringcr ct al.. Phys. Lett. **A102,** 365 (1984)

6.3 R.W. Sicgcl. H. Hahn. in *Current Trends in Physics of Materials,* ed. by M. Yusouff (World Scientific Publ.. Singapore. 1987) p. 403

6.4 H.-E. Schacfcr ct al.. in *Physical Research.* Vol. 8, cd. K. Hcnning (Akadcmic Vcrlag. Bedin. 1988). p. 580

6.5 1l. Glcitcr. Prog. Mat. Sci. 33. 223 (1989)

6.6 H. Glciter. Acta Mater. 48. 1 (2000)

6.7 A.S. Rdelstcin, R. Cam marata (eds.). *Nanomaterials* (IOP, Bristol. 1996)

6.8 C.C. Koch (ed.), *Nanostructured Materials* (Noycs Publications. Norwich NY. 2002)

6.9 U.S. Nalwa (ed.). *Nanoclusters arul Nanocrystals* (American Scientific Publ.. California. 2003)